UNTETHERED BIO-INSPIRED HELICAL SWIMMER IN CHANNELS

AYDEK GÖKÇE ERMAN

Submitted to the Graduate School of Engineering and Natural Sciences
in partial fulfillment of
the requirements for the degree of
Master of Science

SABANCI UNIVERSITY

UNTETHERED BIO-INSPIRED HELICAL SWIMMER IN CHANNELS

Aydek GÖKÇE ERMAN

EECS, M.Sc. Thesis, 2011

Thesis Supervisor: Assoc. Prof. Dr. Serhat YEŞİLYURT

Keywords: Stokes flows, biomimetic micro swimming, CFD modeling, micro swimming robots, Resistive Force Theory, macro helical swimmer experiments

This study focuses on analyzing the effects of parameters such as helical pitch, helical wavelength, and frequency of rotations and diameter of channels on the measured velocity of helix and rotation rate of the body. The first stage of this study is macro design of robots with helical tails. The fundamentals of the design are mainly based on the criteria that affect the robots' motion. The second purpose of the thesis is applying the resistive force theory (RFT) to analyze the effects of swimming parameters and diameter of channels on the velocity of helix and rotation rate of body, analytically. This theoretical model is developed for six degree-of-freedom motion of the helix but two degree-of-freedom motion results are considered because only forward speed and body rotation rates are observable from experiments. The third stage of this study is analyzing the effect of swimming parameters and the diameter of channel on the swimming motion of the swimmer with helical tail by means of CFD (computational fluid dynamics) models. In the last stage, the experimental results are compared with RFT and CFD models.

ÖZET

Bu çalışma helis yapıların içi sıvı dolu tüplerdeki hareketine etkiyen helisin çapı, dalga uzunluğu, açısal dönme hızı ve içinde ilerlediği tüpün çapı gibi parametrelerin makro yüzücünün hareketi üzerindeki etkilerinin yapılan deneylerle incelenmesi ve modellenmesi üzerine odaklanmıştır. Bu çalışmanın ilk aşaması makro boyutta helis yapılı robotların dizayn edilmesidir. Bu tasarım genel olarak robotun sıvı içindeki hareketi incelenerek oluşturulan kriterler baz alınarak yapılmıştır. İkinci aşama olarak altı serbestlik dereceli hareket denklemi teorik olarak modellenmiştir. Deneylerde sadece ilerleme hızı ve gövdenin açısal hızı gözlemlenebildiği için bu altı serbestlik dereceli hareketten sadece iki serbestlik dereceli hareket sonuçları deney sonuçları ile karşılaştırılabilmiştir. Üçüncü aşamada ise helis parametrelerinin ve kanal çaplarının yüzücü hareketi üzerindeki etkilerinin CFD (computational fluid dynamics) modeli kullanılarak iki dereceli serbestlik hareketi baz alınarak modellenmiştir. Son olarak deneysel sonuçlar geliştirilen teorik ve CFD model sonuçları ile karşılaştırılmıştır.

ACKNOWLEDGEMENTS

First of all, I would like to gratefully thank to my family to their helpful attitude and endless patience and also to my supervisor Serhat Yeşilyurt for his valuable guidance throughout of my thesis.

Especially, I would like to give my special thanks to Ahmet Fatih Tabak, Ph.D. Candidate and Fatma Zeynep Temel, Ph.D Candidate to their enthusiastic helps, valuable guidance and infinite supports throughout the development of my thesis.

I wish to thank my thesis defense jury for their valuable suggestions and comments regarding my thesis.

I would also sincerely thank to my close friends, Mehmet Ceyhan, Serkan Okursoy, Elif Hocaoğlu and Merve Acer for their support during my thesis.

LIST OF CONTENTS

CHAPTER 1
INTRODUCTION

1.1 APPLICATION AREAS OF MICRO SWIMMER

Recently, the researchers have shown an increased interest in micro systems in biomedical application of micro system due to its importance for clinical applications. One of the most significant reasons for this increased interest is that, with this new technology, the demand for "high quality" medical care can be met [1]. Developing micro robot technology will have benefit for both patient-oriented and surgeon-oriented sides. Patient-oriented advantages can be listed as reduction of recovery time, infection risks, medical complications and postoperative pain [2]. For surgeon-oriented side, this technology will lead to achieve complex sequences of operations by autonomously with geometrical accuracy, constant surgeon performance and tremor free movements [3].

Micro size robots are analyzed in terms of their applications availability and areas. Their applications can be listed as targeted theraphy, material removal, controllable structures and telemetry [2]. Targeted theraphy represents drug delivery, brachytheraphy and hyperthermia applications. In drug delivery, micro robots can increase the concentration of drug in a region of interest, thus, this target concentrated operation can decrease the side effects. In brachytheraphy, unwanted cells are destroyed via radioactive source, also in hyperhermia these cells are destroyed via heat process. Material removal represents ablation and biopsy processes such that in ablation, materials are removed from the surface that can be used as removal of fatty deposits from the internal walls of blood vessels. Furthermore, controllable structures represent the stents, occlusion and implants. Micro robots can serve as stents to keep the passageways open, or as occlusion to block them, or as an implant. Lastly, they can be used in telemetry operations to transmit to specific locations [2].

These applications can be used in areas such as the circulatory systems, the central nervous systems, the urinary systems/prostate, eye, ear and fetus [2]. In circulatory system, which consists of heart and vessels, especially targeted therapy, removing plaque, destroying

blood clots and acting as stents applications can be done with micro robots. In urinary system, for instance, micro robots have potential to destroy the kidney stones. Also, eye's retina is a critical location for treatment that sensitive manipulations which are risky with human performance can be done with these robots. Furthermore, in ear, stem cell application, which can be used generate of cochlear hair cells to activate the hearing activity, can be done via these micro technology. In addition to that, in fetus, micro robot can enter the uterus for occlusion and ablation applications [2].

Furthermore, these mechanical or electromechanical devices can have the dimensions as in nanometers which are nanorobots. These robots also have same kind of tasks with micro ones as targeted drug delivery, being beneficial for molecular medicine and allowing instant pathogen diagnosis and extermination [4]. Moreoever, molecular nanotechnology can allow cleaning the air, removing pollutants from the water and restoring the ecosystem [4]. Although all of these tasks can be achieved by micro size robots, nano size has some advantages like prevention of damaging of the blood vessel walls or clots which are occurred due to blocking the blood vessels too much [4].

1.2 PREVIOUS WORKS

1.2.1.Planar Wave Propagation

The first serious discussions and analyses of propulsion methods emerged with Sir Geoffray Taylor [5] who was analyzed the propagated bending waves. Then, Gray and Hancock [6] published paper in which the propulsive force on spermatozoa was calculated by using the linear relation between force and velocity. This method was named as Resistive Force Theory (RFT). This research showed that this propulsion speed was depending on the frequency of the waves, the square of the amplitude of waves, wave length, the difference between the coefficients of normal and tangential resistance, size and the drag coefficient of head and finally the length of the tail [6]. Both Taylor and Gray *et.*al researches determined

the linear velocity of the organism by assuming that the angular velocity of the body was known.

1.2.2.Helical Wave Propagation

Chwang et.al [10] published a paper which they analyzed the helical motion by describing a method to determine the longitudinal components of both forward speed of body (U) and angular velocity of head (Ω). They claimed that, if the body was propelling itself with a constant mean velocity in a viscous regime, due to conservation of linear and angular momentum, both the resultant force and the resultant torque acted on the body by the fluid must vanish, which was led to two equations with two unknowns that were U and Ω (2 DOF in total). In another study, Keller and Rubinow [7] modeled three dimensional trajectories of helical micro swimmers by calculating the transverse component of U as well as longitudinal components of U and Ω, which was proved that, when flagellum moves helically, the trajectory of it also helical (3 DOF in total). Also, Lighthill [8] demonstrated in his approach, named as Slender Body Theory (SBT), that, long range hydrodynamic interactions modified the flow field experienced by the flagellum, which were not considered in Resistive Force Theory by Gray and Hancock. These interactions were listed as flagellum-flagellum interactions and cell body-flagellum interactions As a result of considering this effect between small flagella segments was led to calculate appropriate resistive force coefficients. Johnson and Brokaw [9] argued that, this interaction between body-flagella and flagellum-flagellum were insignificant for small cell bodies; on the other hand, they were significant for larger cell bodies and they showed using SBT would give better results than RFT by examined helical waves. Higdon [11] developed a numerical model by employing Lighthill's Slender Body Theorem (SBT) for Stokes flow. With this model, he analyzed a micro organism with helical propeller in free environment by parametrizing this tail.

1.2.3.Propulsion with Wall Effects

A. J. Reynolds [12] described the motion of bending waves nearby the wall. He defined the problem in a bounded environment, since this environment was more realistic for tiny

organisms and the interactions between the swimmer and the environment was crucial because of changing the motion trend with respect to unbounded one. He observed that near the wall, the large increase in propulsive speed would be possible only if the energy output was increased significantly. Analysis of wall boundary effect to propulsion also modeled by Blake [13] by obtained the image system for a stokeslet in a stationary boundary layer which was advantageous for constructing fundamental singularities, thus, the boundary conditions were automatically satisfied. This work was extended by Blake and Chwang [14] by deriving the similar image system for a couplet, a source and a potential doublet [14]. Katz et al. [15] examined the wall boundary effect, too. They mentioned that, when the wall separation decreased to order of a slender body length, the wall effects became significant. In unbounded environment the ratio of normal to tangential resistive force coefficients was limited by two, but they proved that this value was increasing near wall. Because of increasing ratio, the propulsive speed of organism was increasing, too; thus more energy was consumed [15].

A recent study of Ramia et al. [16] presented Boundary Element Method to consider the effect of plane boundaries in the theory of low Reynolds propulsion system. This method was applicable to any number of organisms having arbitrary geometry, orientation and distance from a given plane boundary. Only uniflagellated, spherical organisms propelled by helical flagella were presented with different orientations with respect to wall boundaries. They claimed that the propulsive speed was increasing by 10% near the wall boundary. Lauga et al. [17] demonstrated that *E. Coli* bacteria made clockwise circular motion near solid boundaries, and claimed that this was the result of force free and torque free swimming and hydrodynamic interactions with boundary. Furthermore, they proposed simple analytical model for this motion based on the Resistive Force Theory, model results agreed well of *E. Coli* experiments. Felderhof [40] applied perturbation method to analyze the wall boundary effect of a circular tube on cylindrical the body and he concluded that confinement of the fluid had a crucial effect on both the speed and dissipation of swimming in low Reynolds number.

1.2.4.Numerical Studies

Phan-Thien [39] analyzed the shapes of micro organisms to find the most efficient one by using Boundary Element Theory. They applied this method to study the locomotion of a

micro organism with helical tail and they wanted to investigate the optimal parameters of the tail to attain the most efficient swimming speed. Also, Ramia et.al [16] analyzed the wall effect on trajectory and swimming speed and this analysis were based on BEM, too. Lastly, Goto et al. [19] performed a series of experiments on *Vibrio alginolyticus* which had helical propeller, and these observations were compared their results with the Boundary Element Method computation.

1.2.5.Experimental Studies

Goto et al. [19] performed a series of experiments on *Vibrio alginolyticus*, which was a bacterium with helically shaped flagellum, to observe the speed and the rotation rate of the cell body and recorded the dimensions of cell body and flagellum by using the images taken by dark field microscope. Author compared the experimental results with the Boundary Element Method results. Then they extended their studies to observe the influence of a rigid boundary and free boundary on the motion of helically flagellated bacteria and data were analyzed for swimming speed, curvature of trajectory and change in number of bacteria with respect to different boundary conditions. Authors observed that *Vibrio alginolyticus* did not have an ideal shape and the BEM computation allowed to model arbitrary cell body shapes with helical flagella. In addition to that, their results were not supported Ramia's because, although the propulsive speed increased with the presence of the wall, drag force on the cell body also increased and this increasing was dominant with respect to increment in propulsive speed.

Chattopadhyay et al. [21] presented experimental observations for three bacterial strains; *Vibro alginolyticus*, *Caulobacter crescentus* and *Escherichia coli* with a single polar helical flagellum. They compared their experimental results with RFT and SBT in the literature and reported that SBT results agreed better than RFT ones for all strains tested especially for propulsive speed.

Purcell [22] suggested that for net propulsion, hinged mechanism could have at least three links for non reciprocal motion. This mechanism was analyzed by Becker, Koehler and Stone [23], that, direction of net translation and speed was not only depending on the angular amplitude between links, but also the relative length of them. Chan and Hosoi [24] demonstrated this three link swimmer design and their experimental results were similar to developed theory.

Figure 1.1: Experimental work by Chan and Hosoi on the motion of the three link swimmer [24]

One of the most interesting experiments was carried out by Dreyfus et al. [25] that, linear chain of colloidal magnetic particles linked by DNA and attached to red blood cell was actuated by an external magnetic field and the structure acted as a flexible artificial flagellum with beating movement.

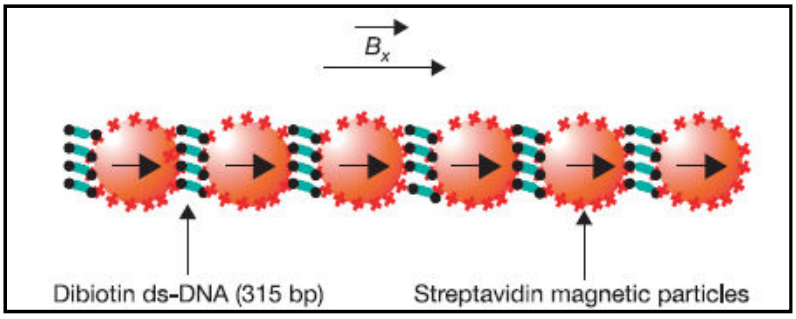

Figure 1.2: Schematic representation of a flexible magnetic filament

A relationship between frequency and thrust force was measured by Behkam and Sitti [26] in an experimental setup consisting of a two phase stepper motor a tail made of a steel wire as a helix. The tethered motion of the tail allowed measurement of the beam deflection due to the thrust force. They claimed that, their experimental results were supported their developed model based on RFT such as, the thrust force and the frequency had the linear relationship.

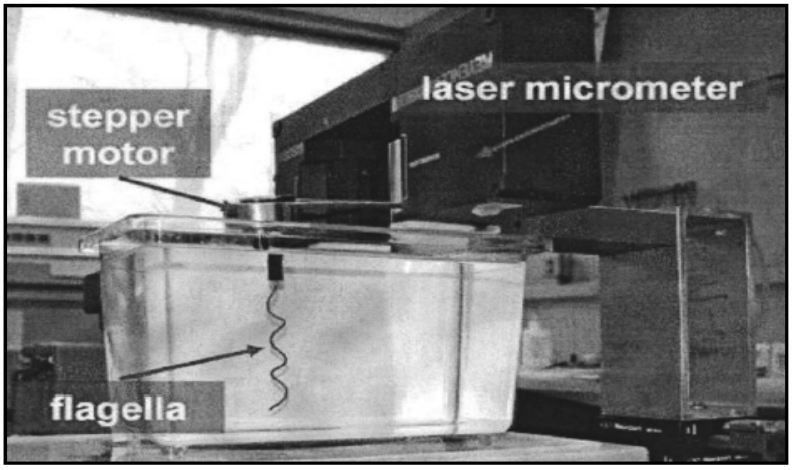

Figure 1.3: Experimental setup for helical wave propulsive force measurement [26]

The first demonstration of an untethered device propelled and navigated in the blood vessel of a living animal was done by Martel [27] et al.; authors controlled and navigated a 1.5 mm diameter ferromagnetic bead in the carotid artery of a living swine. They used magnetic resonance imaging (MRI) platform not only for imaging but also for navigation.

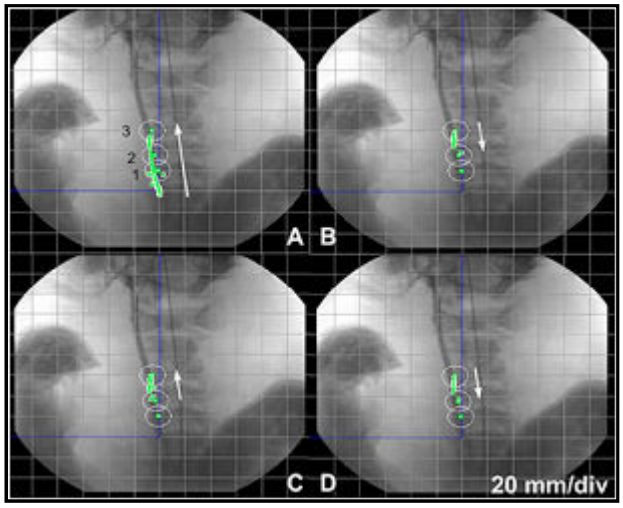

Figure 1.4: In vivo automatic navigation of a 1.5 mm ferromagnetic bead inside the carotid artery of a living swine. Trajectories are superimposed over an x-ray angiograph. The line of dots over the artery shows actual displacement of the bead

Zhang [28] et al. produced the artificial bacteria flagella (ABF) with two parts a helical tail and a soft magnetic metal head. They applied external magnetic torque to produce rotating motion and it was observed that with increasing frequency, the propulsive speed increased until the step out region where the magnetic torque could not overcome the drag force on the swimmer and the speed decreased dramatically.

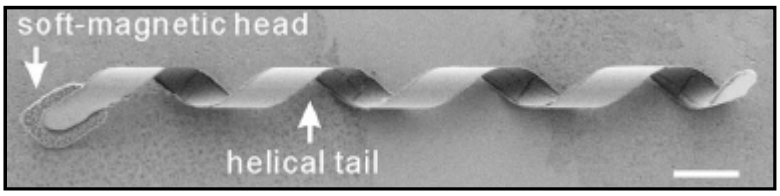

Figure 1.5: Fabrication procedure of the Artificial Bacteria Flagella with InGaAs/GaAs/Cr helical tail [28]

Peyer et al. [29], extended the study of Zhang et al. [28]; they observed near wall motion of artificial bacteria flagella. Authors claimed that at low frequencies the desired screw type motion was replaced by wobbling swimming movement. The results of Zhang et al. [28], at high frequencies ABF's propulsive speed increased with increasing frequencies until a frequency where the torque could not overcome the drag of swimmer. On the other hand, for low frequencies wobbling and drifting velocities were dominated the forward propulsive speed.

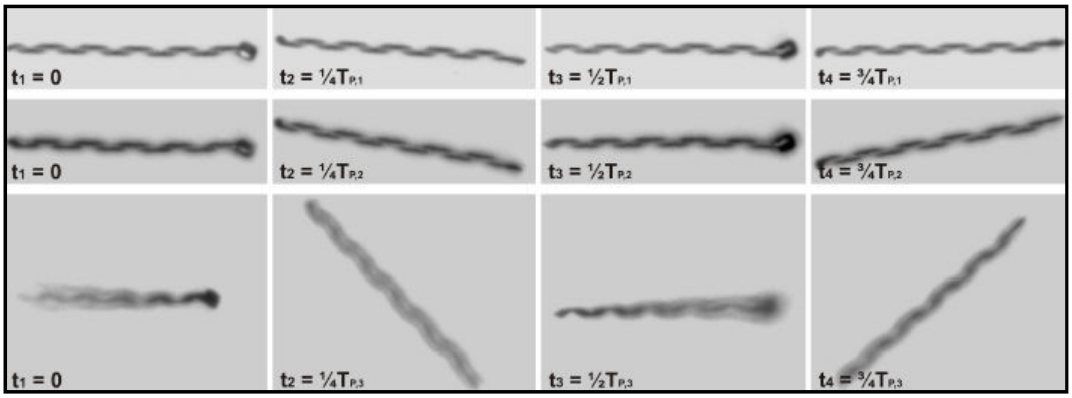

Figure 1.6: Time lapse of the ABF swimming at three different input frequencies $f_1 > f_2 > f_3$

The flexible oar design of Yu [30] was a flexible tail actuated by a single motor at the tail's base. Design's base was fixed at the origin and with rotation of motor; its shape was varied sinusoidally. This rotation was converted to an angular oscillation with Scotch Yoke and lever mechanisms. As a result of the beating elastic tail sinusoidally, a propulsive force was generated. Due to this thrust force, cantilever beam was deflected and this deflection was measured as an electrical signal by strain gages where the strain measurement was converted into a force measurement. Yu [30] measurements of propulsive force and time varying shapes had a good agreement with the results of the Resistive Force Theory.

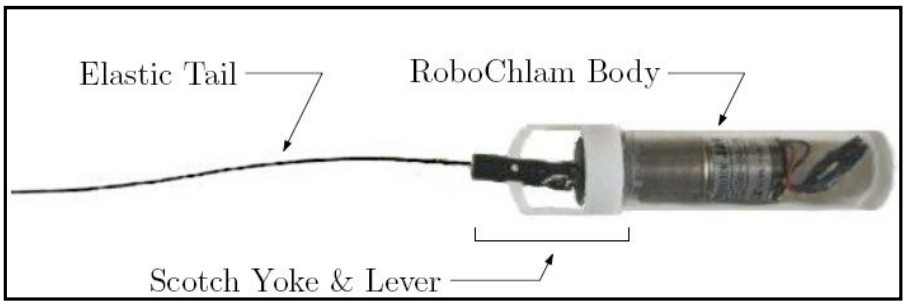

Figure 1.7: Robotic elastic-tail swimmer-dubbed "RoboChlam". The body houses a geared DC motor driven by an external power supply. The Scotch yoke and lever convert the motor's rotation into an angular oscillation. A steel wire at the end of the lever acts as an elastic tail

In the study of Zhang et al. [31], a macro scale swimmer design is introduced with propelling rotating cylinders which was supported by a flotation structure nearby wall. Swimmer moved near to the wall when cylinders were rotated at same angular velocities, but with different angular velocities, periodic motion near the wall was observed.

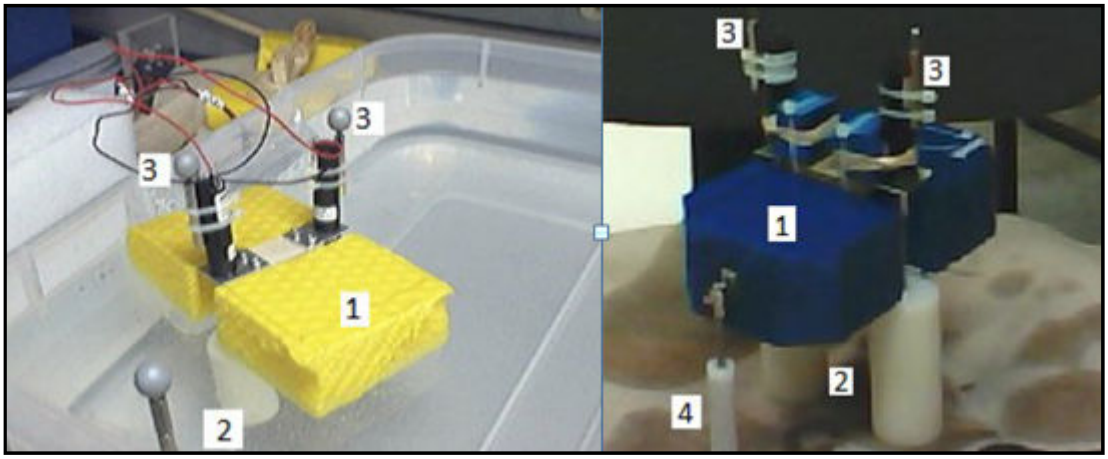

Figure 1.8: Left Picture: Picture of 2-cylinder swimmer. 1. Foam Flotation 2. Nylon Cylinders 3. Motors/Tracking Markers Right Picture: Picture of 2+1-cylinder swimmer. 1. Foam Flotation 2. Nylon Cylinders 3. Motors/Tracking Markers 4. Nylon Cylinder

Chen et al. [32] produced a mechanism with four flexible tails to make the swimming of robot more controllable than the single tail one. This prototype was placed in a silicon oil filled tank sufficiently far from the walls and away from the bottom of the container. Author claimed that the swimming direction can be controlled efficiently by adjusting the rotation of the tails.

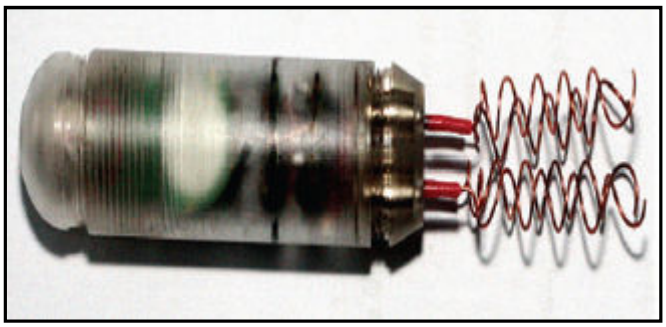

Figure 1.9: Robot prototype with four helical tails made from Shape Memory Alloy (SMA)

1.3. BACKGROUND

1.3.1. Mechanics of Micro Organisms

Flows with Reynolds number less than one are in Stokes regime thus, inertial terms are negligible in Navier Stokes and viscous terms become dominant. According to Scallop Theorem the propeller system must make non reciprocal motion in Stokes regime due to produce net propulsion [22].

1.3.1.1.Eukaryotic Ciliary Beating

Eukaryotic cilia are a motile organelle whose the movement are controlled by relative motion of microtubules which are powered by dynein ATPase motors. Although cilia have the same structure as the flagella; there are some differences between them such as ciliated cells which have many short cilia, e.g the unicellular protozoan Paramecium which is covered by thousands of cilia [3].

Cilia consist of a central bundle of microtubules as axoneme which is surrounded by nine outer doublet microtubules with surrounding a single microtubule [3]. For beating movement, this structure needs ATP and when the ATP is added, sliding movement between pairs of double microtubules cause a bending movement of the axoneme and can propagate. This doublet microtubules' sliding movement is result of force generating proteins such as dynein ATPase motors.

From engineering point of view, this structure is hard to mimic because of too many short cilia are needed to attain beating movement and miniaturization of the power source problem cannot be addressed easily.

1.3.1.2.Eukaryotic Flagella

A eukaryotic flagellum is a bundle of nine fused pairs of microtubule doublets which are surrounding by two central single microtubules. These nine microtubules also extend to two dynein arms, the part which helps flagella to bend by sliding movement against each other [1]. Eukaryotic flagella and cilia have some differences such as beating pattern. Cilia are generally 2-20 [nm] long while the eukaryotic flagella are 100-200 [nm]. Also, cilia occur in vast numbers while flagella occur in smaller numbers.

Furthermore, flagella generate the propulsive force by propagating planar or helical waves. This wave movement must be non reciprocal to create net propulsion in Stokes regime.

1.3.1.3. Prokaryotic Flagella

These kinds of flagella are different from eukaryotic ones with three features. First of all, prokaryotic flagellum is a helical flagellum which is made of 20000 to 30000 flagella. Secondly, because of the material composition of prokaryotic flagellum it is more rigid than the eukaryotic one [5]. Furthermore, actuation mechanism is different such that prokaryotic flagellum is actuated by a rotary motor embedded in the cellular wall while eukaryotic flagellum is actuated by the motor which spreads along the filament [2].

1.3.2 Challenges of Design

- **Miniaturization**

Medical micro robots must be able to travel inside veins and arteries, cavities as well as soft tissues. This introduces a problem because of size differences between the areas where the robots operate. Moreover, miniaturizing of power source to achieve effective onboard controllable propulsion becomes a major challenge [33].

- **Biocompatibility**

Micro swimming robots in body must also ensure to avoid allergic or toxically reactions inside the human body comprehensive toxicity, corrosion and allergy tests must be carried out. For instance, Ni and Ni compounds are non biocompatible, thus, instead of them Ti and Ti alloys are used in medical devices because of their excellent combination of biocompatibility and corrosion resistance properties [34]. Dogangil et al. [34] studied retinal drug delivery system via wireless magnetic micro robots; and due to Ni element is not being biocompatible; author suggested coating their Ni pieces with thin layer of Ti to achieve bio compatible design.

- **Control of orientation**

Extremely high resolution, accuracy, stability and fast response are necessary for micro and nanoscale positioners [33]. Thus, control issue of micro robots is not achieved precisely due to lack of precision control and manipulation of devices and materials at micro and nanoscale. In addition to that, due to the lack of response availability of electronic circuits that can operate in the corrosive environment of human body, software based algorithms/programs may not be used for implementation of fully controllable nanorobots [33].

- **Computation difficulty of electromagnetic field in human body**

Electromagnetism is used in micro robot technology in controllability and treatment areas. For designing an optimal system for optimal treatment, it should be understood the distribution of electromagnetic field in human body. On the other hand, both the material composition and the geometry of human body are very complex which makes this computation a complicated work [36].

1.3.3. Powering Micro Robots

Batteries are inexpensive power source however their scalability is extremely limited to operate in microscopic dimension. The advent of the semiconductor technology arbitrarily shaped rechargeable thin film batteries can be built with thicknesses less than 50 μm [2].

The other important power source for micro robots is fuel cells which harvesting chemical energy directly from the environment with high energy density and low cost. These devices can directly transform chemical energy into electrical one via electrochemical reactions [37]. One of the most significant features of these cells which makes them attractive for *vivo* applications is they can operate under 20-40 °C and near neutral pH [37]. Also, their structural simplicity is made them appropriate for micro applications. In other words, *in vivo* applications are the most obvious target for biofuel cells due to their capability to provide long term, even permanent power supply for pacemakers, glucose sensors and prosthetic valve actuator. With today's technology, biofuel cells consist of two 7 μm diameter carbon fibers, each coated with a different "wired" enzyme bioelectrocatalyst [38].

The other approach generating power for micro robot is using wirelessly transmitted source which is possible with magnetic fields. There are two methods for achieving this magnetic source either by using time varying fields to induce current or by quasi static and low frequency fields to obtain forces and torques which are applied to magnetic materials [2].

1.4. ORIGINALITY OF THIS WORK

In this work, we studied the hydrodynamic behavior of the untethered bio-inspired swimmer within a bounded environment with changing geometric parameters of helical tail and cylindrical channel.

CHAPTER 2

DESIGN OF HELICAL PROPULSION SYSTEM

2.1. DESIGN OPTIONS

2.1.1. Rigid Helical Flagellum

Due to its rigid structure, this implementation imitates prokaryotic flagella. In this design, a rigid helix is attached to a rotary motor exhibiting motor the simplicity of this approach is extremely simple and rigid helical flagellum is easy to use. One of the disadvantage is that the safety problem because of not having to opportunity to adjust the shape of it with respect to boundaries' limits where it is settled in.

2.1.2. Compliant Helical Flagellum

To produce a biocompatible helical flagellar design *in vivo*, the stiffness of the helix can be adjusted by producing it with molding technique and using biocompatible elastomers. Under swimming loads, this material can get desired helical shape. On the other hand, there are some disadvantages of this design such as, complexity in manufacturing process and calculation of all possible loading values to ensure the safety of its use [41].

2.1.3. Flexible Helical Flagellum

In flexible helical flagellum design, each segment of the tail must be in equilibrium between the internal stresses and external loads [42]. Advantage of this design is that, this flexible approach provides safety by design because the filament has the ability to adjust its shape with respect to boundaries'. On the other hand, major disadvantage of this flexible tail is that, it involves more engineering process than a rigid helical flagellum. Furthermore, this kind of helical design only allows for forward propulsion.

2.2.DESIGN CRITERIA FOR EXPERIMENTS

- Neutral Buoyancy

For neutrally buoyant design, the ratio of weight to its volume should be equal to fluid's specific weight. Thus, when the prototype submerges into the fluid, it can remain at rest.

- Stability

Stability is an important criterion for a prototype in order to ensure the movement of real bacteria. The aim is to make the center of gravity and buoyancy to be as close as possible since the distance between these locations can result in a net torque that rotate the body until a stable position is found.

- Propulsive Speed

During design process of the prototype, it is realized that the forward velocity must be taken into account for analyzing the helical flagellar system appropriately. As a result, the capsule and the tail dimensions are determined with respect to efficiency of the movement. Not only is the dimension of the prototype, but also the determination of power source important criterion to obtain a desired propulsive speed.

- Low Power Requirements

Due to the value of maximum observable propulsive speed has 10^{-3} order of magnitude, low power requirements allow for wireless transmission. Thus, this leads more compact prototype design.

- Size

The prototype is designed in macro scale, thus, with larger components manufacturing process become easier. On the other hand, due to autonomous motion of the prototype, size has limitations with respect to efficiency of the helical flagellar propulsion.

- Simple

Experiments are repeated many times, thus, manufacturing and assembly must be easy to produce, almost the same swimmer for each experiment. Thus, the simplicity criterion is extremely important for the repeatability of the experiments.

2.3.PROPOSED DESIGN

2.3.1.Helical Tail

- **Helical Tail Parameters**

A helix can be described by its length L, its amplitude B, its wavelength λ, and its filament radius r. Its representation is given in Figure 2.1. Mathematically, a single turn of the helix is:

$$x = B\ cos(kz) \tag{2.1}$$

$$y = B\ \sin(kz) \tag{2.2}$$

$$k = 2\pi/\lambda \tag{2.3}$$

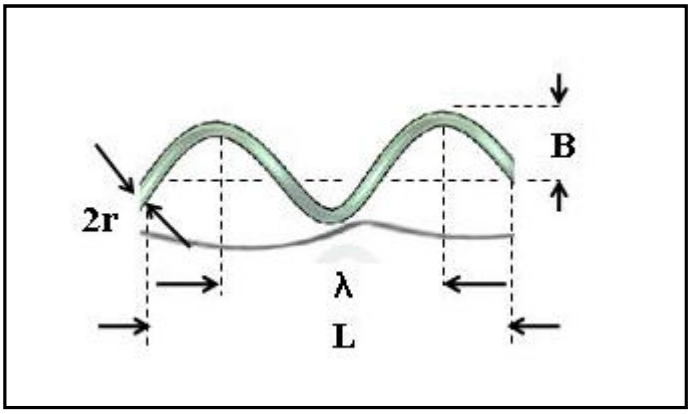

Figure 2.1: Helix Parameters

The helical tail of the robot is made of steel wires with the diameter *r* of 1 mm and apparent length *L* of 48 mm. These steel wires are undergone plastic deformation by surrounding them around drill bits with diameter 2 mm, 4 mm, 6 mm and 8 mm. Also, the wavelengths of the helical tails are adjusted as 24 mm, 16 mm, 12 mm and 8 mm. As a result, helical tails are carried out with 1 mm, 2 mm, 3 mm and 4 mm amplitudes and, 24 mm, 16 mm, 12 mm and 8 mm wavelengths which lead to having different effective tail lengths as seen from Table 2.1. It can be calculated as:

$$L_{eff} = \sqrt{(2\pi B)^2 + \lambda^2}\,\frac{L_{tail}}{\lambda} \tag{2.4}$$

Table 2.1: Robots' Names and Parameters

ROBOTS	B (mm)	λ (mm)	L_{eff} (mm)
A_2	1	24	49.61
A_3	1	16	51.56
A_4	1	12	54.18
A_6	1	8	61.03
B_2	2	24	54.18
B_3/B_3*	2	16	61.03
B_4/B_4*	2	12	69.5
B_6/B_6*	2	8	89.38
C_2	3	24	61.03
C_3/C_3*	3	16	74.17
C_4/C_4*	3	12	89.38
C_6/C_6*	3	8	122.86
D_3/D_3*	4	16	89.38
D_4/D_4*	4	12	111.4
D_6/D_6*	4	8	158.25

In robots' name letter A represents the robots having 1 mm amplitudes, letter B represents the robots with 2 mm amplitudes, letter C represents the robots with 3 mm amplitudes and letter D represents with 4 mm ones. The subscripts denote the number of waves. Also, the superscript * denotes the robots which are used in *Channel 2* experiments namely B_3*, B_4*, B_6*, C_3*, C_4*, D_3*, D_4* and D_6*. Robots without superscript are the ones which are used in *Channel 1* experiments. For instance, the only difference between B_3 and B_3* robots is that their measured frequencies. All the parametric features and pictures can be seen in Appendix B.

- **Importance of Helical Tails' Twisting Direction**

Robots' helical tails are twisted in counterclockwise direction. In principle, forward propulsion is ensured if tail rotates in clockwise direction and body rotates in counter clockwise as seen from the front. Also, if the rotation directions are reversed, backward propulsion can be observed as seen from Figure 2.2.

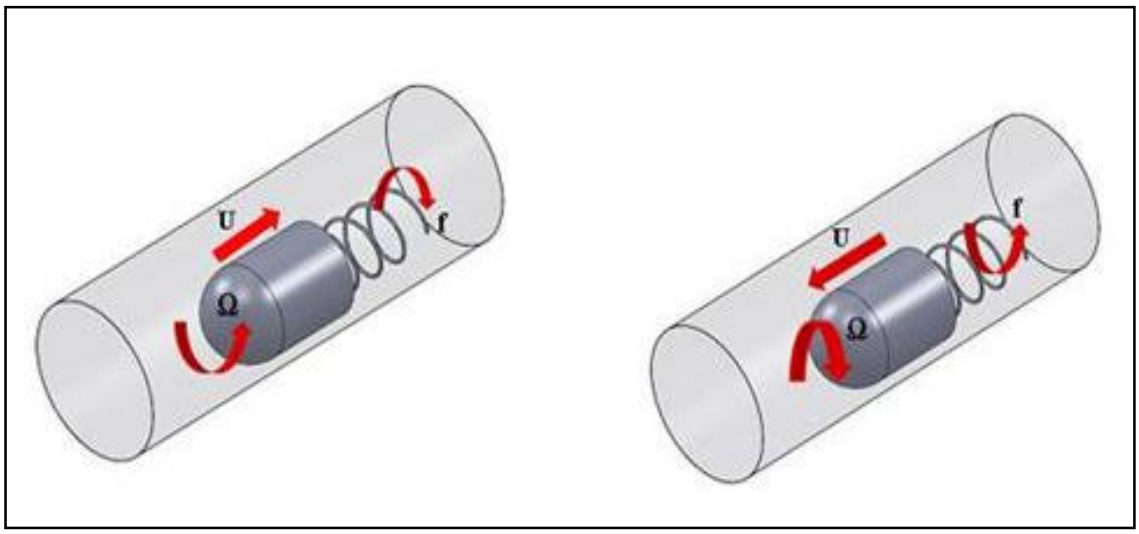

Figure 2.2: Tail and body rotational directions for backward and forward propulsion

2.3.2.Material Selection and Assembly

The body part of the prototype is made from a glass tube, with 40 mm in length and 7.9 mm in radius, with respect to neutral buoyancy and stability of the design. Glass tube's weight and its distribution lead to almost neutrally buoyant design without exerting any couple force which leads to rotation of the body.

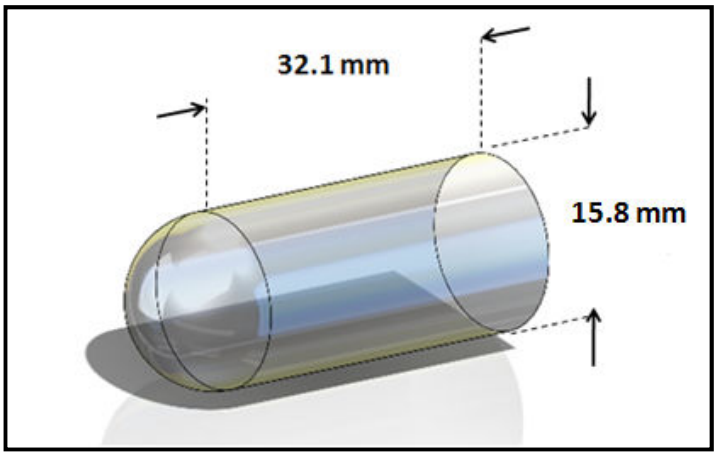

Figure 2.3: Glass tube's dimensions

In glass tube, there are three parts of small dimensions named as the battery, motor and six legged switch. Increasing the number of parts lead to get more complex design which threatens the repeatability of the experiments. In addition to that, small dimensions lead to have more compact design. First part in the body is a small DC motor which is a typical pager motor, with diameter of 6 mm and length of 10.4 mm, where it has limit voltage 3.6 V. Also, the body contains Li-ion polymer battery with 17.3x13.5x7 mm^3 which operates at 3.7 V with an energy storage capacity of 65 mAh, which is enough for 4 minutes of continuous operation of the robot. Selection of battery is significant for experiments, since it must give enough torque to have the robot power to sustain its motion. Lastly the battery must be rechargeable to ensure repeatability of the experiments.

Another part that is used in glass tube is the six legged switch of dimensions 7x3x3 mm^3 to connect the battery and the motor.

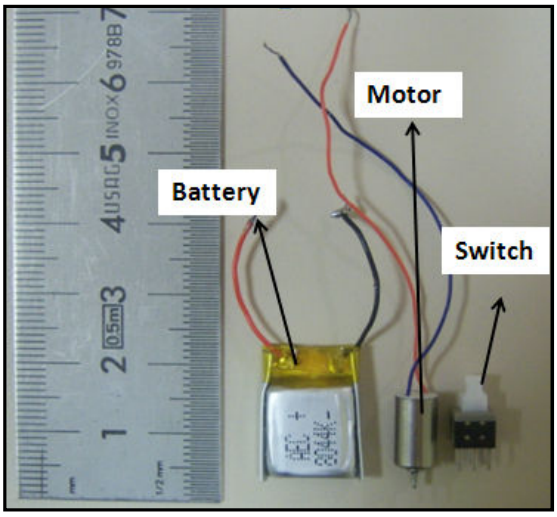

Figure 2.4: Electronical Devices in Glass Tube

The connection between motor and the tail is made with a plastic coupling material, which is constructed by drilling from opposite sides with respect to diameters of the motor shaft and the helical tail.

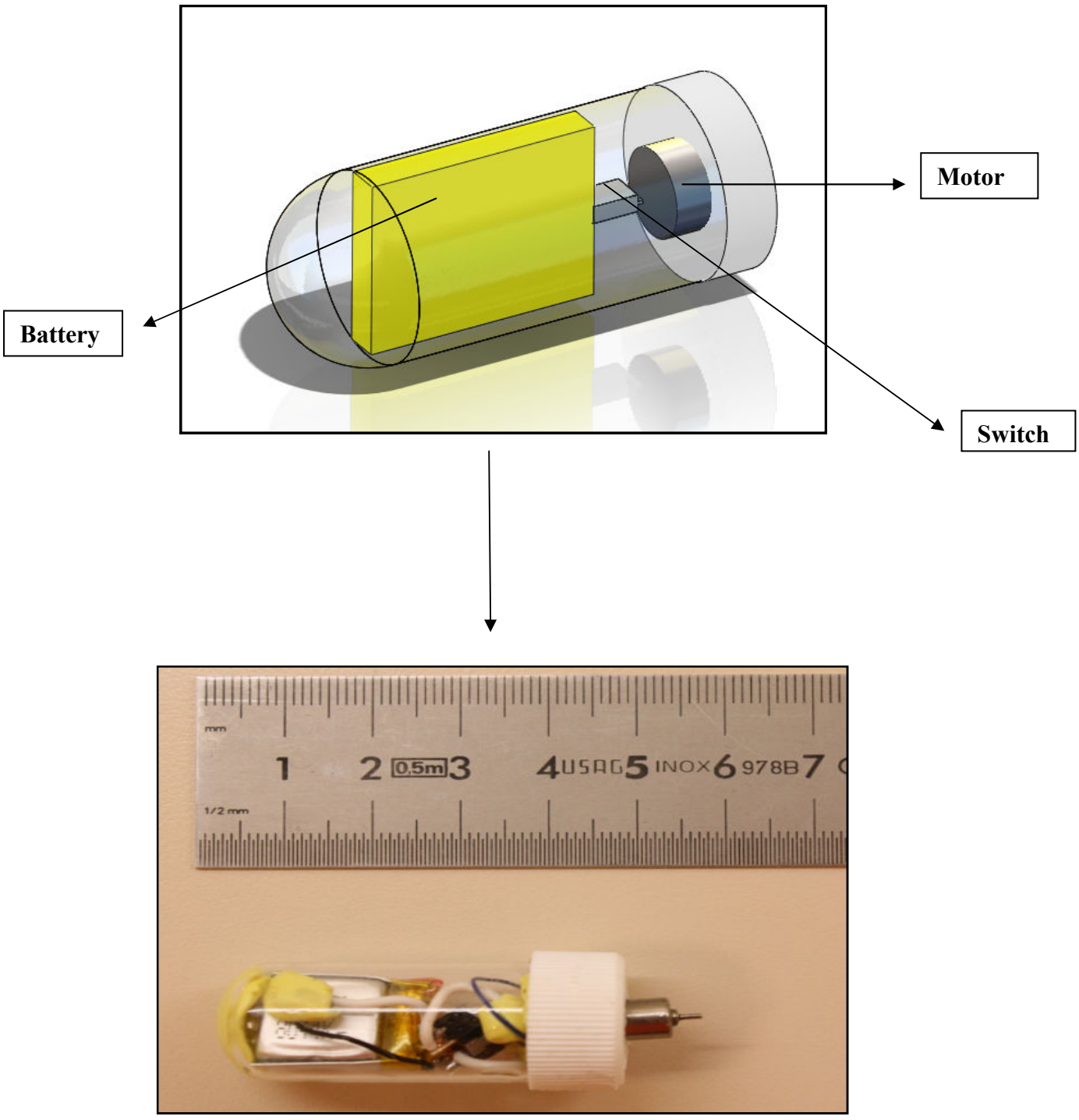

Figure 2.5: Assembly of parts in glass tube

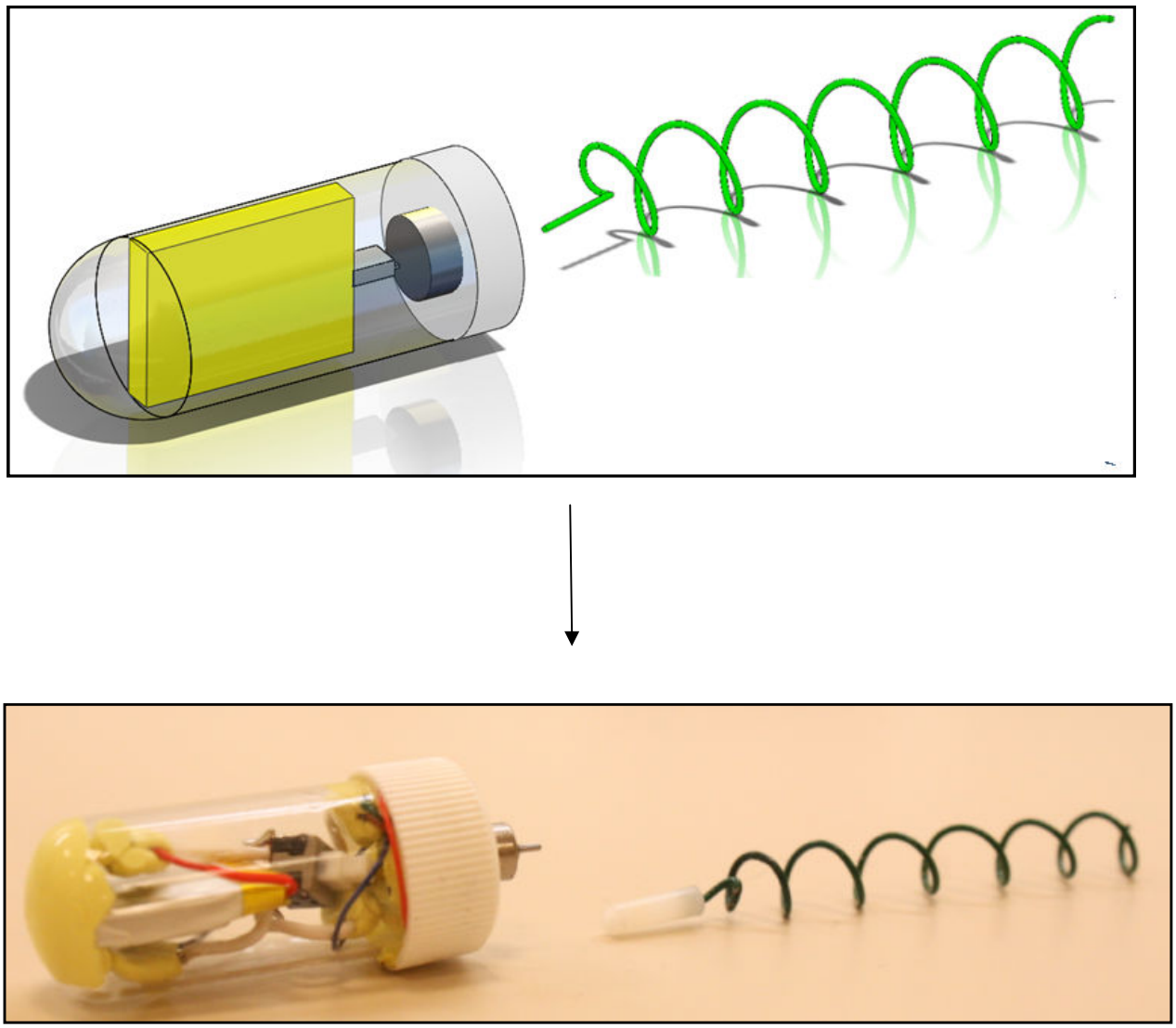

Figure 2.6: Assembly of Glass Tube and Helical Tail

Experiments are done with two channels as named Channel 1 and Channel 2 with 3.6 cm and 2.4 cm diameters, respectively.

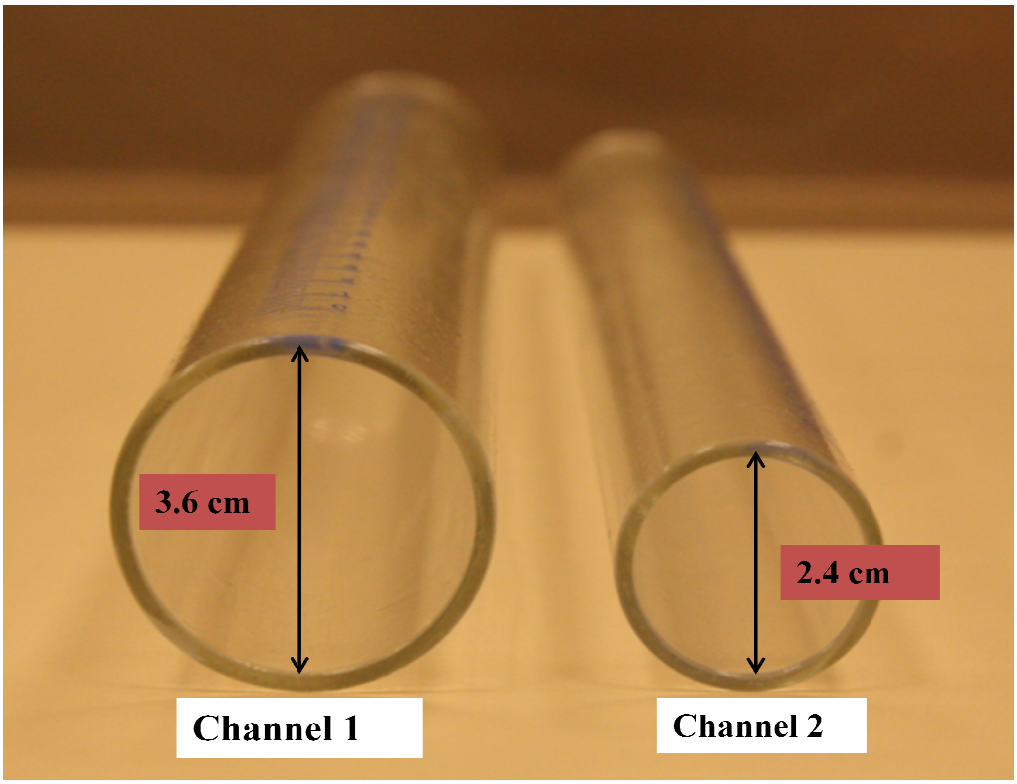

Figure 2.7: Channel 1 and Channel 2

The experiments are conducted in silicon oil to be in the Stokes regime. These are the macro experiments thus; increasing size must be compensated with increasing dynamic viscosity of the fluid.

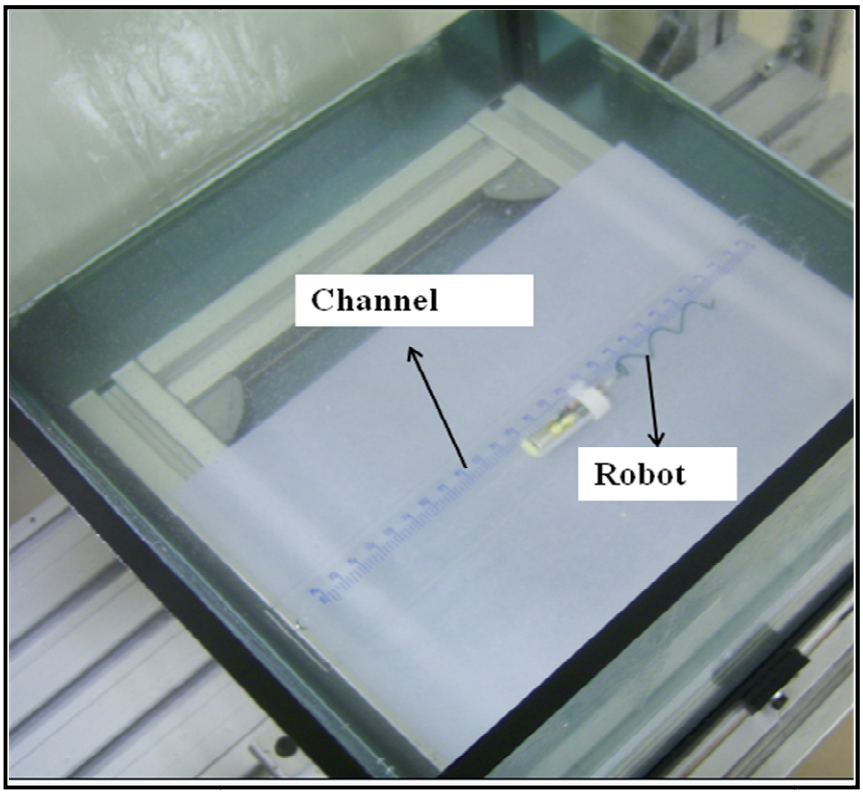

Figure 2.8: Setup

2.4.EXPERIMENTS

For each robot, forward speed and rotation rate are measured at least from three experiments for each channel.

The fully-charged battery is connected to the motor via the six legged switch and then they all put together into the bullet shaped glass tube, where the motor is settled in open ended side. The motor is fixed with the cover which has a hole matching the motor shaft diameter. Then selected helical tail is attached to motor shaft, switch is opened and efficient angular velocity is adjusted. After that, the swimming robot is placed inside a 30cm-long tube with a diameter of 36 mm or 24 mm. The tube is kept open-ended and placed inside a pool of silicone oil with dynamic viscosity of 5.6×10^{-3} Pa-s. Average linear, U, and angular, Ω, velocities, frequency, *f*, of the tail are calculated from 2-minute videos for each robot.

CHAPTER 3

DESCRIPTION OF THE MODEL

3.1. STOKES FLOW

Scaling issue is the dominant factor *in vivo* environments because the designs should have capability of reaching to body cavities currently inaccessible. As a result, Reynolds number becomes an important feature that:

$$Re = \frac{\rho UD}{\mu} \tag{3.1}$$

where ρ is the density of the fluid, U is the local velocity, D is the characteristic dimension of the object and, μ is the fluid dynamic viscosity.

Reynolds number is a dimensionless parameter, which is the ratio of inertial forces to viscous forces for the object. For instance, the Reynolds number for a human swimmer, where the inertial forces are dominant, is 10^4; for a microorganism, where the viscous forces are dominant, is typically 10^{-3}.

The motion of a Newtonian fluid is governed by Navier Stokes equation:

$$\rho \frac{\partial u}{\partial t} + \rho u.\nabla u = \mu \nabla^2 u - \nabla p \tag{3.2}$$

Objects with Reynolds number less than one are in the Stokes regime. In this regime viscous terms in Navier Stokes become dominant and the inertial terms are negligible; as a result, above equation becomes:

$$-\nabla p + \mu \nabla^2 u = 0 \tag{3.3}$$

This equation is known as Stokes equation and states that, in viscous regime, if there is no external force, pressure forces must be balanced with viscous ones.

3.2. REVERSIBILITY

By neglecting inertial terms in Navier Stokes equation, pressure and velocity becomes linearly proportional to each other, as it is seen in Stokes equation (3.3); thus, this linearity leads to reversible flow property in kinematic sense [1].

From Eq. (3.3) we get:

$$\nabla p = \mu \nabla^2 u \tag{3.4}$$

The corresponding x-momentum equation is:

$$\frac{\partial \mathrm{p}}{\partial \mathrm{x}} = \mu\left(\frac{\partial^2 u}{\partial x^2} + \frac{\partial^2 u}{\partial y^2}\right) \tag{3.5}$$

If u(x,y,z,t) and p(x,y,z,t) are the solution of equation (3.5), then –u(x,y,z,t) and –p(x,y,z,t) are also the solutions to this equation. The stress tensor is defined as:

$$\mathbf{T} = -p\mathbf{I} + \mu(\nabla \mathbf{u} + (\nabla \mathbf{u})^{\mathrm{T}}) \tag{3.6}$$

The integration of this tensor gives the force and when –u(x,y,z,t) and –p(x,y,z,t) solutions are used, then the stress tensor and the force vector also changes the sign from positive to negative. This is the reason for the reversibility of the Stokes flow.

Purcell [22] examined this reversibility issue by suggested two hinged mechanism which not make any reciprocal motion to produce net propulsion. He uses scallop as an example of a reciprocal motion that cannot produce non retracing motion due to its one hinge structure, thus it cannot propel itself in viscous regime. As a result, he concludes that the simplest animal that can swim in that regime is an animal with two hinges. As seen from Figure 3.1, this non reciprocal motion can be achieved by making movement such sequence: First θ_1 opens up and becomes θ_1' while θ_2 remains same, then θ_1' remains same while θ_2 opens up and becomes θ_2', third movement for non reciprocal motion must be closing θ_1' and becoming θ_1 while θ_2' remaining same and the last movement must be closing θ_2' and becoming θ_2 while θ_1 remaining same. These movement sequence produces a non reciprocal motion, thus this structure can propel itself in Stokes regime.

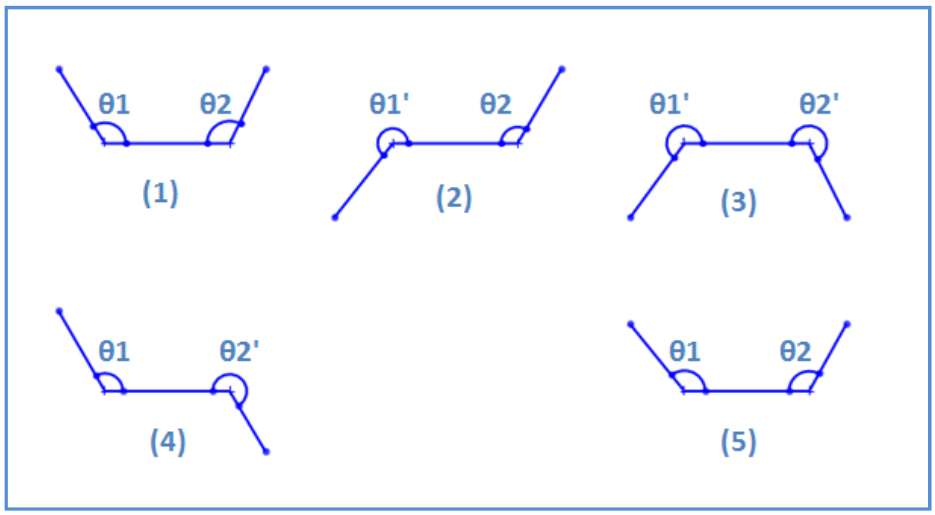

Figure 3.1: Two hinges non reciprocal system (1) Start position of structure; (2) θ_1 opens up, θ_2 remains same; (3) θ_1' remains same, θ_2' opens up; (4) θ_1' closes up, θ_2' remains same; (5) θ_2' closes up

3.3 RESISTIVE FORCE THEORY

It is generally accepted that bacteria propel themselves through fluids by rotating a flagellum or a flagellar and this motion can be created by viscous forces in Stokes regime. Because of the linearity feature of Stokes equations, Resistive Force Theory and Slender Body Theory can model an arbitrary 2D velocity field by superposition of Stokeslet and doublet functions.

Gray and Hancock [6] derive the Resistive Force Theory which is based on the principle that hydrodynamic forces are proportional to the local body velocity and this proportionality is defined as resistive force coefficient. On the other hand, there are some simplifications in this theory which leads to some uncertainties the results such that ignoring 'neighboring' and 'end' effects. By the 'neighboring' effect it is meant that, the force acts on the element of body by fluid is also affected by the neighboring waves. By the 'end' effect it is meant that, difference in measurements of resultant flow by an infinitely long flagellum and by a finite one.

Furthermore, Lighthill [6] modeled this velocity field by taken into account of the forces exerted on flagellum by the rest of it. In other words, he tried to model the true hydrodynamics for flagellar propulsion by considering the interaction between small flagellar segments. In RFT, the surrounding fluid is considered to be static while in SBT, this field is calculated self-consistently which leads to calculate interaction between small flagellar parts [21].

Although both of the theories have some limitations, they provide a good approach while modeling the helical propeller system. In this chapter, Resistive Force Theory is used to model this system by using Lighthill's resistive force coefficients. For more complicated motions like near wall, modified resistive force coefficients are used to verify the effect of wall interaction to the dynamic of the system.

3.3.1. Equations of Motion

Resistive Force Theory is developed by taking into account a small element of flagellum where hydrodynamic forces acted on this element are proportional to the local velocity with resistive force coefficient. To adopt this approach into helical movement of flagellum with a head, force free and torque free equation of motion are used to solve the 6-DOF system. In addition to that swimmer is modeled in a fluidic environment with no upstream velocity.

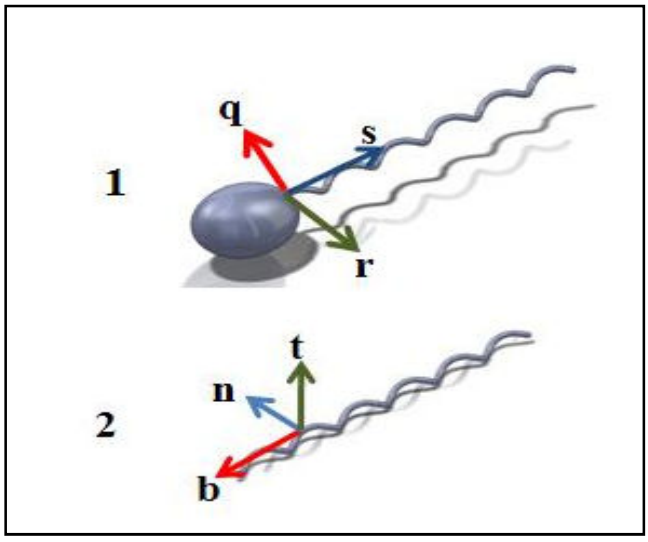

Figure 3.2: Frames attached to parts of swimmer: 1) Body coordinate frame of swimmer; 2) Local Frenet-Serret coordinate frame of helical tail

The motion of the left handed helix shaped slender tail is limited to the q and r axes, whose motions are given with sinusoidal wave equations as:

$$q(s,t) = B_q(s)\ \cos(\omega t - ks) \tag{3.7}$$

$$r(s,t) = B_r(s)\ \sin(\omega t - ks) \tag{3.8}$$

The above equations are depending on time, t, position on tail, s, angular velocity of tail, $\omega = 2\pi f$, wave number, $k = 2\pi L_{tail}/\lambda$ which L_{tail} is apparent tail length and λ is the wave pitch. In addition to amplitudes of B_q and B_r are depending on the position, s:

$$B_q(s) = B_q^{max}\ (1 - e^{-CS}) \tag{3.9}$$

$$B_r(s) = B_r^{max}\ (1 - e^{-CS}) \tag{3.10}$$

where, C is the envelope constant.

Position vector of tail with respect to body frame SQR, $\boldsymbol{P}^{SQR}$, is given as:

$$\boldsymbol{P}^{SQR} = \begin{bmatrix} s \\ q(s,t) \\ r(s,t) \end{bmatrix} = \begin{bmatrix} s \\ B_q(s)\ \cos(\omega t - ks) \\ B_r(s)\ \sin(\omega t - ks) \end{bmatrix} \tag{3.11}$$

3.3.1.1.Frenet Serret Formulas

In vector calculus, the Frenet-Serret formulas describe the kinematic properties of particle which moves along a continuous, differentiable curve in three-dimensional Euclidean-space R^3 [3].

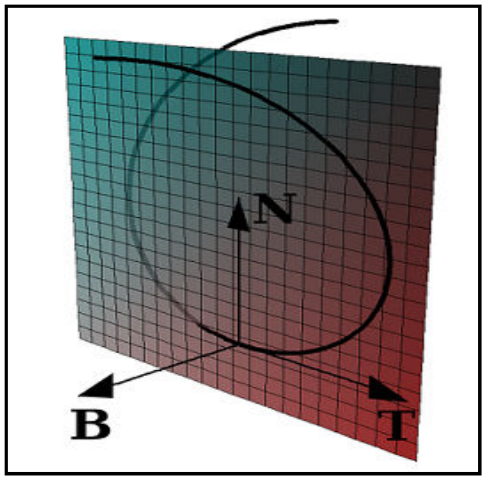

Figure 3.3: A space curve; the vectors **T**, **N** and **B**

These formulas apply to curves r(s) which are non-degenerate and parameterized by its arc length, as a result, the tangent, normal and binormal unit vectors can be explained as:

- **T** is the unit vector tangent to the curve which is pointing out of the trajectory
- **N** is the derivative of **T** with respect to arc length which is divided by its length
- **B** is the cross product of **T** and **N** unit vectors

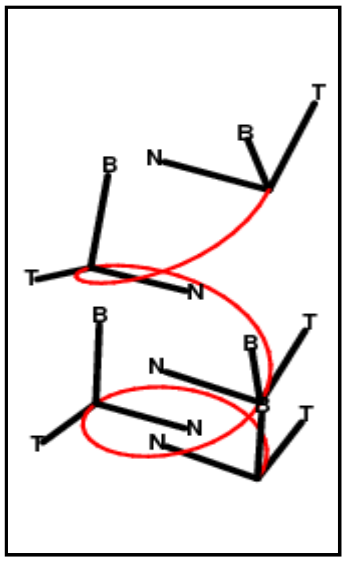

Figure 3.4: The Frenet-Serret frame moving along a helix space

Rotation matrix is derived from the local Frenet-Serret coordinates at tail's surface as:

$$\boldsymbol{t}(s) = \frac{\partial \boldsymbol{P}^{SQR}/\partial s}{||\partial \boldsymbol{P}^{SQR}/\partial s||} \tag{3.12}$$

$$\boldsymbol{b}(s) = \frac{(\partial \boldsymbol{P}^{SQR}/\partial s)\times(\partial^2 \boldsymbol{P}^{SQR}/\partial s^2)}{||(\partial \boldsymbol{P}^{SQR}/\partial s)\times(\partial^2 \boldsymbol{P}^{SQR}/\partial s^2)||} \tag{3.13}$$

$$\boldsymbol{n}(s) = \boldsymbol{b}(s) \times \boldsymbol{t}(s) \tag{3.14}$$

where ***t(s)*** represents unit tangent, ***b(s)*** represents unit binormal and ***n(s)*** represents unit normal vectors. In addition to that $\partial \boldsymbol{P}^{SQR}/\partial s$ equals to:

$$\frac{\partial \boldsymbol{P}^{SQR}}{\partial s} = \begin{bmatrix} \partial s/\partial s \\ \partial q(s,t)/\partial s \\ \partial r(s,t)/\partial s \end{bmatrix} = \begin{bmatrix} 0 \\ B_q(s)\, k \sin(\omega t - ks) \\ -B_r(s)\, k \cos(\omega t - ks) \end{bmatrix} \tag{3.15}$$

Thus, the rotation matrix from tail's local Frenet Serret to body *SQR*-frame can be written as:

$$\boldsymbol{R}_{BNT}^{SQR} = [\boldsymbol{b}(s) \quad \boldsymbol{n}(s) \quad \boldsymbol{t}(s)] \tag{3.16}$$

3.3.1.2.Forces and Torques Calculation on Tail's Surface

Forces on tail are exerted due to rotation of the helix and the rotation of the swimmer. Forces due to rotation of the helix are calculated, firstly. Velocity vector of tail with respect to body frame *SQR* can be found by taking derivative of the position vector with respect to time as:

$$\boldsymbol{U}_{\omega}^{SQR} = \frac{d\boldsymbol{P}^{SQR}}{dt} = \begin{bmatrix} 0 \\ -B_q(s)\omega \sin(\omega t - ks) \\ B_r(s)\omega \cos(\omega t - ks) \end{bmatrix} \tag{3.17}$$

where subscript ω denotes the contribution which is caused by rotation of helix.

Also, the velocity vector of tail can be expressed as:

$$\boldsymbol{U}_{\omega}^{BNT} = \begin{bmatrix} U_{\omega,b} \\ U_{\omega,n} \\ U_{\omega,t} \end{bmatrix} = \begin{bmatrix} \boldsymbol{U}_{\omega}^{SQR}.\boldsymbol{b}(s) \\ \boldsymbol{U}_{\omega}^{SQR}.\boldsymbol{n}(s) \\ \boldsymbol{U}_{\omega}^{SQR}.\boldsymbol{t}(s) \end{bmatrix} \tag{3.18}$$

Drag coefficient matrix for helical tail is:

$$\boldsymbol{C}_{nt} = \begin{bmatrix} -C_n & 0 & 0 \\ 0 & -C_n & 0 \\ 0 & 0 & -C_t \end{bmatrix} \tag{3.19}$$

where C_n and C_t represent normal and tangential resistive force coefficients, respectively.

Velocity vector in *BNT*-frame can be expressed in *SQR* body frame as:

$$\boldsymbol{U}_{\omega}^{BNT} = (\boldsymbol{R}_{BNT}^{SQR})^{-1}\boldsymbol{U}_{\omega}^{SQR} = (\boldsymbol{R}_{BNT}^{SQR})^{T}\,\boldsymbol{U}_{\omega}^{SQR} \tag{3.20}$$

Force and velocity vectors are related to each other with resistive force coefficient matrix and the force vector $d\boldsymbol{F}_{\omega}^{BNT}$ in *BNT*-frame can be expressed as:

$$d\boldsymbol{F}_{\omega}^{BNT} = \boldsymbol{C}_{nt}\boldsymbol{U}_{\omega}^{BNT}ds \tag{3.21}$$

$$d\boldsymbol{F}_{\omega}^{BNT} = \boldsymbol{C}_{nt}(\boldsymbol{R}_{BNT}^{SQR})^{T}\boldsymbol{U}_{\omega}^{SQR}ds \tag{3.22}$$

The force vector in body frame *SQR*, $d\boldsymbol{F}_{\omega}^{SQR}$ is:

$$d\boldsymbol{F}_{\omega}^{SQR} = \begin{bmatrix} dF_{\omega,s}^{SQR} \\ dF_{\omega,q}^{SQR} \\ dF_{\omega,r}^{SQR} \end{bmatrix} \tag{3.23}$$

$$d\boldsymbol{F}_{\omega}^{SQR} = \boldsymbol{R}_{BNT}^{SQR}d\boldsymbol{F}_{\omega}^{BNT} \tag{3.24}$$

$$d\boldsymbol{F}_{\omega}^{SQR} = \boldsymbol{R}_{BNT}^{SQR}\boldsymbol{C}_{nt}(\boldsymbol{R}_{BNT}^{SQR})^{T}\boldsymbol{U}_{\omega}^{SQR}ds \tag{3.25}$$

Total force vector $\boldsymbol{F}_{\omega}^{SQR}$ in *SQR*-frame is found by integrated the Eq. (3.25) over all tail length:

$$\boldsymbol{F}_{\omega}^{SQR} = \int_{0}^{L_{tail}} \boldsymbol{R}_{BNT}^{SQR}\boldsymbol{C}_{nt}(\boldsymbol{R}_{BNT}^{SQR})^{T}\boldsymbol{U}_{\omega}^{SQR}ds \tag{3.26}$$

Another force is added to tail due to rotation of the swimmer. Angular velocity vector, $\boldsymbol{\Omega}_{tail}^{SQR}$ in *SQR*-frame:

$$\Omega_{tail}^{SQR} = \begin{bmatrix} \Omega_{tail}^{s} \\ \Omega_{sw}^{q} \\ \Omega_{sw}^{r} \end{bmatrix} = \begin{bmatrix} 0 \\ \Omega_{sw}^{q} \\ \Omega_{sw}^{r} \end{bmatrix} \tag{3.27}$$

where subscript '*tail*' denotes the helical tail and '*sw*' denotes the swimmer.

The linear velocity vector, due to rigid body rotation of the swimmer:

$$\dot{\boldsymbol{P}}^{SQR} = \Omega_{sw}^{SQR} \times \boldsymbol{P}^{SQR} = \begin{bmatrix} r(s,t)\,\Omega_{sw}^{q} - q(s,t)\,\Omega_{sw}^{r} \\ -r(s,t)\,\Omega_{tail}^{s} + s\,\Omega_{sw}^{r} \\ q(s,t)\,\Omega_{tail}^{s} - s\,\Omega_{sw}^{q} \end{bmatrix} \tag{3.28}$$

This vector can be decomposed into:

$$\dot{\boldsymbol{P}}^{SQR} = \boldsymbol{Q}^{SQR}\Omega_{tail}^{SQR} = \begin{bmatrix} 0 & r(s,t) & -q(s,t) \\ -r(s,t) & 0 & s \\ q(s,t) & -s & 0 \end{bmatrix} \begin{bmatrix} \Omega_{tail}^{s} \\ \Omega_{sw}^{q} \\ \Omega_{sw}^{r} \end{bmatrix} \tag{3.29}$$

in which $\boldsymbol{Q}^{SQR}$ is skew symmetric matrix.

Thus, the drag force vector on tail, $d\boldsymbol{F}_{\Omega}^{SQR}$, due to rotation of the swimmer in *SQR*-frame can be expressed as:

$$d\boldsymbol{F}_{\Omega}^{SQR} = \begin{bmatrix} dF_{\Omega,s}^{SQR} \\ dF_{\Omega,q}^{SQR} \\ dF_{\Omega,r}^{SQR} \end{bmatrix} \tag{3.30}$$

$$d\boldsymbol{F}_{\Omega}^{SQR} = \boldsymbol{R}_{BNT}^{SQR}\boldsymbol{C}_{nt}(\boldsymbol{R}_{BNT}^{SQR})^{T}\dot{\boldsymbol{P}}^{SQR}ds \tag{3.31}$$

$$d\boldsymbol{F}_{\Omega}^{SQR} = \boldsymbol{R}_{BNT}^{SQR}\boldsymbol{C}_{nt}(\boldsymbol{R}_{BNT}^{SQR})^{T}\boldsymbol{Q}^{SQR}\Omega_{tail}^{SQR}ds \tag{3.32}$$

Total force vector, $\boldsymbol{F}_{\Omega}^{SQR}$, in *SQR*-frame is found by integrating Eq. (3.32) over all tail:

$$\boldsymbol{F}_{\Omega}^{SQR} = \left(\int_{0}^{L_{tail}} \boldsymbol{R}_{BNT}^{SQR}\boldsymbol{C}_{nt}(\boldsymbol{R}_{BNT}^{SQR})^{T}\boldsymbol{Q}^{SQR}ds\right)\Omega_{tail}^{SQR} \tag{3.33}$$

Three dimensional hydrodynamic torque values on tail are exerted also due to rotation of the helix and the rotation of the swimmer.

Propulsion torque due to rotation of the helix $d\boldsymbol{T}_{\omega}^{SQR}$ is calculated to begin with.

$$d\boldsymbol{T}_{\omega}^{SQR} = \boldsymbol{P}^{SQR} \times d\boldsymbol{F}_{\omega}^{SQR} = \begin{bmatrix} dF_{\omega,r}^{SQR} q(s,t) - dF_{\omega,q}^{SQR} r(s,t) \\ -dF_{\omega,r}^{SQR} s \quad + dF_{\omega,s}^{SQR} r(s,t) \\ dF_{\omega,q}^{SQR} s \quad - dF_{\omega,s}^{SQR} q(s,t) \end{bmatrix} \tag{3.34}$$

and $d\boldsymbol{T}_{\omega}{}^{SQR}$ vector can be decomposed into:

$$d\boldsymbol{T}_{\omega}^{SQR} = -\boldsymbol{Q}^{SQR} d\boldsymbol{F}_{\omega}^{SQR} = (\boldsymbol{Q}^{SQR})^{T} d\boldsymbol{F}_{\omega}^{SQR} = \begin{bmatrix} 0 & -r(s,t) & q(s,t) \\ r(s,t) & 0 & -s \\ -q(s,t) & s & 0 \end{bmatrix} \begin{bmatrix} dF_{\omega,s}^{SQR} \\ dF_{\omega,q}^{SQR} \\ dF_{\omega,r}^{SQR} \end{bmatrix} \tag{3.35}$$

Thus, $d\boldsymbol{T}_{\omega}{}^{SQR}$ vector is:

$$d\boldsymbol{T}_{\omega}^{SQR} = (\boldsymbol{Q}^{SQR})^{T} \boldsymbol{R}_{BNT}^{SQR} \boldsymbol{C}_{nt} (\boldsymbol{R}_{BNT}^{SQR})^{T} \boldsymbol{U}_{\omega}^{SQR} ds \tag{3.36}$$

Total propulsion torque vector in *SQR*-frame is found by integrating Eq. (3.36) over all tail:

$$\boldsymbol{T}_{\omega}^{SQR} = \int_{0}^{L_{tail}} (\boldsymbol{Q}^{SQR})^{T} \boldsymbol{R}_{BNT}^{SQR} \boldsymbol{C}_{nt} (\boldsymbol{R}_{BNT}^{SQR})^{T} \boldsymbol{U}_{\omega}^{SQR} ds \tag{3.37}$$

Another torque vector, which is drag torque, is added to tail due to rotation of the swimmer.

$$d\boldsymbol{T}_{\Omega}^{SQR} = \boldsymbol{P}^{SQR} \times d\boldsymbol{F}_{\Omega}^{SQR} = \begin{bmatrix} dF_{\Omega,r}^{SQR} q(s,t) - dF_{\Omega,q}^{SQR} r(s,t) \\ -dF_{\Omega,r}^{SQR} s \quad + dF_{\Omega,s}^{SQR} r(s,t) \\ dF_{\Omega,q}^{SQR} s \quad - dF_{\Omega,s}^{SQR} q(s,t) \end{bmatrix} \tag{3.38}$$

and $d\boldsymbol{T}_{\Omega}{}^{SQR}$ vector can be decomposed into:

$$d\boldsymbol{T}_{\Omega}^{SQR} = -\boldsymbol{Q}^{SQR} d\boldsymbol{F}_{\Omega}^{SQR} = (\boldsymbol{Q}^{SQR})^{T} d\boldsymbol{F}_{\Omega}^{SQR} = \begin{bmatrix} 0 & -r(s,t) & q \\ r(s,t) & 0 & -s \\ -q(s,t) & s & 0 \end{bmatrix} \begin{bmatrix} dF_{\Omega,s}^{SQR} \\ dF_{\Omega,q}^{SQR} \\ dF_{\Omega,r}^{SQR} \end{bmatrix} \tag{3.40}$$

Thus, $d\boldsymbol{T}_{\Omega}{}^{SQR}$ vector is:

$$d\boldsymbol{T}_{\Omega}^{SQR} = (\boldsymbol{Q}^{SQR})^{T} \boldsymbol{R}_{BNT}^{SQR} \boldsymbol{C}_{nt} (\boldsymbol{R}_{BNT}^{SQR})^{T} \boldsymbol{Q}^{SQR} \Omega_{tail}^{SQR} ds \tag{3.41}$$

and total drag torque vector in *SQR*-frame is found by integrating the Eq. (3.41) over all tail:

$$\boldsymbol{T}_{\Omega}^{SQR} = (\int_{0}^{L_{tail}} (\boldsymbol{Q}^{SQR})^{T} \boldsymbol{R}_{BNT}^{SQR} \boldsymbol{C}_{nt} (\boldsymbol{R}_{BNT}^{SQR})^{T} \boldsymbol{Q}^{SQR} ds) \Omega_{tail}^{SQR} \tag{3.42}$$

In order to calculate the components of the tail's mobility matrices, point-wise contribution of the local resistive force coefficients on the body frame should be calculated as and can be seen in Appendix A:

$$\boldsymbol{C}_{RCR} = \boldsymbol{R}_{BNT}^{SQR} \boldsymbol{C}_{nt} \left(\boldsymbol{R}_{BNT}^{SQR}\right)^{T} \tag{3.43}$$

Thus, the components of the tail's mobility matrices can be expressed as:

$$\boldsymbol{C}_U^F = \int_0^{L_{tail}} \boldsymbol{C}_{RCR}\, ds \tag{3.44}$$

$$\boldsymbol{C}_\omega^F = \int_0^{L_{tail}} \boldsymbol{C}_{RCR}\, \boldsymbol{Q}^{SQR}\, ds \tag{3.45}$$

$$\boldsymbol{C}_U^T = \int_0^{L_{tail}} (\boldsymbol{Q}^{SQR})^T\, \boldsymbol{C}_{RCR}\, ds \tag{3.46}$$

$$\boldsymbol{C}_\omega^T = \int_0^{L_{tail}} (\boldsymbol{Q}^{SQR})^T\, \boldsymbol{C}_{RCR}\, \boldsymbol{Q}^{SQR} ds \tag{3.47}$$

where *U* denotes the contribution from linear velocities and ω denotes the contribution from the angular velocities.

Thus, the resultant force on tail surface due to rotation of the helix and swimmer can be expressed as:

$$\boldsymbol{F}_{tail}^{SQR} = \boldsymbol{F}_\omega^{SQR} + \boldsymbol{F}_\Omega^{SQR} \tag{3.48}$$

$$\boldsymbol{F}_{tail}^{SQR} = \boldsymbol{C}_U^F\, \boldsymbol{U}_\omega^{SQR} + \boldsymbol{C}_\omega^F\, \Omega_{tail}^{SQR} \tag{3.49}$$

In addition to that, the resultant torque on tail surface due to rotation of helix and swimmer can be expressed as:

$$\boldsymbol{T}_{tail}^{SQR} = \boldsymbol{T}_\omega^{SQR} + \boldsymbol{T}_\Omega^{SQR} \tag{3.50}$$

$$\boldsymbol{T}_{tail}^{SQR} = \boldsymbol{C}_U^T\, \boldsymbol{U}_\omega^{SQR} + \boldsymbol{C}_\omega^F\, \Omega_{tail}^{SQR} \tag{3.51}$$

Thus, this linear relationship between force (torque) and velocity can be expressed in matrix as:

$$\begin{bmatrix} \boldsymbol{F}_{tail}^{SQR} \\ \boldsymbol{T}_{tail}^{SQR} \end{bmatrix} = \begin{bmatrix} \boldsymbol{C}_U^F & \boldsymbol{C}_\omega^F \\ \boldsymbol{C}_U^T & \boldsymbol{C}_\omega^T \end{bmatrix} \begin{bmatrix} \boldsymbol{U}_\omega^{SQR} \\ \Omega_{tail}^{SQR} \end{bmatrix} \tag{3.52}$$

3.3.1.3.Forces and Torques Calculation on Body's Surface

Due to translational and rotational motion of the body, both kinds of drag forces are exerted on this part of the helical propeller system. Also, the linear relationship between the force (torque) and the velocity with drag coefficient is also valid for the body part of helical propeller.

Linear velocity vector of body on *SQR*-frame is

$$\boldsymbol{U}_{body}^{SQR} = \begin{bmatrix} U_{sw}^s \\ U_{sw}^q \\ U_{sw}^r \end{bmatrix} \tag{3.53}$$

where subscript '*body*' denotes the head part of the helical propeller system. Angular velocity vector of body on *SQR*-frame is:

$$\Omega_{body}^{SQR} = \begin{bmatrix} \Omega_{body}^{s} \\ \Omega_{sw}^{q} \\ \Omega_{sw}^{r} \end{bmatrix} \tag{3.54}$$

The body part of the prototype is not spherical but it almost has the elliptical shape. Thus, the analytical solution which is given in Berg study for this kind of geometrical structure can be used [43].

Linear drag coefficient exerts on the body part due to translational motion of system is:

$$\boldsymbol{D}_U^F = \begin{bmatrix} 4\pi\mu b/[ln(2b/a) - 1/2] & 0 & 0 \\ 0 & 8\pi\mu b/[ln(2b/a) + 1/2] & 0 \\ 0 & 0 & 8\pi\mu b/[ln(2b/a) + 1/2] \end{bmatrix} \tag{3.55}$$

Rotational drag coefficient exerts on the body part due to rotational motion of the system is:

$$\boldsymbol{D}_\omega^T = \begin{bmatrix} (16/3)\pi\mu a^2 b & 0 & 0 \\ 0 & 8\pi\mu a^3/[ln(2b/a) - 1/2] & 0 \\ 0 & 0 & 8\pi\mu a^3/[ln(2b/a) - 1/2] \end{bmatrix} \tag{3.56}$$

In equations (3.55) and (3.56) μ is the dynamic viscosity of the fluid, a is semi-minor and b is semi-major axis of the elliptical body. Assuming that the center of mass swimmer is very close to center of mass of this elliptical body then, drag force exerts on this structure can be calculated as:

$$\boldsymbol{F}_{body}^{SQR} = \boldsymbol{D}_U^F \, \boldsymbol{U}_{body}^{SQR} \tag{3.57}$$

Likewise, drag torque exerts on elliptical body can be calculated as:

$$\boldsymbol{T}_{body}^{SQR} = \boldsymbol{D}_\omega^T \, \boldsymbol{\omega}_{body}^{SQR} \tag{3.58}$$

Thus, this linear relationship between force and velocity can be expressed in matrix as:

$$\begin{bmatrix} \boldsymbol{F}_{body}^{SQR} \\ \boldsymbol{T}_{body}^{SQR} \end{bmatrix} = \begin{bmatrix} \boldsymbol{D}_U^F & 0 \\ 0 & \boldsymbol{D}_\omega^T \end{bmatrix} \begin{bmatrix} \boldsymbol{U}_{body}^{SQR} \\ \boldsymbol{\omega}_{body}^{SQR} \end{bmatrix} \tag{3.59}$$

3.3.1.4.Quaternion

A quaternion is a collection of four real parameters of which the first is considered a scalar and the last three a vector 3D space. This quaternion vector can be represented as:

$$[s, v] = s + v_x \hat{\boldsymbol{\imath}} + v_y \hat{\boldsymbol{\jmath}} + v_z \hat{\boldsymbol{k}} \tag{3.60}$$

Using quaternion is a better way to represent the rotations than using 3-by-3 rotation matrices. They are using for easy and better interpolation, avoiding singularities and reaching more stable systems.

Because the rotation sequence cannot be partioned into *S*, *Q*, and *R*-frames, complex rotations of swimmer, oriented it with respect to *XYZ* Newtonian reference frame can only be handled by quaternions. Thus, the quaternion matrix from body's *SQR*-frame to *XYZ* Newtonian-reference frame can be represented as:

$$\boldsymbol{q}_{SQR}^{XYZ} = [q_{s0} \quad q_{v1} \quad q_{v2} \quad q_{v3}] \tag{3.61}$$

To calculate this $\boldsymbol{q}_{SQR}^{XYZ}$ matrix, $\dot{\boldsymbol{q}}_{SQR}^{XYZ}$ must be integrated over time to obtain current quaternion at each time [44].

$$\dot{q}_{s0} = -\left(\Omega_{sw}^{s} q_{v1} + \Omega_{sw}^{q} q_{v2} + \Omega_{sw}^{r} q_{v3}\right)/2 \tag{3.62}$$

$$\begin{bmatrix} \dot{q}_{v1} \\ \dot{q}_{v2} \\ \dot{q}_{v3} \end{bmatrix} = \begin{bmatrix} \Omega_{sw}^{s} q_{s0} + \Omega_{sw}^{q} q_{v3} - \Omega_{sw}^{r} q_{v2} \\ \Omega_{sw}^{q} q_{s0} + \Omega_{sw}^{r} q_{v1} - \Omega_{sw}^{s} q_{v3} \\ \Omega_{sw}^{r} q_{s0} + \Omega_{sw}^{s} q_{v2} - \Omega_{sw}^{q} q_{v1} \end{bmatrix} \tag{3.63}$$

By using this quaternion matrix corresponding instantaneous rotation matrix can be expressed as:

$$\boldsymbol{R}_{SQR}^{XYZ} = \begin{bmatrix} 1 - 2(q_{v2})^2 - 2(q_{v3})^2 & 2q_{v1}q_{v2} - 2q_{v3}q_{s0} & 2q_{v1}q_{v3} + 2q_{v2}q_{s0} \\ 2q_{v1}q_{v2} + 2q_{v3}q_{s0} & 1 - 2(q_{v1})^2 - 2(q_{v3})^2 & 2q_{v2}q_{v3} - 2q_{v1}q_{s0} \\ 2q_{v1}q_{v3} - 2q_{v2}q_{s0} & 2q_{v2}q_{v3} + 2q_{v1}q_{s0} & 1 - 2(q_{v1})^2 - 2(q_{v2})^2 \end{bmatrix} \tag{3.64}$$

For transformations $\boldsymbol{R}_{SQR}^{XYZ}$ matrix is used and because it is a rotation matrix, the relationship $\boldsymbol{R}_{SQR}^{XYZ^{-1}} = \boldsymbol{R}_{SQR}^{XYZ^{T}}$ can be invoked. With the help of this property, to obtain the tail's mobility matrices' transformation to *xyz*, Newtonian-reference frame, these calculations are needed as:

$$\boldsymbol{C}_{U}^{F,XYZ} = \boldsymbol{R}_{SQR}^{XYZ}\, \boldsymbol{C}_{U}^{F}\, \boldsymbol{R}_{SQR}^{XYZ^{T}} \tag{3.65}$$

$$\boldsymbol{C}_{\omega}^{F,XYZ} = \boldsymbol{R}_{SQR}^{XYZ}\, \boldsymbol{C}_{\omega}^{F}\, \boldsymbol{R}_{SQR}^{XYZ^{T}} \tag{3.66}$$

$$\boldsymbol{C}_{U}^{T,XYZ} = \boldsymbol{R}_{SQR}^{XYZ}\, \boldsymbol{C}_{U}^{T}\, \boldsymbol{R}_{SQR}^{XYZ^{T}} \tag{3.67}$$

$$\boldsymbol{C}_{\omega}^{T,XYZ} = \boldsymbol{R}_{SQR}^{XYZ}\, \boldsymbol{C}_{\omega}^{T}\, \boldsymbol{R}_{SQR}^{XYZ^{T}} \tag{3.68}$$

Transformation of forces and torques on tail's surface from *SQR* to *XYZ*-frame can be represented by:

$$\boldsymbol{F}_{tail}^{XYZ} = \boldsymbol{R}_{SQR}^{XYZ}\, \boldsymbol{F}_{tail}^{SQR} \tag{3.69}$$

$$\boldsymbol{T}_{tail}^{XYZ} = \boldsymbol{R}_{SQR}^{XYZ}\, \boldsymbol{T}_{tail}^{SQR} \tag{3.70}$$

3.3.2.Dynamics of the Helical Propeller System's Motion

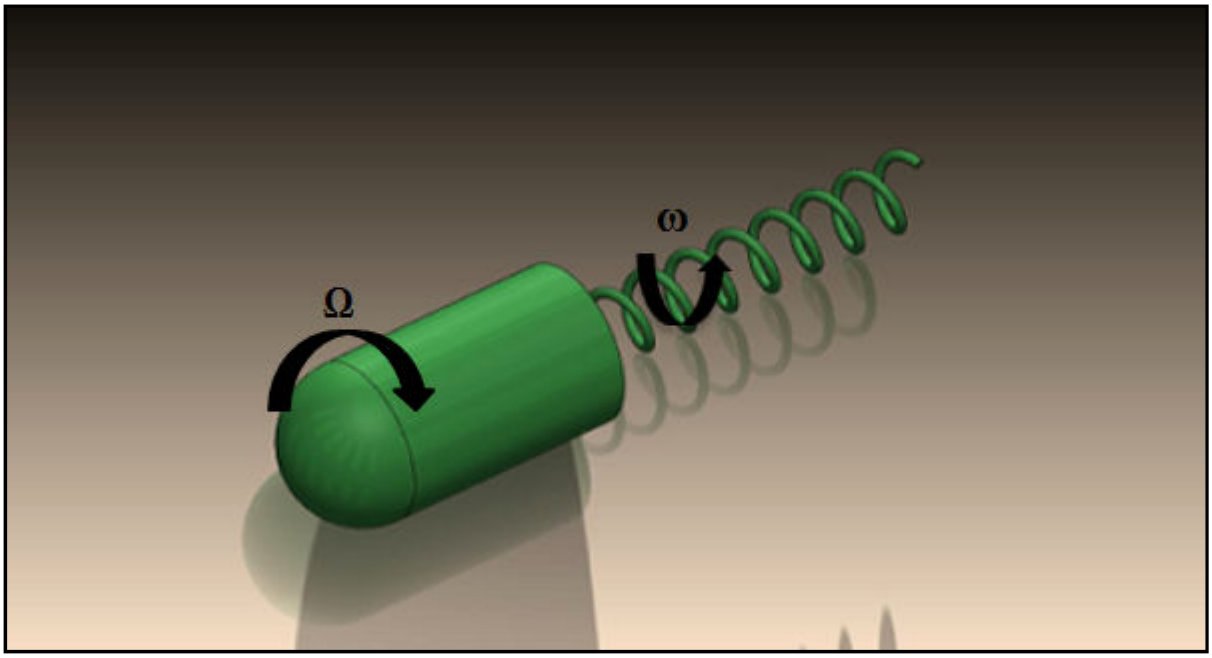

Figure 3.5: Helical Propeller System Body and Tail Rotation Directions

In general, because of torque-free and force-free motion assumption, both the resultant force and torque act on the system must vanish. Consider a system, with head and a flagellum, swimming in Stokes regime by helical propeller. Assuming that helical flagellum is twisted in counter clockwise direction, thus, forward propulsion is ensured if tail rotates in clockwise and body rotates in counter clockwise directions when swimmer as seen from front. If the twisted direction is reversed, rotation directions of tail and body must be reversed for forward propulsion.

First of all, helical propeller's head and tail start to rotate clockwise direction. On the other hand, an additional counter torque is exerted on system because of viscous fluid. This counter torque reduces the angular velocity of tail relative to *xyz* reference frame which leads to reduce of both propulsive force and torque. Due to counter torque, body starts to rotate in counter clockwise direction. In other words, motor's angular velocity of $2\pi f + \Omega$ is divided between body and tail such as Ω and $2\pi f$, respectively. When the tail reaches an induced angular velocity of $2\pi f$, exerting net force and torque on helical propeller system vanish and system becomes steady periodic.

The system is modeled with respect to an observer who is residing on the revolute joint between the body and the tail. Thus, force free and torque free dynamics result in getting six equations with six unknowns.

Propulsion force and torque are exerted on tail can be written the multiplication of mobility matrices and the velocity vector of tail as:

$$\begin{bmatrix} \boldsymbol{F}_{propulsion_{(3x1)}} \\ \boldsymbol{T}_{propulsion_{(3x1)}} \end{bmatrix}_{(6x1)} = \begin{bmatrix} \boldsymbol{C}_U^F & \boldsymbol{C}_\omega^F \\ \boldsymbol{C}_U^T & \boldsymbol{C}_\omega^T \end{bmatrix}_{(6x6)} \begin{bmatrix} 0 \\ 0 \\ 0 \\ 2\pi f \\ 0 \\ 0 \end{bmatrix}_{(6x1)} \tag{3.71}$$

Drag force and torque are exerted on the system can be written multiplication of the drag coefficient matrix and the velocity vector of the body as:

$$\begin{bmatrix} \boldsymbol{F}_{Drag_{(3x1)}} \\ \boldsymbol{T}_{Drag_{(3x1)}} \end{bmatrix}_{(6x1)} = \left(\begin{bmatrix} \boldsymbol{C}_U^{F,mod} & \boldsymbol{C}_\omega^{F,mod} \\ \boldsymbol{C}_U^{T,mod} & \boldsymbol{C}_\omega^{T,mod} \end{bmatrix}_{(6x6)} + \begin{bmatrix} \boldsymbol{D}_U^F & 0 \\ 0 & \boldsymbol{D}_\omega^T \end{bmatrix}_{(6x6)} \right) \begin{bmatrix} U_{sw}^s \\ U_{sw}^q \\ U_{sw}^r \\ \Omega_{body}^s \\ \Omega_{sw}^q \\ \Omega_{sw}^r \end{bmatrix}_{(6x1)} \tag{3.72}$$

In $\begin{bmatrix} \boldsymbol{C}_U^{F,mod} & \boldsymbol{C}_\omega^{F,mod} \\ \boldsymbol{C}_U^{T,mod} & \boldsymbol{C}_\omega^{T,mod} \end{bmatrix}$ matrix, as the frequency is given into the system as an input, the fourth row's and column's elements are zero. As it is mentioned above, net force and torque vanish on the helical propeller system, thus:

$$\begin{bmatrix} \boldsymbol{F}_{propulsion_{(3x1)}} \\ \boldsymbol{T}_{propulsion_{(3x1)}} \end{bmatrix}_{(6x1)} + \begin{bmatrix} \boldsymbol{F}_{Drag_{(3x1)}} \\ \boldsymbol{T}_{Drag_{(3x1)}} \end{bmatrix}_{(6x1)} = \boldsymbol{0} \tag{3.73}$$

This leads to the equation system with six unknowns, as:

$$\begin{bmatrix} \boldsymbol{C}_U^F & \boldsymbol{C}_\omega^F \\ \boldsymbol{C}_U^T & \boldsymbol{C}_\omega^T \end{bmatrix}_{(6x6)} \begin{bmatrix} 0 \\ 0 \\ 0 \\ 2\pi f \\ 0 \\ 0 \end{bmatrix}_{(6x1)} + \left(\begin{bmatrix} \boldsymbol{C}_U^{F,mod} & \boldsymbol{C}_\omega^{F,mod} \\ \boldsymbol{C}_U^{T,mod} & \boldsymbol{C}_\omega^{T,mod} \end{bmatrix}_{(6x6)} + \begin{bmatrix} \boldsymbol{D}_U^F & 0 \\ 0 & \boldsymbol{D}_\omega^T \end{bmatrix}_{(6x6)} \right) \begin{bmatrix} U_{sw}^s \\ U_{sw}^q \\ U_{sw}^r \\ \Omega_{body}^s \\ \Omega_{sw}^q \\ \Omega_{sw}^r \end{bmatrix}_{(6x1)} = \boldsymbol{0}$$

(3.74)

Also:

$$\begin{bmatrix} \boldsymbol{C}_U^F & \boldsymbol{C}_\omega^F \\ \boldsymbol{C}_U^T & \boldsymbol{C}_\omega^T \end{bmatrix}_{(6x6)} \begin{bmatrix} 0 \\ 0 \\ 0 \\ 2\pi f \\ 0 \\ 0 \end{bmatrix}_{(6x1)} = -\left(\begin{bmatrix} \boldsymbol{C}_U^{F,mod} & \boldsymbol{C}_\omega^{F,mod} \\ \boldsymbol{C}_U^{T,mod} & \boldsymbol{C}_\omega^{T,mod} \end{bmatrix}_{(6x6)} + \begin{bmatrix} \boldsymbol{D}_U^F & 0 \\ 0 & \boldsymbol{D}_\omega^T \end{bmatrix}_{(6x6)} \right) \begin{bmatrix} U_{sw}^s \\ U_{sw}^q \\ U_{sw}^r \\ \Omega_{body}^s \\ \Omega_{sw}^q \\ \Omega_{sw}^r \end{bmatrix}_{(6x1)}$$

(3.75)

As a result, multiplying the left hand side with the inverse of the drag coefficient matrix leads to find the unknowns matrix $[U_{sw}^s \quad U_{sw}^q \quad U_{sw}^r \quad \Omega_{body}^s \quad \Omega_{sw}^q \quad \Omega_{sw}^r]'$ such as:

$$\left(-\left(\begin{bmatrix} \boldsymbol{C}_U^{F,mod} & \boldsymbol{C}_\omega^{F,mod} \\ \boldsymbol{C}_U^{T,mod} & \boldsymbol{C}_\omega^{T,mod} \end{bmatrix} + \begin{bmatrix} \boldsymbol{D}_U^F & 0 \\ 0 & \boldsymbol{D}_\omega^T \end{bmatrix} \right) \right)^{-1} \begin{bmatrix} \boldsymbol{C}_U^F & \boldsymbol{C}_\omega^F \\ \boldsymbol{C}_U^T & \boldsymbol{C}_\omega^T \end{bmatrix} \begin{bmatrix} 0 \\ 0 \\ 0 \\ 2\pi f \\ 0 \\ 0 \end{bmatrix} = \begin{bmatrix} U_{sw}^s \\ U_{sw}^q \\ U_{sw}^r \\ \Omega_{body}^s \\ \Omega_{sw}^q \\ \Omega_{sw}^r \end{bmatrix} \tag{3.76}$$

Therefore, the linear velocity and angular velocity vector in *XYZ*-frame can be expressed as:

$$U^{XYZ} = R_{SQR}^{XYZ} U^{SQR} \tag{3.77}$$

$$\Omega^{XYZ} = R_{SQR}^{XYZ} \Omega^{SQR} \tag{3.78}$$

3.3.3. RESISTIVE FORCE COEFFICIENTS

3.3.3.1.Lighthill's Resistive Force Coefficients

Lighthill [8] derives a numerical method as Slender Body Theory, to predict the performance of flagellar propulsion. He applied his method to eukaryotic flagellum with helical propeller and then he proves that this method is also valid for prokaryotic flagellum.

As it is mentioned above that, when he models this velocity field, which is created by helical flagella motion, he has taken into account of the forces exerting on flagellum by the rest of it. In other words, he considers the neighboring effect that the force acts on the element of the flagellum by fluid is affected by the neighboring waves, too. On the other hand, he neglects the anomalies which are caused by the helical flagellum tips' end effects.

He begins his analysis by zero thrust limit, where calculating the performance of the flagellum without considering any effects from the cell body. He uses Stokeslet to calculate this force that, Stokeslet represents one single point force on to fluid which is applied by one single point of flagellum.

$$\mathbf{F}\delta(r) - \nabla p + \mu\nabla^2\mathbf{u} = 0 \tag{3.79}$$

In above equation force **F** is localized, which means that, it perfectly acts at one point, thus, it is multiplied by *δ(r).* One proper representation of velocity field, which is created by this Stokeslet is:

$$\mathbf{u} = \frac{\mathbf{F}}{6\pi\mu r} + \frac{1}{4}r^2\nabla\left[\nabla.\left(\frac{\mathbf{F}}{6\pi\mu r}\right)\right] \tag{3.80}$$

In Stokeslet, there is net force acting on the fluid and velocity flow field is decaying with *1/r* when *r->∞*. Then, he extends this model which has both helical propeller and body because, he mentions that the helical undulation by itself cannot satisfy the instantaneous equilibrium condition of the system since, it generates a net thrust force by itself. This extension is done for finite thrust, which includes both the cell body and the helical flagellum without considering the hydrodynamic interaction between them. Then, the analysis is done with including the long range hydrodynamic interaction between the flagellum and the cell body [21].

Effective tail length, L_{eff}, can be calculated as:

$$L_{eff} = \sqrt{(2\pi B)^2 + \lambda^2}\,\frac{L_{tail}}{\lambda} \tag{3.81}$$

where B is amplitude of the and λ is the wavelength of tail, L_{tail} is the apparent tail length. According to Lighthill's [8] article, α is the ratio of apparent tail length to actual, effective, tail length as:

$$\alpha = \frac{L_{tail}}{L_{eff}} \tag{3.82}$$

By using this ratio, ε can be calculated as:

$$\varepsilon = \frac{5.2\alpha r}{\lambda} \tag{3.83}$$

Then, to calculate the resistive force coefficients, Lighthill's $A_1(\alpha)$ and $A_2(\alpha)$ parameters are found as:

$$A_1(\alpha) = \left(\int_{\varepsilon}^{\alpha} \frac{\theta \sin\theta d\theta}{[\alpha^2\theta^2 + 2(1-\alpha^2)(1-\cos\theta)]^{\frac{3}{2}}} \right) + ln\varepsilon \tag{3.84}$$

$$A_2(\alpha) = \left(\int_{\varepsilon}^{\alpha} \frac{(sin\theta)^2 d\theta}{[\alpha^2\theta^2 + 2(1-\alpha^2)(1-\cos\theta)]^{\frac{3}{2}}} \right) + ln\varepsilon \tag{3.85}$$

where θ is between $\theta = [\varepsilon, 2\pi c]$ and c is a periodicity constant. These calculations are verified by checking the α^2 vs $A_1(\alpha)$ and $A_2(\alpha)$ graphs which is below and it reveals the same behavior with Lighthill's graphics.

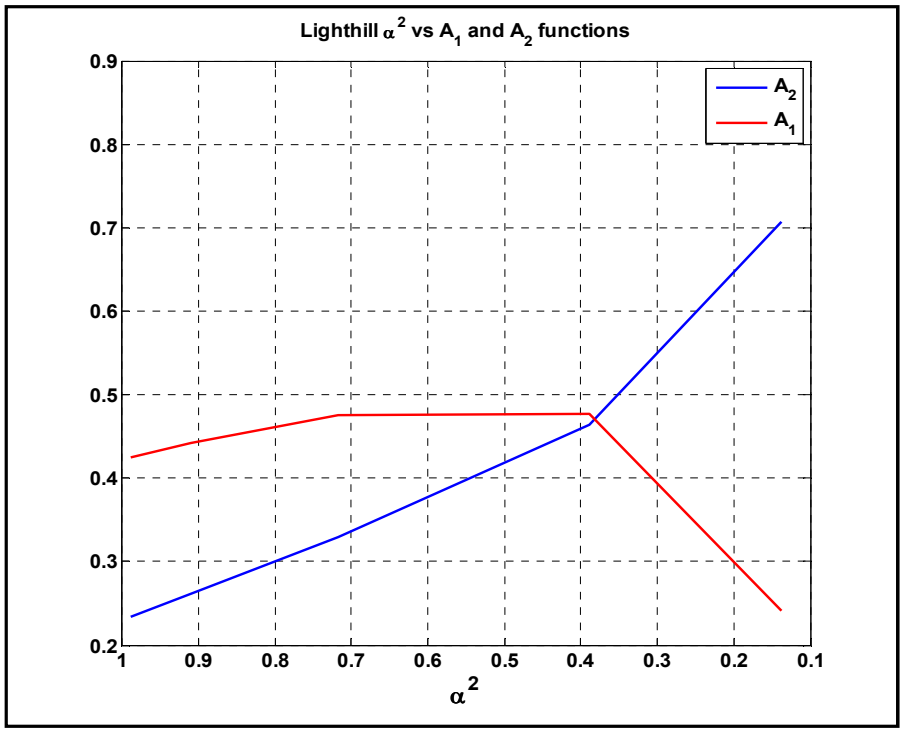

Figure 3.6: The functions $A_1(\alpha)$ and $A_2(\alpha)$

As a result, Lighthill's tangential, C_T, and normal resistive, C_N, force coefficients are calculated as:

$$C_T = \frac{2\pi\mu}{-ln\varepsilon - \frac{1}{2} + \alpha^2 A_1(\alpha) + (1-\alpha^2)A_2(\alpha)} \quad (3.86)$$

$$C_N = \frac{4\pi\mu}{-ln\varepsilon + (2\alpha^2 - 1)A_1(\alpha) + 2(1-\alpha^2)A_2(\alpha)} \quad (3.87)$$

3.3.3.2.Lauga's Resistive Force Coefficients

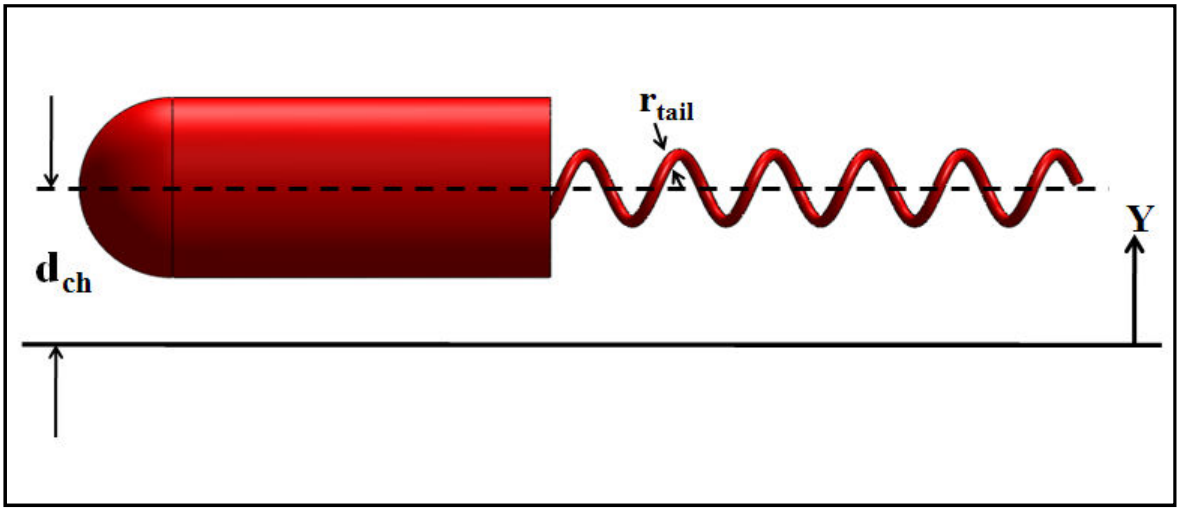

Figure 3.7: Parameters in Lauga's Resistive Force Coefficients

Lauga models the bacterium as a single, left-handed rigid helix with spherical body attached to it. As seen from the Figure 3.7, this bacteria's tail has radius r_{tail} and its center of mass location is at a distance d_{ch} above the solid surface.

In their analysis, they do not use free swimmer resistive force coefficients hence, the presence of the solid boundaries modifies them. This modification is reflected into these coefficients with adding them the wall boundary distance effect as d_{ch}.

As a result, Lauga's tangential, C_T, and normal resistive, C_N, force coefficients are calculated as:

$$C_T = \frac{2\pi\mu}{ln\left(2d_{ch}/r_{tail}\right)} \quad (3.88)$$

$$C_N = 2C_T = \frac{4\pi\mu}{ln\left(2d_{ch}/r_{tail}\right)} \tag{3.89}$$

CHAPTER 4

CFD MODELLING

The swimming robot with a rigid helical tail and a bullet shaped body is analyzed COMSOL with three simulation sets to verify the experimental results. In this chapter, the parts of COMSOL modeling are explained. First, non-dimensional modeling process is explained because all models are done with respect to this process. Then, the geometric properties of the helical propeller system are given. This is followed by the parametric approach, which shows the parameters of the different simulation sets. Then, the details of the model are shown by explaining frames, boundary conditions with subdomain settings and mesh zones. Lastly, the 2 DOF equation of motion of the swimmer are given which are used in models.

4.1 NON-DIMENSIONALIZATION OF CFD MODEL

We begin with the differential equation for conservation of linear momentum for a Newtonian fluid, known as incompressible Navier Stokes equation. The dimensional form of Navier Stokes equation is:

$$\rho \frac{D\boldsymbol{V}}{Dt} = \rho \left[\frac{\partial \boldsymbol{V}}{\partial t} + (\boldsymbol{V}.\boldsymbol{\nabla})\boldsymbol{V}\right] = -\boldsymbol{\nabla}\mathrm{P} + \mu\nabla^2\mathbf{V} \tag{4.1}$$

From this equation the dimensional x-momentum equation can be written as:

$$\rho\left(\frac{\partial u}{\partial t} + u\frac{\partial u}{\partial x} + v\frac{\partial u}{\partial y} + w\frac{\partial u}{\partial z}\right) = -\frac{\partial p}{\partial x} + \mu\left(\frac{\partial^2 u}{\partial x^2} + \frac{\partial^2 u}{\partial y^2} + \frac{\partial^2 u}{\partial z^2}\right) \tag{4.2}$$

To obtain the non-dimensional form of this equation scaling parameters are chosen as characteristic length, l; characteristic speed, V; characteristic frequency, f and reference pressure, p_0. Thus, non-dimensional parameters u^*, v^*, p^*, x^*, y^* and t^* can be expressed as:

$$u^* = \frac{u}{V} \tag{4.3}$$

$$v^* = \frac{v}{V} \tag{4.4}$$

$$p^* = \frac{p}{\rho U^2} \tag{4.5}$$

$$x^* = \frac{x}{l} \tag{4.6}$$

$$y^* = \frac{y}{l} \tag{4.7}$$

$$t^* = \frac{t}{\tau} = tf \tag{4.8}$$

Various transformations can be made:

$$\frac{\partial u}{\partial x} = \frac{\partial (u^* V)}{\partial x^*} \frac{\partial x^*}{\partial x} = \frac{\partial (u^* V)}{\partial x^*} \frac{\partial (x/l)}{\partial x} \tag{4.9}$$

Thus it can be expressed as:

$$\frac{\partial u}{\partial x} = \frac{V}{l} \frac{\partial u^*}{\partial x^*} \tag{4.10}$$

In same way $\partial u/\partial y$ and $\partial u/\partial z$ can be expressed as:

$$\frac{\partial u}{\partial y} = \frac{V}{l} \frac{\partial u^*}{\partial y^*} \tag{4.11}$$

$$\frac{\partial u}{\partial z} = \frac{V}{l} \frac{\partial u^*}{\partial z^*} \tag{4.12}$$

and $\partial^2 u/\partial x^2$ can be found in non dimensionalized form as:

$$\frac{\partial^2 u}{\partial x^2} = \frac{V}{l} \frac{\partial}{\partial x^*} \left(\frac{\partial u^*}{\partial x^*}\right) \frac{\partial x^*}{\partial x} = \frac{V}{l} \frac{\partial}{\partial x^*} \left(\frac{\partial u^*}{\partial x^*}\right) \frac{\partial \left(\frac{x}{l}\right)}{\partial x} \tag{4.13}$$

$$\frac{\partial^2 u}{\partial x^2} = \frac{V}{l^2} \frac{\partial^2 u^*}{\partial x^{*2}} \tag{4.14}$$

In same way $\partial^2 u/\partial y^2$ and $\partial^2 u/\partial z^2$ can be expressed as:

$$\frac{\partial^2 u}{\partial y^2} = \frac{V}{l^2} \frac{\partial^2 u^*}{\partial y^{*2}} \tag{4.15}$$

$$\frac{\partial^2 u}{\partial z^2} = \frac{V}{l^2} \frac{\partial^2 u^*}{\partial z^{*2}} \tag{4.16}$$

The other term $\partial u/\partial t$ can be expressed as in non dimensionalized term as:

$$\frac{\partial u}{\partial t} = \frac{V}{\tau} \frac{\partial u^*}{\partial t^*} \tag{4.17}$$

and for pressure terms:

$$\frac{\partial p}{\partial x} = \frac{\partial (p_0 p^*)}{\partial x^*} \frac{\partial x^*}{\partial x} = \frac{\partial (p_0 p^*)}{\partial x^*} \frac{\partial \left(\frac{x}{l}\right)}{\partial x} \tag{4.18}$$

$$\frac{\partial p}{\partial x} = \frac{p_0}{l} \frac{\partial p^*}{\partial x^*} \tag{4.19}$$

By substituting these terms into x momentum Navier Stokes equation becomes:

$$\rho\left(\frac{V}{\tau}\frac{\partial u^*}{\partial t^*}+u\frac{V}{l}\frac{\partial u^*}{\partial x^*}+v\frac{V}{l}\frac{\partial u^*}{\partial y^*}+w\frac{V}{l}\frac{\partial u^*}{\partial z^*}\right)=\frac{-p_0}{l}\frac{\partial p^*}{\partial y^*}+\mu\frac{V}{l^2}\left(\frac{\partial^2 u^*}{\partial {x^*}^2}+\frac{\partial^2 u^*}{\partial {y^*}^2}+\frac{\partial^2 u^*}{\partial {z^*}^2}\right) \quad (4.20)$$

Dividing all terms with $\rho V^2/l$ this equation becomes:

$$\frac{fl}{V}\frac{\partial u^*}{\partial t^*}+\frac{u}{V}\frac{\partial u^*}{\partial x^*}+\frac{v}{V}\frac{\partial u^*}{\partial y^*}+\frac{w}{V}\frac{\partial u^*}{\partial z^*}=-\frac{1}{2}\frac{\partial p^*}{\partial x^*}+\frac{\mu}{\rho Vl}\left(\frac{\partial^2 u^*}{\partial {x^*}^2}+\frac{\partial^2 u^*}{\partial {y^*}^2}+\frac{\partial^2 u^*}{\partial {z^*}^2}\right) \quad (4.21)$$

Thus, Navier Stokes in non-dimensional form can be written as:

$$[St]\frac{\partial \boldsymbol{V}^*}{\partial t^*}+(\boldsymbol{V}^*.\nabla^*)\boldsymbol{V}^*=-\frac{1}{2}\nabla^*\boldsymbol{P}^*+\left[\frac{1}{Re}\right]\nabla^{*\mathbf{2}}\boldsymbol{V}^* \quad (4.22)$$

For expressing helical propeller system in non-dimensional form, as reference parameters scaling factor (*D*) and frequency (*f*) are used. The first step to represent the prototype in COMSOL is determining the scaling factor (*D*) which is 10^{-2} in model. Frequency also is given as input to the model which is measured from experiments. By using scaling factors *D* and *f,* non-dimensional thrust force F_x* and torque T_x* can be found as:

Table 4.1: Non-dimensionalization process for thrust force F_x^*

Variable	[ ]	Variable	[ ]	Variable	[ ]	Variable	[ ]
F_x	$\frac{ML}{T^2}$	$\frac{F_x}{D}$	$\frac{M}{T^2}$	$\frac{F_x}{\rho D^4}$	$\frac{1}{T^2}$	$\frac{F_x}{f^2\rho D^4}$	0
f	$\frac{1}{T}$	f	$\frac{1}{T}$	f	$\frac{1}{T}$		
ρ	$\frac{M}{L^3}$	ρD^3	M				
μ	$\frac{M}{LT}$	μD	$\frac{M}{T}$	$\frac{\mu}{\rho D^2}$	$\frac{1}{T}$	$\frac{\mu}{f\rho D^2}$	0
D	L						

Table 4.2: Nondimensionalization process for thrust torque T_x^*

Variable	[ ]	Variable	[ ]	Variable	[ ]	Variable	[ ]
T_x	$\frac{ML^2}{T^2}$	$\frac{T_x}{D^2}$	$\frac{M}{T^2}$	$\frac{T_x}{\rho D^5}$	$\frac{1}{T^2}$	$\frac{T_x}{f^2\rho D^5}$	0
f	$\frac{1}{T}$	f	$\frac{1}{T}$	f	$\frac{1}{T}$		
ρ	$\frac{M}{L^3}$	ρD^3	M				
μ	$\frac{M}{LT}$	μD	$\frac{M}{T}$	$\frac{\mu}{\rho D^2}$	$\frac{1}{T}$	$\frac{\mu}{f\rho D^2}$	0
D	L						

With same process, the non-dimensional velocity can be found as:

$$V_x^* = fD \tag{4.23}$$

The CFD model sets are non-dimensional models, thus non-dimensional Navier Stokes equation is considered as:

$$[St]\frac{\partial \boldsymbol{V}^*}{\partial t^*} + (\boldsymbol{V}^*.\nabla^*)\boldsymbol{V}^* = -\nabla^*\boldsymbol{P}^* + \left[\frac{1}{Fr^2}\right]\boldsymbol{g} + \left[\frac{1}{Re}\right]\nabla^{*\mathbf{2}}\boldsymbol{V}^* \tag{4.24}$$

From this equation, it can be observed that for dynamic viscosity term, in non-dimensional model, 1/Re must be used. Both dimensional and non-dimensional parameters can be seen from Table 4.7 for CFD and prototype, respectively:

Table 4.3: Dimensional (Prototype) and Nondimensional (CFD) Parameters

	$\boldsymbol{\rho}$	$\boldsymbol{D_{ch1}}$	$\boldsymbol{D_{ch2}}$	$\boldsymbol{f}$	$\boldsymbol{\mu}$
CFD	1 [1]	3.6 [1]	2.4 [1]	1 [1]	$1/Re$
Prototype	900 $[kg/m^3]$	0.036 $[m]$	0.024 $[m]$	f_{exp}	5.6 $[Pa*s]$

Because of CFD model is scaled version of the prototype, to achieve the similarity between the model and the prototype, Reynolds number must be the same as:

$$Re_{CFD} = Re_{Pro} \tag{4.25}$$

$$\frac{\rho_{CFD}\, V_{CFD}\, D_{CFD}}{\frac{1}{Re_{CFD}}} = \frac{\rho_{Pro}\, V_{Pro}\, D_{Pro}}{\mu_{Pro}} \tag{4.26}$$

In above equation, subscript *CFD* is used for COMSOL model and subscript *Pro* is used for prototype. As it is mentioned before, the scaling parameters are chosen as characteristic length *D* and frequency *f*, thus velocity can be expressed as $V = Df$. Also from Table 4.7 it can

be seen that, characteristic length D is 10^{-2}, thus $D_{Pro} = D_{CFD}10^{-2}$. As a result of these expressions, Reynolds number equality between the model and prototype can be expressed as:

$$\frac{\rho_{CFD}\ D_{CFD}\, f_{CFD}\, D_{CFD}}{\frac{1}{Re_{CFD}}} = \frac{\rho_{Pro}\, D_{CFD}10^{-2}\, f_{Pro} D_{CFD}10^{-2}}{\mu_{Pro}} \tag{4.27}$$

Thus, dynamic viscosity of subdomain setting can be specified as:

$$\frac{1}{Re_{CFD}} = \frac{\mu_{Pro}}{\rho_{Pro}10^{-4} f_{Pro}} \tag{4.28}$$

4.2. GEOMETRIC PROPERTIES

With non-dimensional approach which was explained in section 4.1, characteristic length parameter is chosen as 10^{-2} and one type of swimmer which has the same geometrical properties in experiments is modeled in COMSOL simulations. This swimmer's motion is analyzed within two cylindrical channels which also has same geometrical parameters with respect to experiments.

The swimmer has bullet shaped body with helical propeller and its geometrical values are given in Table 4.4. In addition to that, the cylindrical channels have diameters 3.6 cm and 2.4 cm which are in non-dimensional form as in Table 4.5.

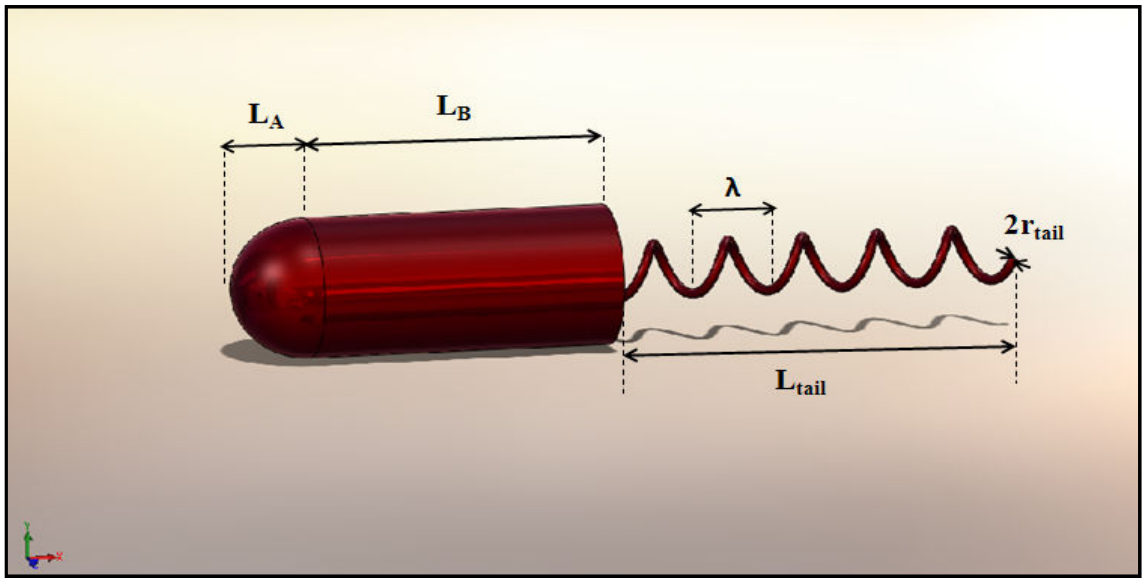

Figure 4.1: Swimmer with parametric dimensions

Table 4.4: Common Dimensional Properties for Swimmer

Radius of head, L_A	0.79 [1]
Length of body, L_B	3.21 [1]
Apparent length of tail, L_{tail}	4.8 [1]
Diameter of tail, $2r_{tail}$	0.1 [1]

Table 4.5: Dimensional Properties for Cylindrical Channels

Channels	Channel 1	Channel 2
Diameter ($2R_{ch}$)	3.6 [1]	2.4 [1]
Length of channel (L_{ch})	50 [1]	50 [1]

4.3. PARAMETRIC APPROACH

Helical propeller system with bullet shaped body is analyzed in COMSOL with three simulation sets. One of the sets is representing *center* motion of this propeller system in Channel 1 with R_{ch} 1.8 [1], the other one is representing the *off-center* motion of this system in Channel 1 with R_{ch} 1.8 [1] which is much more similar motion trend with respect to experiments. These two different sets are significant due to understanding of wall distance effect to this helical propeller system in same channel. The last set of simulation is representing *center* motion of this system in narrower channel with 1.2 [1] diameter, where it is needed to understand how the dynamical values are changing with respect to changing channel limits.

In these sets, input parameters are the frequency, which is measured from the experiments, f; apparent length of the tail, L_{tail}; wavelength, λ; maximum amplitude of the helical tail B; deformation limits of helical tail which will be explained in detail in Section 4.5, $xtail_1$, $xtail_2$, $xtail_{box}$, R_{swx}; deformation limit of whole helical propeller system in longitudinal axis, swx_1 and swx_2; channel dimensions of R_{ch} and L_{ch}.

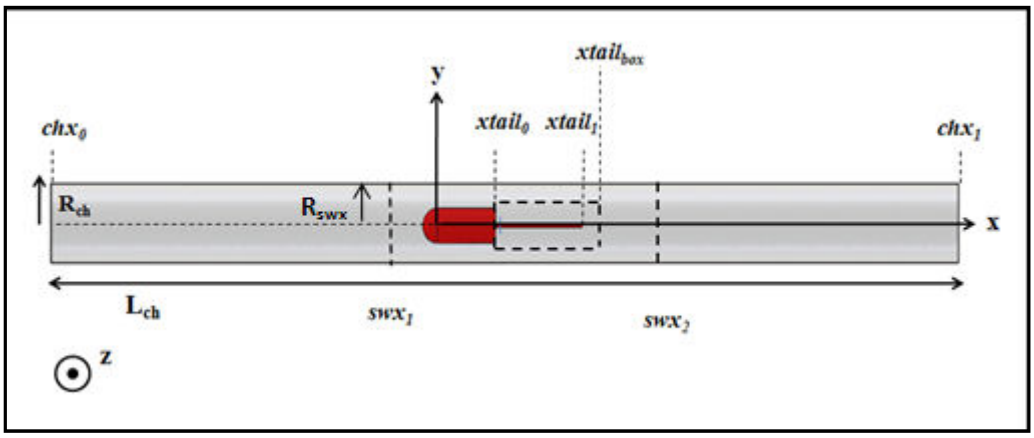

Figure 4.2: Side view of micro channel and swimmer with parametric dimensions

Table 4.6: Input parameters for *Channel 1* simulations

Robots	f [1]	B [1]	λ [1]
A_1	6.9	0.1	4.8
A_2	8.193	0.1	2.4
A_3	4.322	0.1	1.6
A_4	4.325	0.1	1.2
A_6	6.133	0.1	0.8
B_1	3.9	0.2	4.8
B_2	3.805	0.2	2.4
B_3	3.27133	0.2	1.6
B_4	3.144	0.2	1.2
B_6	2.843	0.2	0.8
C_1	3.1	0.3	4.8
C_2	2.01	0.3	2.4
C_3	2.49433	0.3	1.6
C_4	2.137	0.3	1.2
D_1	2	0.4	4.8
D_2	1.6	0.4	2.4
D_3	1.1833	0.4	1.6

Channel 1 center simulations are done for robots A_1, A_2, A_3, A_4, A_6, B_1, B_2, B_3, B_4, C_1, C_2, C_3, D_1, D_2 and D_3. In addition to that *Channel 1 off-center* simulations are done for robots A_2, A_3, A_4, A_6, B_2, B_3, B_4, B_6, C_1, C_2 and C_3.

Table 4.7: Input parameters for *Channel 2* simulations

Robots	f	B	Λ
$\boldsymbol{B_3^*}$	3.611	0.2	1.6
$\boldsymbol{B_4^*}$	3.7833	0.2	1.2
$\boldsymbol{C_3^*}$	2.8167	0.3	1.6
$\boldsymbol{C_4^*}$	2.42	0.3	1.2
$\boldsymbol{D_3^*}$	1.0389	0.4	1.6

Channel 2 center simulations are done for robots B_3*, B_4*, C_3*, C_4* and D_3*.

4.4. FRAMES

In COMSOL simulations, two frames are defined on system as reference and spatial frames. Spatial frame is a fixed coordinate system with spatial coordinates (x, y, and z) which is associated with deformed mesh application mode. In this coordinate system, the mesh is deforming and the coordinates (x, y, and z) of mesh nodes are functions of time. Furthermore, reference frame (X, Y, and Z) is the coordinate system which describes the original configuration. In other words, this frame is associated with the geometry, and it exits even when the deformed mesh is not defined.

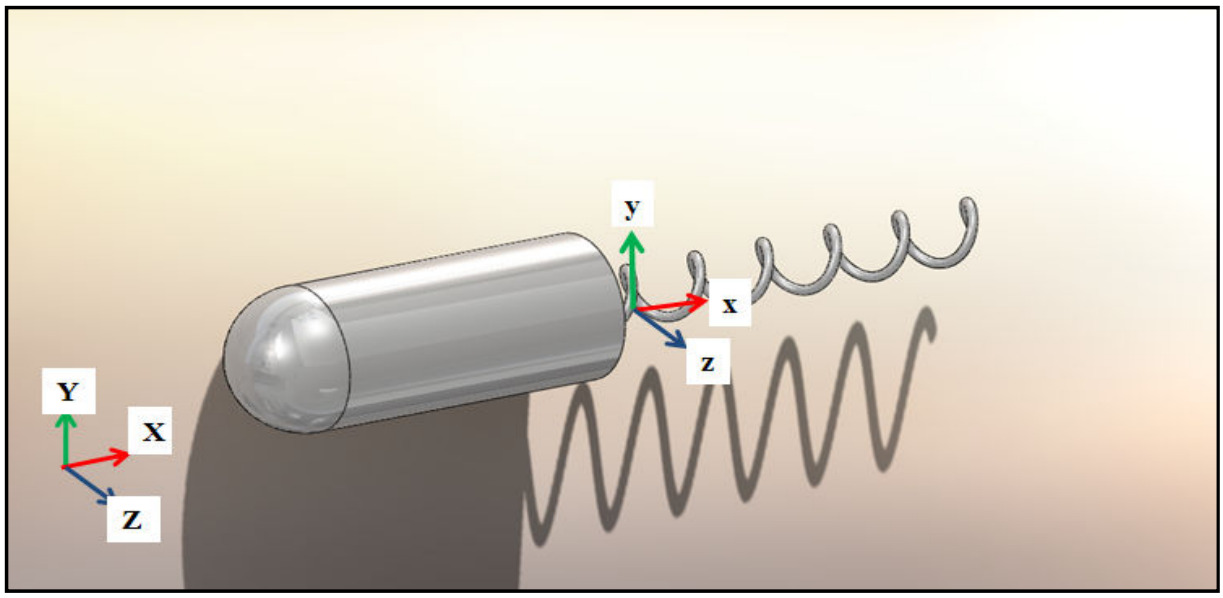

Figure 4.3: Spatial and Reference Frames

4.5. BOUNDARY CONDITIONS

In order to solve Navier Stokes equation and continuity equations, appropriate initial conditions and boundary conditions need to be applied. The boundary conditions on inlet-outlet, radial walls, body and tail are specified as follows: Pressure boundary conditions need static gage pressure inputs [1]. For this CFD model, cylindrical channel inlet pressure is specified as zero. This zero gage pressure boundary conditions can be interpreted as at the inlet and outlet, pressures are equal to the environmental pressure where the channel is settled in.

$$[-P\mathbf{I}].\mathbf{n}|_{x=0,y,z,t} = [-P\mathbf{I}].\mathbf{n}|_{x=L_{ch},y,z,t} = 0 \tag{4.29}$$

where $\mathbf{n}$ is the normal direction at outlet and inlet boundaries.

In this CFD model, which is the viscous flow application, radial walls have no-slip boundary conditions. This boundary condition means that, while tangential fluid velocity equal to wall velocity, normal velocity component is set to be zero [1]. In addition to that, translational and rotational velocities are assigned as wall boundary conditions at body and tail of helical propeller system. Details of these are explained in Section 4.7.

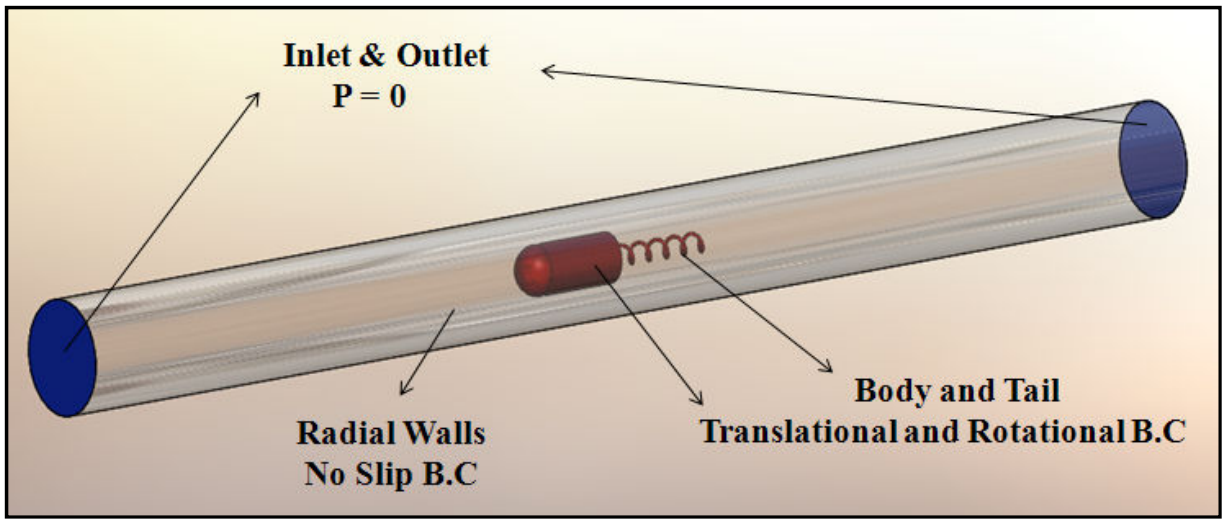

Figure 4.4: Boundary Conditions on Inlet-Outlet, Radial Walls, Body and Tail

4.6.NUMERICAL METHODS

4.6.1. Implementation of the Mesh Deformation

CFD algorithms use two different approaches to solve problems as Lagrangian-mesh method and Eulerian-mesh method. In Lagrangian-mesh method, small deformations for fluidic problems or solid problems with small displacement can be modeled [45] In Eulerian method, any flow can be modeled except the flow with moving boundaries or free surface [45]. On the other side, both approach have some disadvantages as in Lagrangian method, the problems with large distortion of the computational domain cannot be solved without frequent re-meshing operations and as in Eulerian one, material interfaces can lose their definitions when the fluid boundaries are moving through the mesh and for local regions mesh with fine resolution is a hard task to achieve [45]. Therefore, a new approach, which is the combination of these two, is needed to solve the problems which cannot be modeled with the approaches neither Lagrangian nor Eulerian methods are used separately. This method is Arbitrary-Lagrangian-Eulerian method where can be used to reduce the mesh distortion in order to prevent the frequent re-meshing operation. Braescu et al. give a description that, if the velocity of the domain is ω, in Eulerian approach this ω is zero while in Lagrangian approach

it is equal to the velocity of the particle. But in ALE approach, it is neither zero nor the velocity of the fluid particle that, it has the value between these where the velocity is adjusted by this approach to control the mesh displacement and prevent the distortion [45].

In three sets of CFD simulations, two mesh zones are defined that, first is prescribed along YZ axes which provides the deformation of cylindrical tail into helical tail and second is prescribed along XY axes which provides the displacement of swimmer.

The first mesh zone, which is prescribed along XY axes, is regulating the movement of swimmer in –X axis which is induced by the rotation about Y and Z axes. Along X axis, swimmer displacement limits, which are between swx_1 and swx_2, takes unit value, but out of these limits because the mesh cannot pass throughout the inlet and outlet boundaries, it makes linear movement which takes zero value at channel boundaries as chx_0 and chx_1. In other words, this mesh behavior is like the accordion movement that squeezing the mesh nodes along –X direction where the swimmer moves along forward direction, and broadening the mesh nodes along +X direction where it represents the area of backside of the swimmer. This behavior is represented by trapezoid geometry.

To find the environmental mesh deformation along X axis, first, the mesh movement equation must be specified as:

$$sw_{env} = (X \leq swx_2)(X \geq swx_1) + (X < swx_1)(X \geq chx_0)\left(\frac{X - chx_0}{swx_1 - chx_0}\right) + (X > swx_2)(X \leq chx_1)\left(\frac{X - chx_1}{swx_2 - chx_1}\right) \quad (4.30)$$

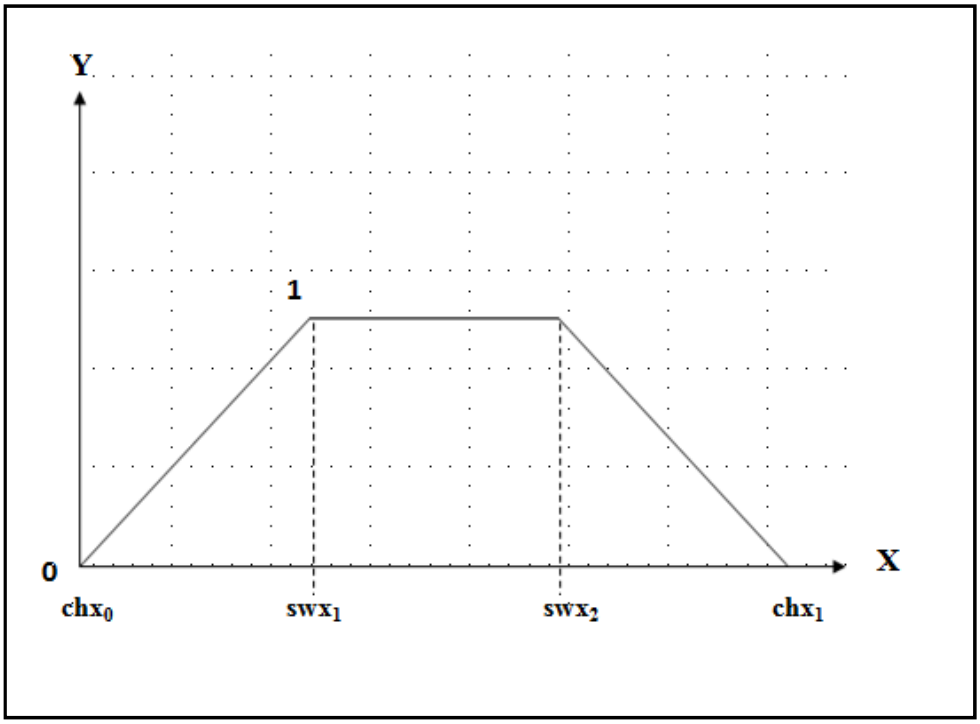

Figure 4.4: *X* axis Mesh Diagram for *Channel 1* and *Channel 2*

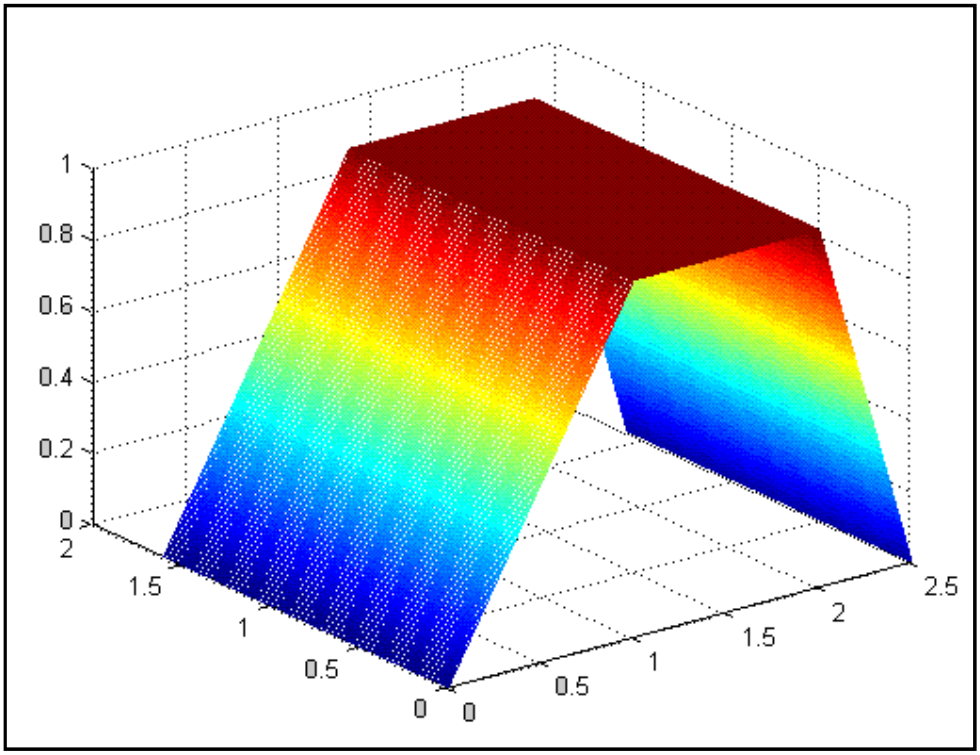

Figure 4.5: 3D mesh configuration in *XY* axes

The second mesh zone, which is prescribed along *YZ* axes, is regulating the shape of tail which is induced by the rotation about *Y* and *Z* axes. For *center* movement of swimmer in *Channel 1* and *Channel 2*, along YZ axes, the tail deformation is limited with channel radial boundaries as $-R_{ch}$ and R_{ch}; for *off-center* movement of swimmer in *Channel 1*, along YZ axes, this deformation is limited by $-R_{ch}$* and R_{ch}' . The mesh displacement is allowed along these radial limits because the mesh cannot pass throughout the radial boundaries of channels. Due to this constraint, in *off-center* movement, these radial boundaries of mesh are limited by values which are less than channel boundaries limits. Furthermore, through radial boundaries to r_{tail} values, mesh makes linear movement which takes zero value at radial boundaries of dummy channels and takes unity value at r_{tail} boundaries. Along $-r_{tail}$ and r_{tail} boundaries, it takes unity value and between these boundaries, the function describes the circle to prescribe tail shape.

Thus, for calculating the tail deformation in YZ domain:

$$tail_{env,YZ} = \left(\frac{Y^2+Z^2-R_{ch}^2}{r_{tail}^2-R_{ch}^2}\right)\left((Y^2+Z^2) \le R_{ch}^2\right)\left((Y^2+Z^2) > r_{tail}^2\right) + \left(Y^2+Z^2 \le r_{tail}^2\right) \quad (4.31)$$

To find tail environment in XYZ domain this $tail_{env,YZ}$ should be multiplied with:

$$tail_{env,XYZ} = tail_{env,YZ}\left[(X \geq xtail_0)(X < xtail_1) + (X > xtail_1)(X < xtail_{box})\frac{(xtail_{box}-X)}{(xtail_{box}-xtail_1)}\right] \quad (4.32)$$

Deformation of tail along Y and Z axes are given as:

$$y_{deformation} = q(s,t) = B_q(s)\cos(\omega t - ks) \quad (4.33)$$

$$z_{deformation} = r(s,t) = B_r(s)\sin(\omega t - ks) \quad (4.34)$$

where $B_q(s)$ and $B_r(s)$ are the functions:

$$B_q(s) = B_q^{max}(1 - e^{-cs}) \quad (4.35)$$

$$B_r(s) = B_r^{max}(1 - e^{-cs}) \quad (4.36)$$

As a result, the subdomain setting for helical tail shape is given as:

$$tail_{y_{def}} = tail_{env,XYZ}\, y_{deformation} \quad (4.37)$$

$$tail_{z_{def}} = tail_{env,XYZ}\, z_{deformation} \quad (4.38)$$

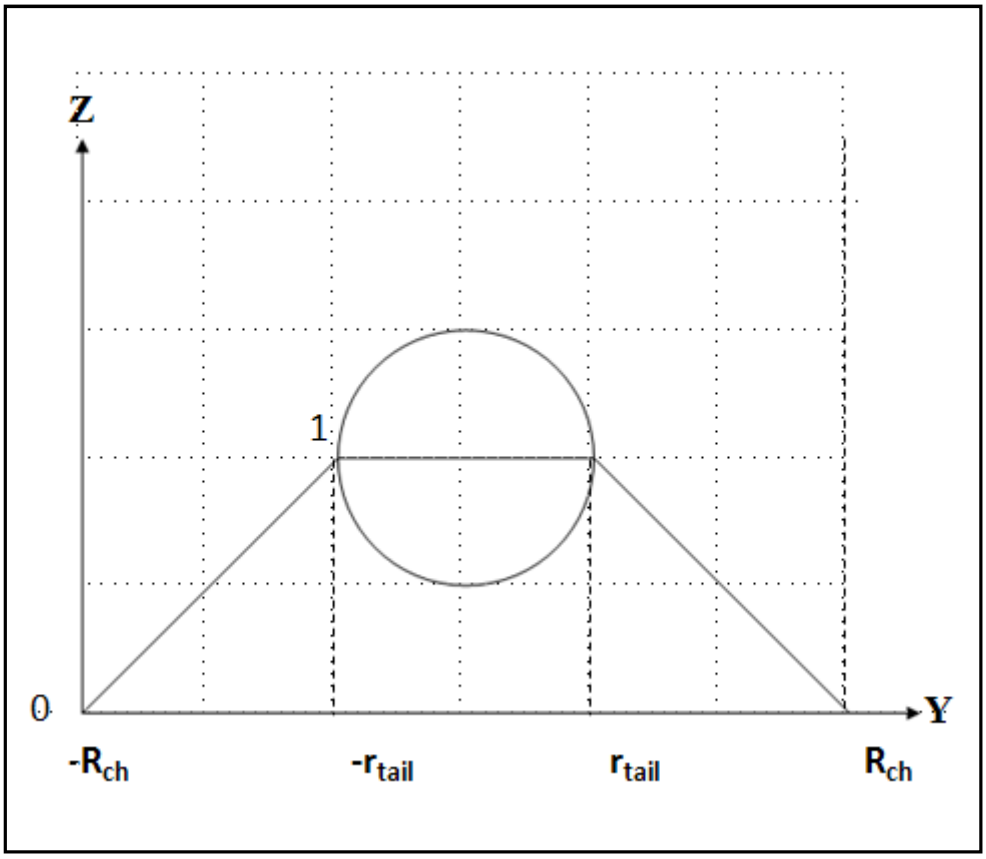

Figure 4.6: *Center* Movement YZ axis Mesh Diagram for *Channel 1* and *Channel 2*

Table 4.8: *Center* Movement Non-dimensional Parameters on Figure 4.6

$\underline{\boldsymbol{Center}}$	$\boldsymbol{Channel\ 1}$	$\boldsymbol{Channel\ 2}$
$\boldsymbol{R_{ch}}$	1.8 [1]	1.2 [1]
$\boldsymbol{r_{tail}}$	0.05 [1]	0.05 [1]

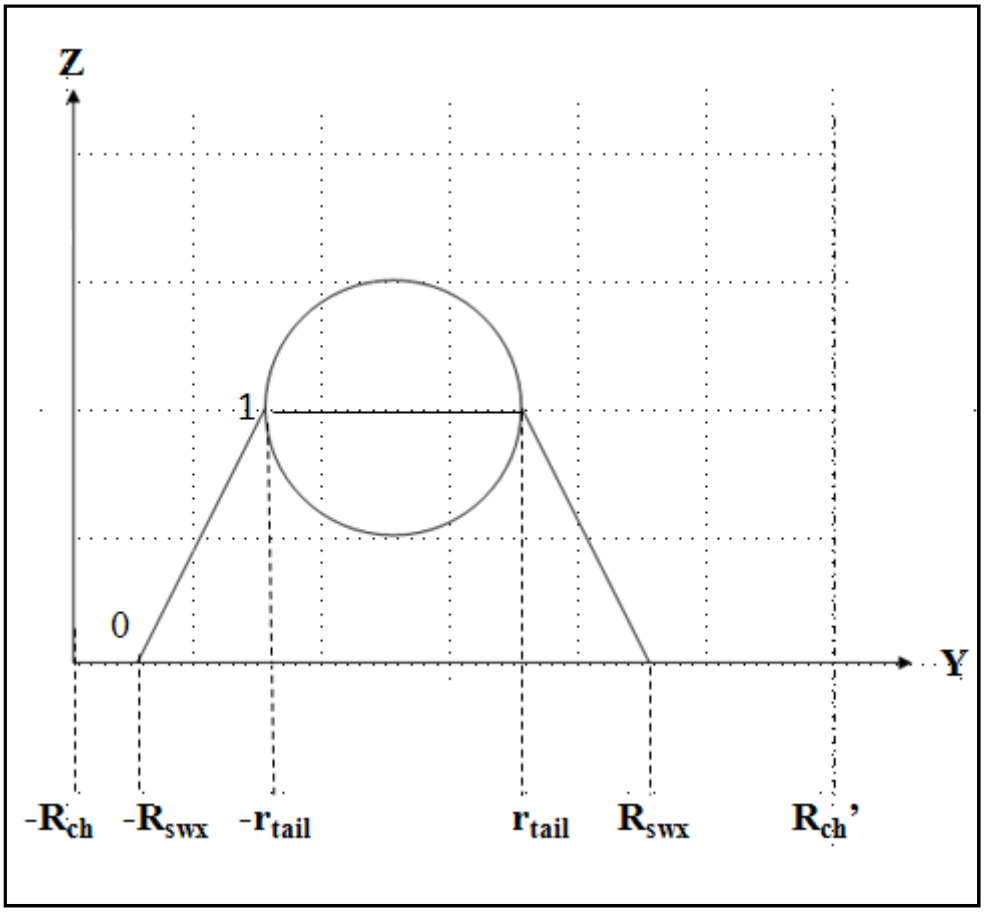

Figure 4.7: *Off-Center* Movement YZ axis Mesh Diagram for *Channel 1*

Table 4.9: *Off-Center* Movement Non-dimensional Parameters on Figure 4.7

$\underline{\boldsymbol{Off-Center}}$	$\boldsymbol{Channel\ 1}$
$\boldsymbol{-R^{*}_{ch}}$	-1.4 [1]
$\boldsymbol{R'_{ch}}$	2.2 [1]
$\boldsymbol{r_{tail}}$	0.05 [1]
$\boldsymbol{R_{swx}}$	0.9 [1]

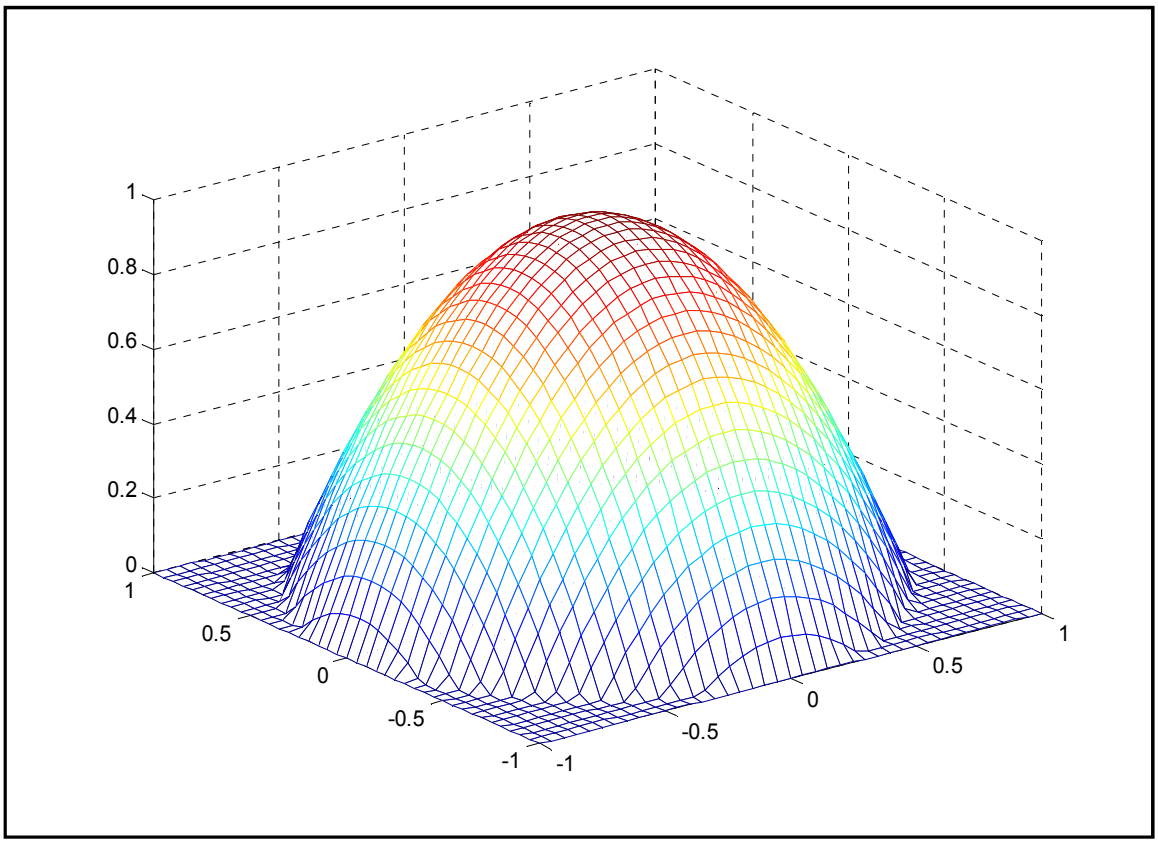

Figure 4.8: 3D mesh configuration in *YZ* axes

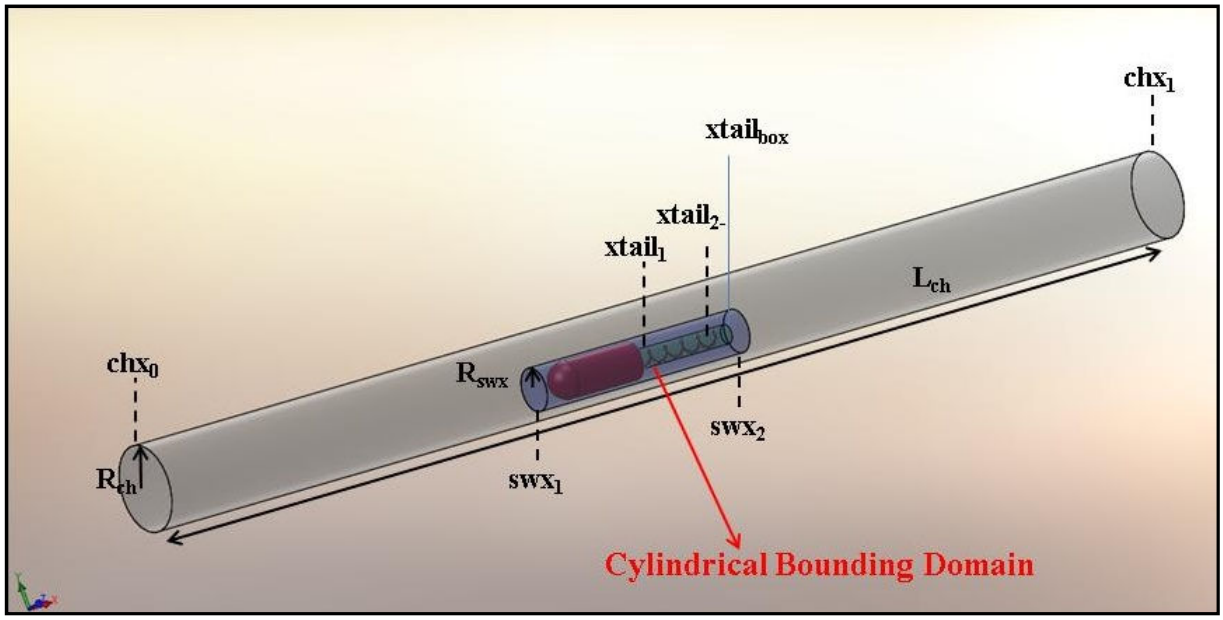

Figure 4.9: Trimetric view of channel *off-center* simulation and swimmer with parametric dimensions

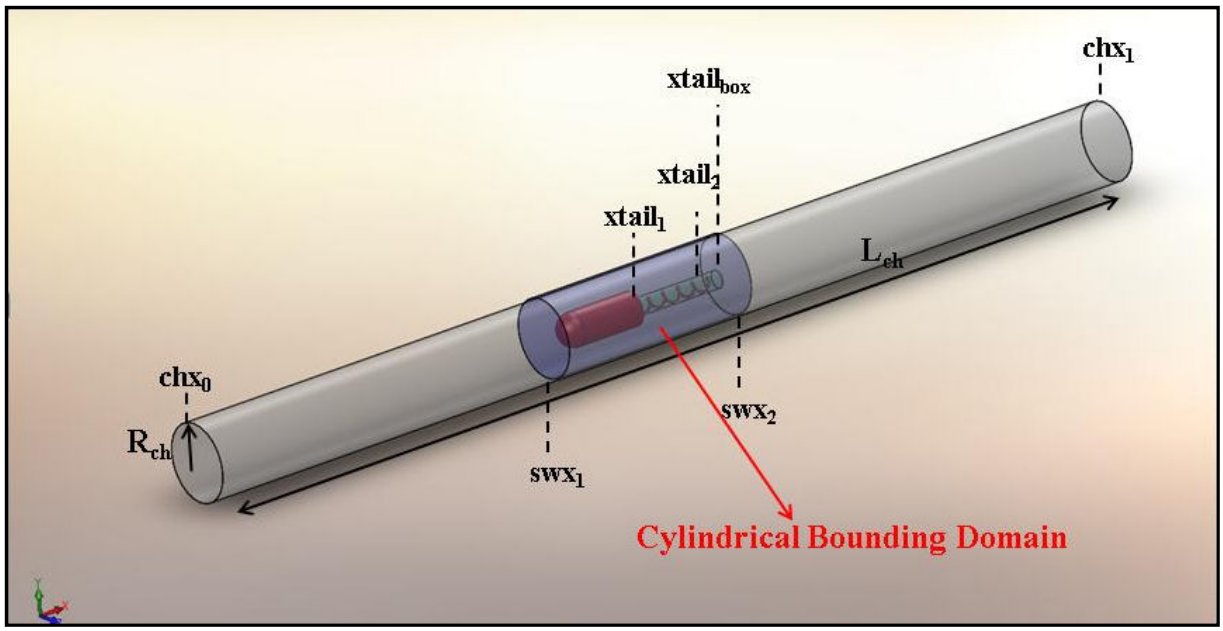

Figure 4.10: Trimetric view of micro channel *center* simulation and swimmer with parametric dimensions

4.6.2.Mesh Configuration

There are three sets of simulations that two of them done for *Channel 1* with 3.6 cm diameter and the third one are done for *Channel 2* with 2.4 cm diameter. Although, helical propeller with different parameters in different channels is modeled, for all simulations, tetrahedrons which are quadratic Lagrangian elements are used.

Figure (4.11) represents the helical propeller with bullet shaped body that, for healthy solutions some mesh strategies are developed. For body part, six mesh points are used for the bottom and top part of the circular part (II) while for the rectangular part's edges (I), this number increase to twelve to get a well distributed mesh on the body. For tail, the cylindrical part's edges (IV) are meshed with respect to number of waves. For one wave, twenty mesh points are used. Also, for the bottom and top surfaces (III) of the cylindrical part, six mesh points are needed. Furthermore, the Figure (4.12) represents the subdomain where the fine mesh is used. Mesh statistics can be found in Appendix C.

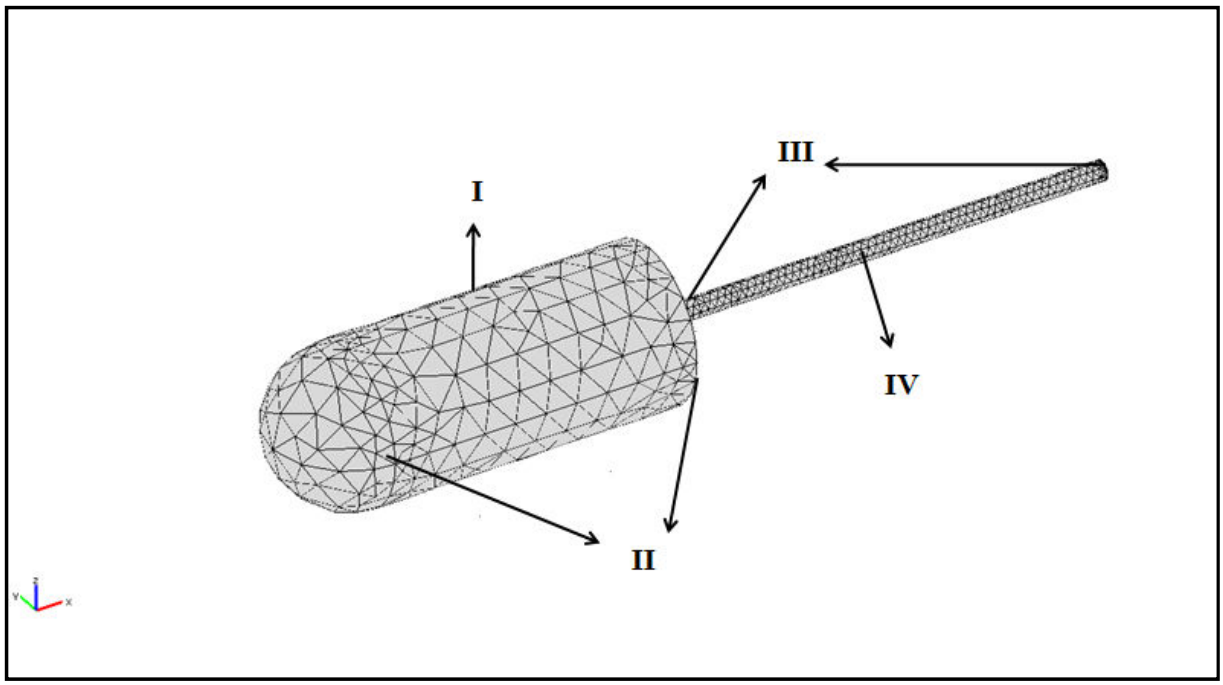

Figure 4.11: Mesh elements on swimmer

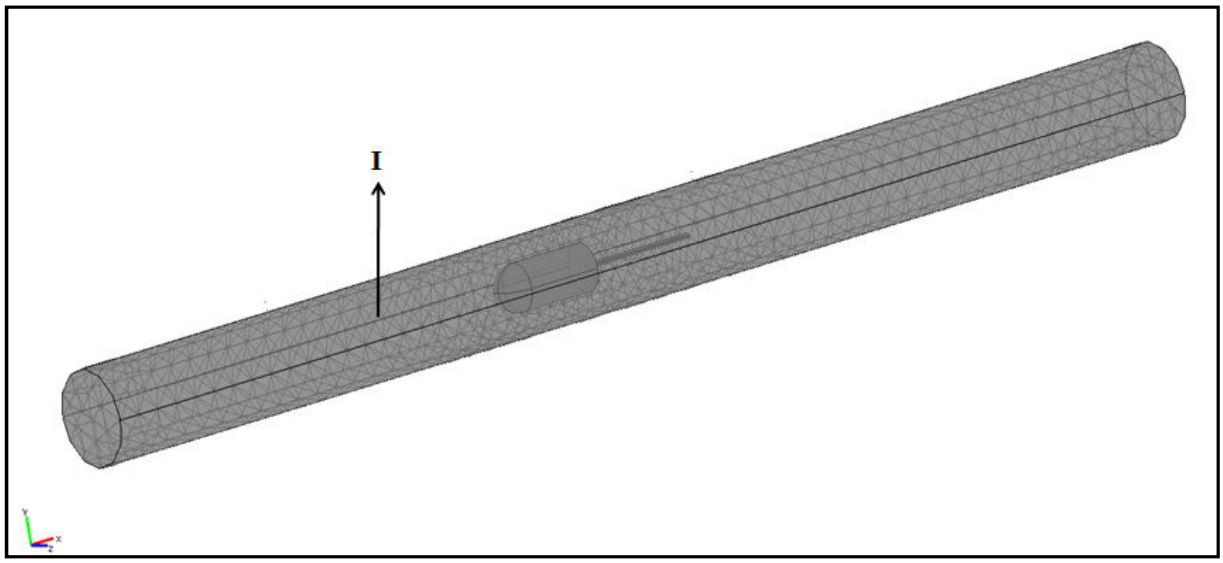

Figure 4.12: Sub-domain mesh elements

4.7.TRANSLATIONAL AND ROTATIONAL MOTION OF HELICAL PROPELLER (2 DOF MOTION)

The swimmer is assumed to be neutrally buoyant, thus, has the same density with the water in calculations. Time dependent position and orientation of swimmer with 2 DOF can be calculated with ordinary differential equations (ODE) and the equation of motion is given as:

$$\mathbf{x}(t) = [x(t) \;\; y(t) \;\; z(t)]' \tag{4.39}$$

$$\dot{\mathbf{x}}(t) = V(t) = [u_x(t) \;\; 0 \;\; 0]' \tag{4.40}$$

$$\boldsymbol{\theta}(t) = [\theta_x(t) \;\; 0 \;\; 0]' \tag{4.41}$$

$$\dot{\boldsymbol{\theta}}(t) = \omega(t) = [\theta_x(t) \;\; 0 \;\; 0]' \tag{4.42}$$

Force and torque on swimmer can be calculated by integrating the fluid forces on swimmer's surface. Furthermore, because of conservation of linear and angular momentum, both total force and torque on swimmer's surface is zero, thus, the linearity feature of these vectors with resistive coefficients, linear and angular accelerations can be calculated as [47]:

$$\begin{bmatrix} V(t) \\ \omega(t) \end{bmatrix} = \begin{bmatrix} \int -\mathbf{F}\mathrm{d}t \\ \int -\mathbf{T}\mathrm{d}t \end{bmatrix} \tag{4.43}$$

where these **F** and **T** vectors are for 2 DOF helical propeller motion [47]:

$$\mathbf{F} = [F_x \;\; 0 \;\; 0]' = [\int \Sigma_x dA \;\; 0 \;\; 0] \tag{4.44}$$

$$\mathbf{T} = [T_x \;\; 0 \;\; 0]' = \begin{bmatrix} \int [\Sigma_z y - \Sigma_y z] dA \\ 0 \\ 0 \end{bmatrix} \tag{4.45}$$

Stress tensors for 3D domain can be calculated as:

$$\Sigma_x = \left(2\mu \frac{\partial u}{\partial x} - P\right) n_x + \mu \left(\frac{\partial v}{\partial x} + \frac{\partial u}{\partial y}\right) n_y + \mu \left(\frac{\partial w}{\partial x} + \frac{\partial u}{\partial z}\right) n_z \tag{4.46}$$

$$\Sigma_y = \mu \left(\frac{\partial u}{\partial y} + \frac{\partial v}{\partial x}\right) n_x + \left(2\mu \frac{\partial v}{\partial y} - P\right) n_y + \mu \left(\frac{\partial v}{\partial z} + \frac{\partial w}{\partial y}\right) n_z \tag{4.47}$$

$$\Sigma_z = \mu \left(\frac{\partial u}{\partial z} + \frac{\partial w}{\partial x}\right) n_x + \mu \left(\frac{\partial v}{\partial z} + \frac{\partial w}{\partial y}\right) n_y + \left(2\mu \frac{\partial w}{\partial z} - P\right) n_z \tag{4.48}$$

The time dependent, 3D and incompressible flow in channel is governed by unsteady Navier-Stokes equation in deforming domain [46-47]:

$$\rho \left(\frac{\partial \mathbf{U}}{\partial t} + (\mathbf{U} - \mathbf{u}_m).\nabla \mathbf{U}\right) = -\nabla P + \mu \nabla^2 \mathbf{U} \text{ in } \Omega(\mathrm{t}) \tag{4.49}$$

In above equation, **U** is the velocity field of the flow, P is the pressure, ρ is the density and μ is the dynamic viscosity of the fluid, and $\mathbf{u}_m$ is the velocity of the deforming domain with respect to initial domain [47]:

$$\mathbf{u}_m\left(x_{\Omega(t)}, t\right) = \frac{dx_{\Omega(t)}}{dt}|_{\Omega(0)} \tag{4.50}$$

4.8. SOLVER SETTINGS

Navier-Stokes equations are solved by weak constraints with Parallel-Direct-Sparse-Solver (PARDISO) with 10^{-2} relative tolerance and 10^{-3} absolute tolerance. The solver maximum time step is selected as 10^{-2}. With these solver parameters, parametric CFDs are solved 5 hours average except the ones with six number of helical waves which are solved almost 30 hours, Intel Xeon processor workstation with 96 GB RAM and running on CentOS Linux operating system.

CHAPTER 5

RESULTS

Experiments and modeling of onboard-powered autonomous swimmer are presented in this thesis. Robots consist of a bullet shaped glass tube body and a helical tails which are made of steel wires. A revolute joint is used to transfer the motion between these two parts. Actuation (a DC motor), a switch and the battery of the robot contained within body. ,

Two sets of experiments are carried out in open-ended tubes which are filled with silicon oil. These tubes have 3.6 cm and 2.4 cm diameters. Experiments with 3.6 cm tube are named as *Channel 1* experiment, while with 2.4 cm tube is named as *Channel 2*. The measurements are done with respect to 15 different configurations of helical tail for *Channel 1* and 9 different configurations of helical tail for *Channel 2*. For each case, experiments are repeated for at least three times. The linear velocity of swimmer and angular velocities of the body and tail are calculated from the images in 2-minute videos for each robot.

Three sets of non-dimensional CFD model are carried out. This non-dimensional model is done with respect to parameters of robots which are used in experimental process. First one is representing the *center* motion of robots in *Channel 1*, and the second one is representing same kind of motion in *Channel 2*. The last set is representing *off-center* motion of robots in *Channel 1*. *Center* motion of *Channel 1* and *2* simulations are done for 15 and 5 different configurations of helical tail, respectively; and, the *off-center* motion simulation in *Channel 1* is done for 11 different configurations. Furthermore, the angular velocities of tail, which are calculated from experiments, are fed into these simulations. Measured forward velocities and angular velocities of the body are compared with the calculations from both the RFT and CFD model

In the RFT model, two different resistive force coefficients are used which are Lighthill's resistive force coefficients for free swimmer and Lauga's resistive force coefficients which are including the wall boundary distance parameter.

In this chapter, time average experimental, COMSOL and RFT results are presented.

5.1. TIME AVERAGE EXPERIMENTAL, COMSOL AND RFT RESULTS

In experiments, prototypes' helical tails are twisted in counter clockwise direction and analysis is done with respect to forward propulsion. As a result, forward propulsion is ensured when, the tail rotates in clockwise direction and body rotates in counterclockwise direction as seen from the front. This forward propulsion is due to the reaction force from the interaction between the rotating tail and the surrounding viscous fluid similar to cork screw motion in solids. This propulsion can be generated only in Stokes flow, where the viscous forces are dominant. The reaction force on the tail from the fluid due to tails rotation also acts on the whole body via revolute joint between the tail and the body. This propulsion force of the tail is balanced by the drag force of the swimmer that travels with linear velocity which is the result of force free motion.

Similarly the torque generated by the motor acts in opposite directions on the tail and the body due to torque free motion. In the robot, motor's rotor is connected to the tail, and the stator to the body. Thus, motor's total angular velocity $2\pi f + \Omega$ are divided between body and tail such as Ω and f, respectively.

Channel 1 and Channel 2 experimental results are compared with calculations from the RFT model and COMSOL simulations.

5.1.1. *Channel 1* Results

5.1.1.1. RFT and Experimental Results in *Channel 1*

Channel 1 experiments are done with the cylindrical tube of diameter 3.6 cm. In experiments, linear velocity of the robot, rotation rates of the body and the tail are measured. The rotation rate of the tail is fed into RFT model as input, and model's outputs, linear velocity of the robot and the angular velocity of the body are compared with experimental measurements. In RFT model, different resistive force coefficients are used as Lighthill's free swimmer coefficients and Lauga's coefficients which include the wall boundary effect.

Due to non-standard shape of the body, and near bottom-wall swimming conditions of the robots in experiments, theoretical drag coefficients given by are modified [21]. As a result, both linear and angular drag coefficients of the body are tuned due to add the friction between

the body and the channel into RFT model. An important point is that tuning the rotational drag coefficient of the body modifies only the angular velocity of the body calculations and same issue is occurring while tuning the linear drag coefficient of the body. In other words, in the RFT model, tuning rotational and linear drag coefficients of the body only affect the tuned related velocity parameter of the system. These tuned drag coefficients are:

For RFT model with Lighthill's SBT resistive force coefficients:

$$\begin{bmatrix} D^F_{U,Li} \\ D^T_{\Omega,Li} \end{bmatrix} = \begin{bmatrix} 9\ (kg/s) \\ 2.83 \times 10^{-4} (kgm^2/s) \end{bmatrix} \tag{5.1}$$

For RFT model with Lauga's resistive force coefficients:

$$\begin{bmatrix} D^F_{U,La} \\ D^T_{\Omega,La} \end{bmatrix} = \begin{bmatrix} 9\ (kg/s) \\ 2.27 \times 10^{-4} (kgm^2/s) \end{bmatrix} \tag{5.2}$$

Also, in RFT-with-wall-correction, i.e. RFTwall, calculations, the distance from bottom wall, d_{ch} , is selected as d_{ch} = 0.012 cm. In graphs, experimental results are indicated as 'exp', RFT results with Lighthill's coefficients are indicated as 'RFT' and with Lauga's coefficients are indicated as 'RFTwall.

Table 5.1: Standard Deviation Calculations for Forward Speeds in *Channel 1*

ROBOTS	U_{std} (± %)	$U_{RFT,error}$ (%)	$U_{RFTwall,error}$ (%)
A_2	2.836	5.6691	2.449
A_3	3.3898	13.7678	14.1746
A_4	7.1306	38.9236	30.5439
A_6	3.4595	106.6667	82.7027
B_2	9.7284	22.451	33.6702
B_3	8.4337	31.5663	32.1446
B_4	2.0833	15.3646	12.1875
B_6	5.873	47.8095	54.522
C_2	15.5364	13.4572	28.0395
C_3	8.4112	11.4019	21.1215
C_4	1.4301	5.8538	7.4417
C_6	8.6712	10.032	34.039
D_3	3.0928	35.827	18.9868
D_4	10	38.3771	10.8229
D_6	7.4424	46.1099	18.365

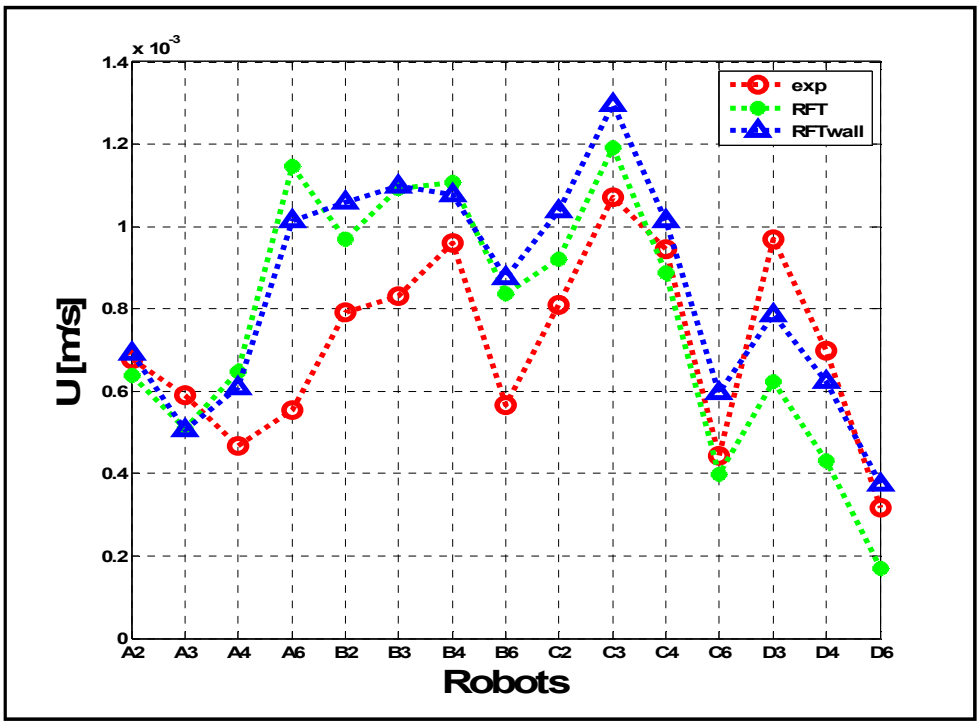

Figure 5.1: Forward Speeds vs. Robots for *Channel*

From Figure 5.1, it can be seen experimental measurements and both RFT and RFTwall calculations have the same trend. For RFT calculations with Lighthill's free swimmer resistive force coefficients, according to Table 5.1, robots A_2 (5.6691 %), C_2 (13.4572 %), and C_6 (10.032 %) almost remain outside one-sigma around the measurements; in fact robots A_6 (106.6667 %), B_3 (31.5663 %) and B_6 (47.8095 %) have large discrepancy with the experimental results. For RFTwall calculations which are done with Lauga's resistive force coefficients, according to Table 5.1, robots A_2 (2.449 %), C_4 (7.4417 %) and D_4 (10.8229 %) almost remain outside one-sigma around the measurements; on the other side, robots A_6 (106.6667 %), B_6 (54.522 %) and C_6 (34.039 %) have large discrepancy with the experimental results. What is interesting in this data which is seen in Table 5.1 that, RFTwall results are more agreeable than the RFT results for the robots (D robots) with the radius of 4 mm.

Table 5.2: Standard Deviation Calculations for Forward Speeds in *Channel 2*

ROBOTS	Ω_{std} *(± %)*	$\Omega_{RFT,error}$ *(%)*	$\Omega_{RFTwall,error}$ *(%)*
A_2	14.2536	25.9714	24.5399
A_3	5.9824	38.1911	46.6969
A_4	28.4345	30.5838	47.72
A_6	15.771	11.4486	45.7944
B_2	1.9342	11.6313	8.4126
B_3	8	2.3636	8.7273
B_4	2.9116	3.8292	22.181
B_6	23.5036	16.7983	38.9152
C_2	20.7887	1.7857	6.3988
C_3	4.1505	24.3612	20.4894
C_4	23.5069	14.7484	5.3456
C_6	5.3171	7.264	15.8468
D_3	6.72	8	0.64
D_4	8	9.2727	2.3636
D_6	7.9922	30.2144	21.8324

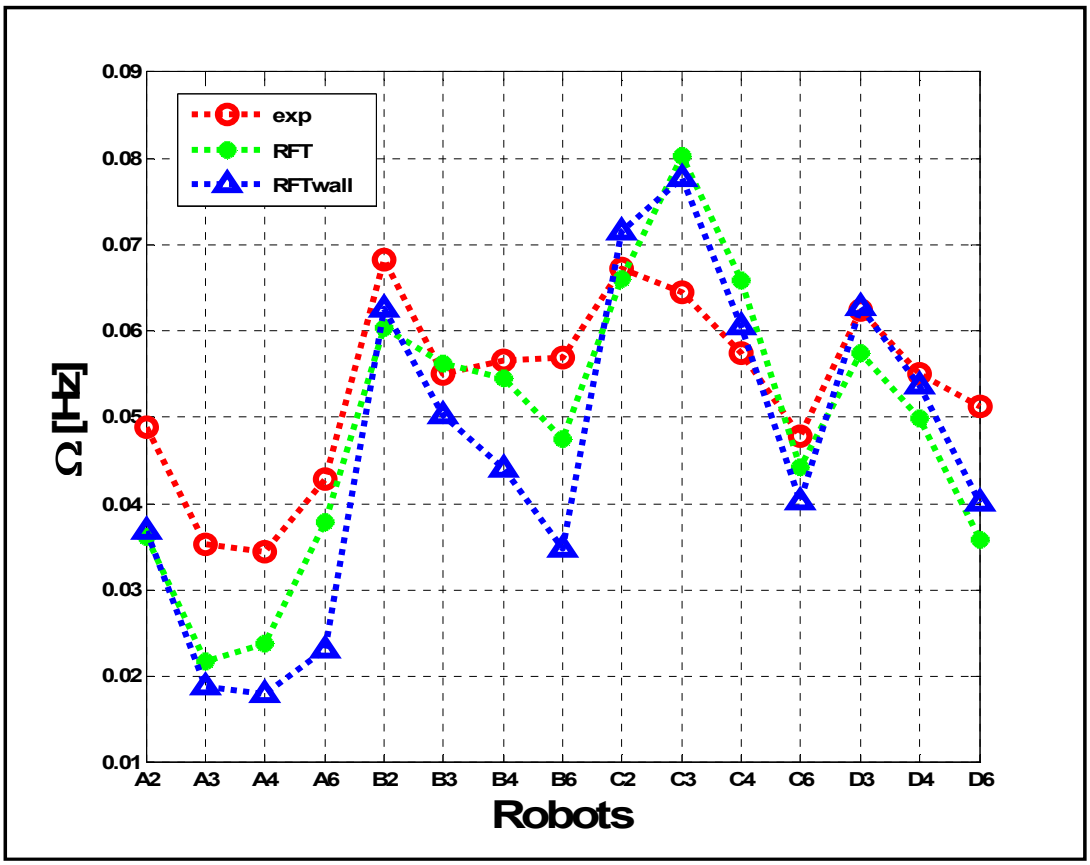

Figure 5.2: Body Rotations vs. Robots for *Channel 1*

From Figure 5.2 it can be seen that the body rotations' trend is almost same for experimental observations, RFT and RFTwall calculations. For RFT calculations with Lighthill's free swimmer resistive force coefficients, according to Table 5.2, robots B_3 (2.3636 %), B_4 (3.8292 %) and C_2 (1.7857 %) exactly remain outside one-sigma around the measurements; in fact robots A_3 (38.1911 %), B_2 (11.6313 %) and C_3 (24.3612 %) have large discrepancy with the experimental results. For RFTwall calculations which are done with Lauga's resistive force coefficients, according to Table 5.2, robots C_2 (6.3988 %), D_3 (0.64 %) and D_4 (2.3636 %) exactly remain outside one-sigma around the measurements; on the other hand, robots A_3 (46.6969 %), A_4 (47.72 %) and A_6 (45.7944 %) have large discrepancy with the experimental results.

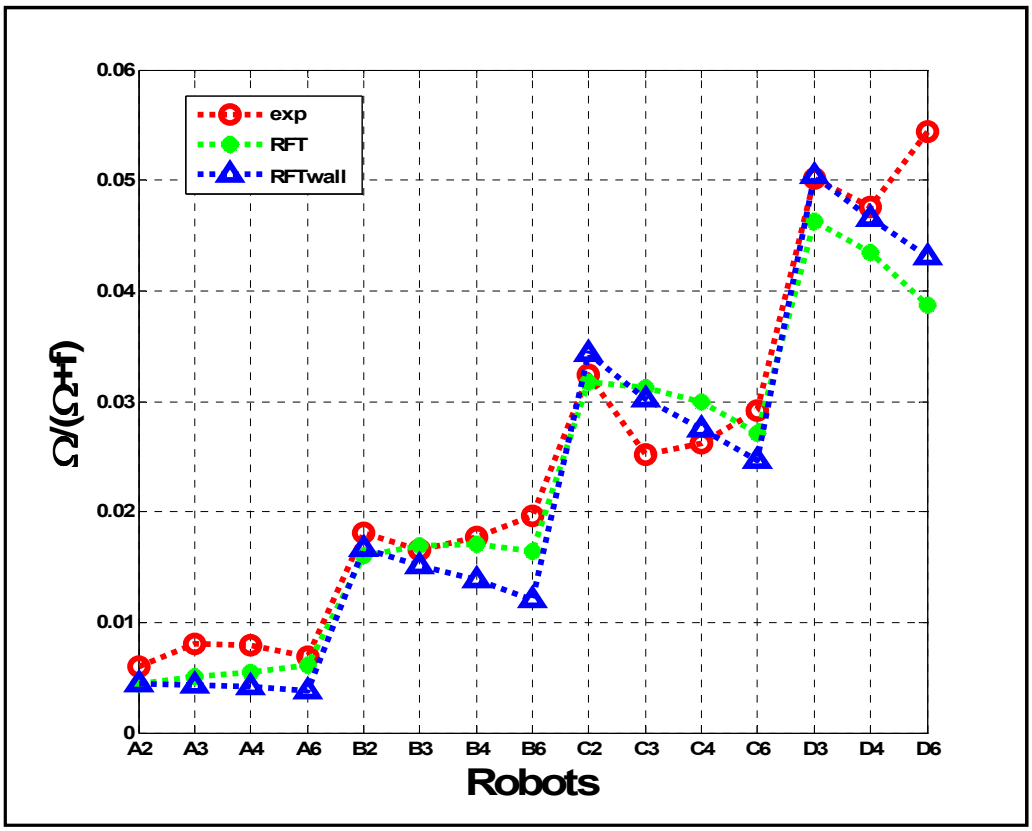

Figure 5.3: Ratio of Body Rotations to Motor Rotations vs Robots for *Channel 1*

The Figure 5.3 shows the ratio of head rotation rate to motor rotation rate. It can be observed from this figure that, both coefficients suggested by Lighthill and Lauga, underestimate this ratio except for the robots with 3 mm amplitude. Both RFT and RFTwall show decreasing trend of amplitude groups, except the amplitude of 2 mm. However, experimental measurements show convex trend for each amplitude group. This trend only differs for the robots with 2 mm amplitude. Because of this trend differences between the experiments and RFT, RFTwall models, the robots with six helical waves which are A_6, B_6, C_6 and D_6 show large discrepancy.

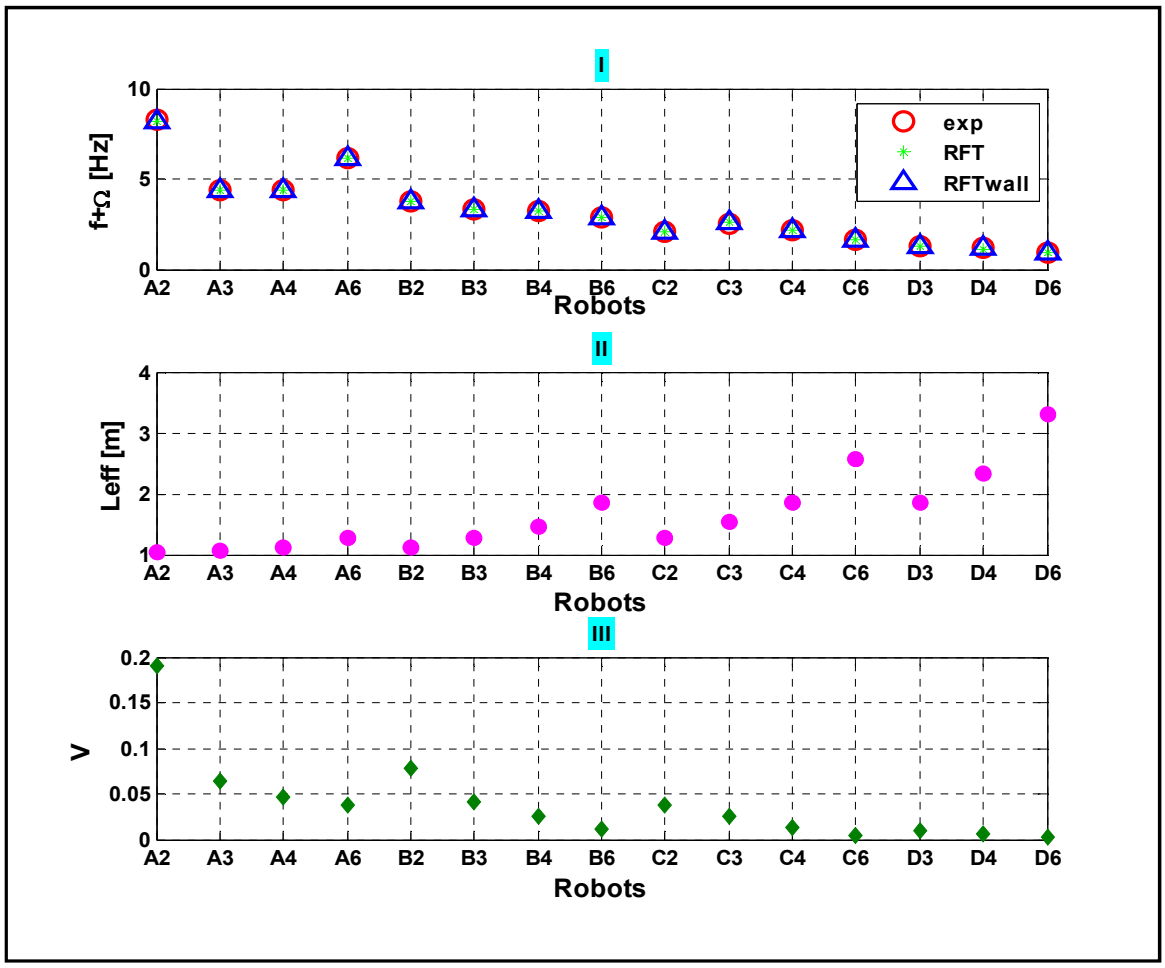

Figure 5.4: I. Total motor rotations vs. Robots; II. Effective length vs. Robots; III. Linear Wave Propagation Speeds vs. Robots

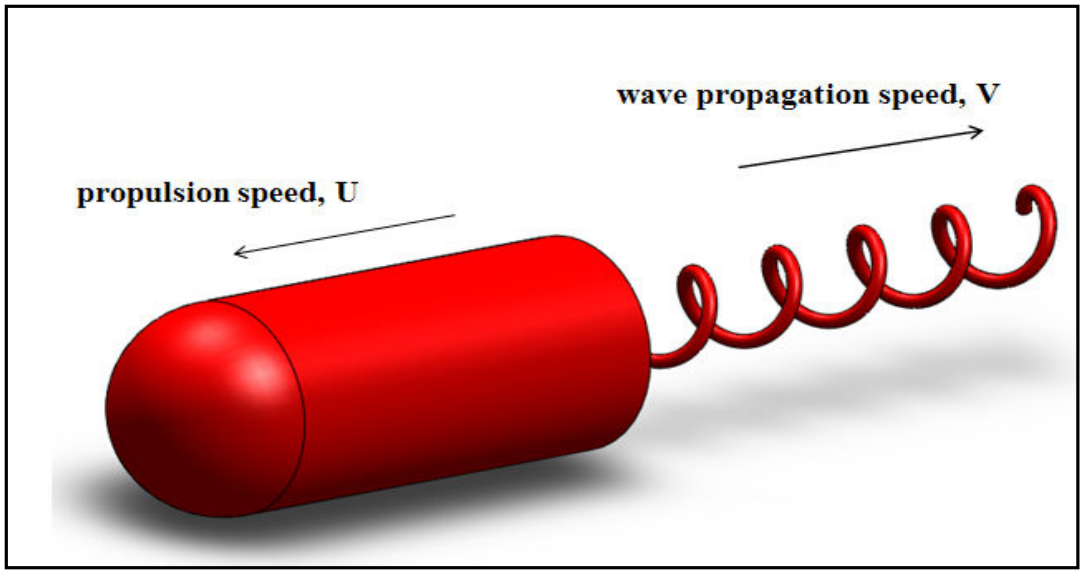

Figure 5.5: Forward Speed and Wave Propagation Speed for Helical Propeller System

The average linear velocity (U) of the robots are normalized by the wave propagation speed (V) on the tail's curvilinear coordinates, and compared with the normalized speed from experiments. The linear wave propagation speed on the tail is given by:

$$V = f\lambda\alpha \tag{5.3}$$

Here f is the frequency of the rotation of the tail, λ is the wavelength (helical pitch) and α is a coefficient that quantifies the ratio between the effective total length of the tail, L_{eff}, and the helical apparent length L, such as:

$$\alpha = \frac{L}{L_{eff}} \tag{5.4}$$

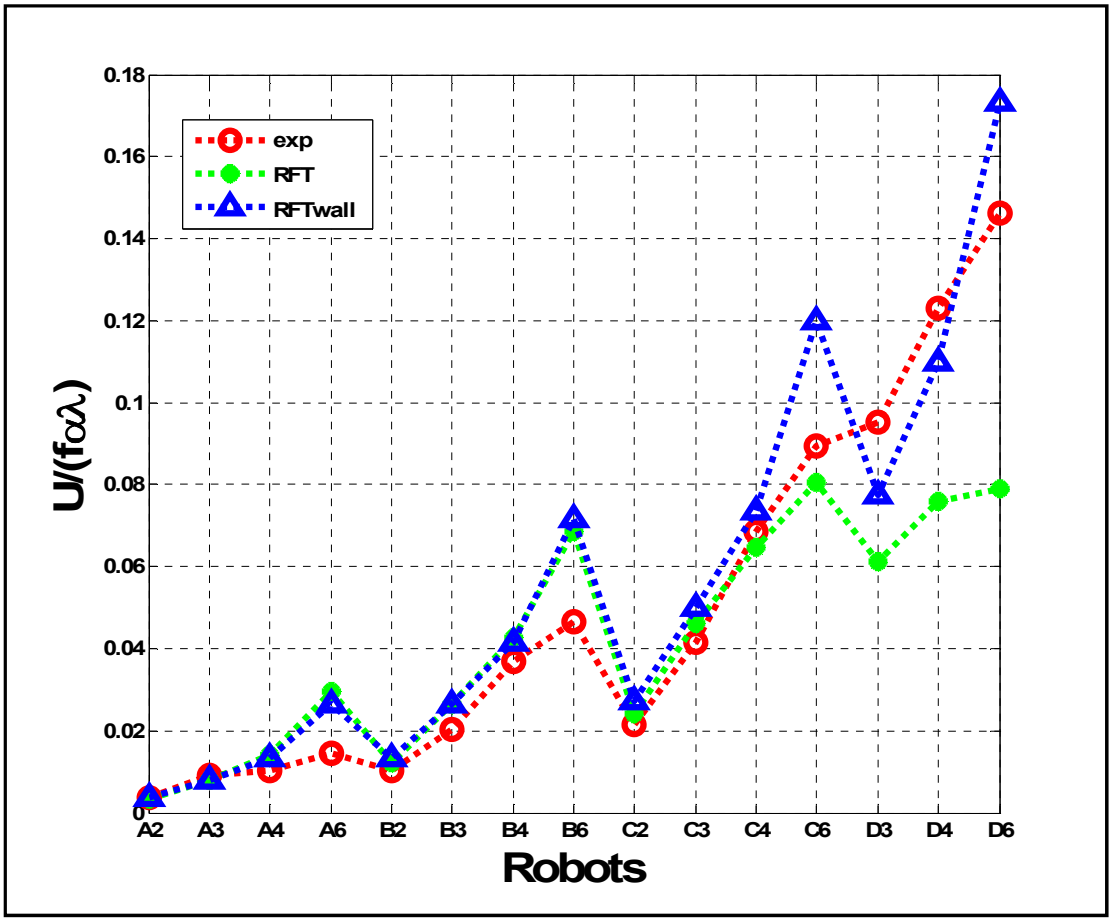

Figure 5.6: Linear Wave Propagation Speeds vs. Robots in *Channel 1*

Normalized average linear velocity for each robot agrees reasonably well with both RFT and RFTwall calculations. The same analysis for velocity vs. robots is true for normalized velocity such that for RFT calculations with Lighthill's free swimmer resistive force coefficients, according to Table 5.1, robots A_2 (5.6691 %), C_2 (13.4572 %) and C_6 (10.032 %) almost remain outside one-sigma around the measurements; in fact robots A_6 (106.6667 %), B_3 (31.5663 %) and B_6 (47.8095 %) have large discrepancy with the experimental results. For RFTwall calculations which are done with Lauga's resistive force coefficients, according to Table 5.1, robots A_2 (2.499 %), C_4 (7.4417 %) and D_4 (10.8229 %)

almost remain outside one-sigma around the measurements; on the other side, robots A_6 (106.6667 %), B_6 (54.522 %) and C_6 (34.039 %) have large discrepancy with the experimental results.

From Figure 5.4, it is observed that total frequency of the system has a decreasing trend with respect to robots. Also, it is seen from the Figure 5.3, the angular frequency ratio to total frequency of the helical propeller system has increasing while the amplitude of the robots increasing, too; hence, it leads to decrease the effective rotation rate of the helix. Although the effective length has increasing trend as it seen from Figure 5.4, the decreasing rate of frequency is higher than the increasing rate of effective length thus, linear wave propagation speed has decreasing trend with respect to robots. Therefore, as seen from Figure 5.6, scaling propulsive speeds with linear wave propagation speeds results in increasing trend. Furthermore, it is apparent from the Figure 5.6 that, this trend shows some different behavior between experimental measurements, RFTwall and RFT models. No significant difference is found from A_2 robot to D_4 robot but, the most striking result to emerge from the data can be seen for D_6 robot. In there, the normalized velocity of robot is limited in RFT model by 7.88 % but, in experiments and RFTwall model this normalized velocity increases beyond this limit; robot reaches up to 14.64 % for experiments and 17.32 % for RFTwall model. As a result, overall, Lauga's coefficients are superior to Lighthill's coefficients in modeling swimming of helical waves within wall bounded environment with 1.8 cm radius.

.

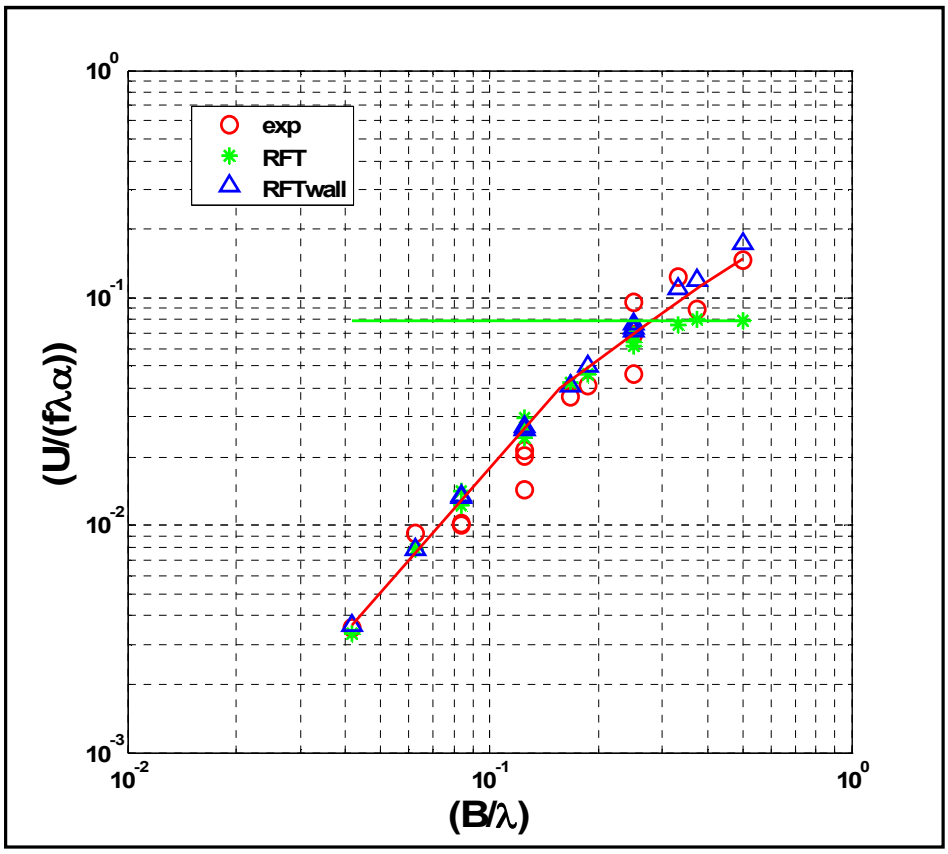

Figure 5.7: log(*B*/*λ*) vs. log(*U*/*V*) for *Channel 1*

In Figure 5.7, measurement and the results of RFT and RFTwall are plotted with respect to *B*/*λ*, which the constant pitch angle as:

$$tan\beta = \frac{2\pi B}{\lambda} \tag{5.5}$$

From Figure 5.7, as the pitch angle increases, tail exerts more force on the fluid hence, forward thrust ability also increases for helical propeller system. Due to increase in thrust force, the system forward speed gets closer to linear wave propagation speed. But the normalized velocity of robot is limited in RFT model by 7.88 % but, in experiments and RFTwall model this normalized velocity increases beyond this limit; robot reaches up to 14.64 % for experiments and 17.32 % for RFTwall model. Although RFTwall model overestimates this ratio, both the experimental measurements and RFTwall simple model have same increasing trend which shows that Lauga's coefficients are superior than Lighthill's ones for *Channel 1*.

5.1.1.2. Experimental, RFT and COMSOL Results in *Channel 1*

Helical propeller system with bullet shaped body is analyzed in COMSOL within two simulation sets for *Channel 1*. One of the set is representing *center* motion of this propeller system in and the other one is representing the *off-center* motion of this system which is much more similar motion trend with respect to experiments. These two different sets are significant due to understanding of wall distance effect to this helical propeller system in same channel. From Section 5.1.1.1 it is resulted that, Lauga's resistive coefficients are working better for *Channel 1* experimental measurement thus, the figures below, these experimental results are compared with RFTwall model and two different COMSOL simulation sets.

In graphs, experimental results are indicated as 'exp', RFT results with Lauga's coefficients are indicated as 'RFTwall', COMSOL "*center*" simulations are indicated as CFDc and COMSOL "*off-center*" simulations are indicated as CFDoc.

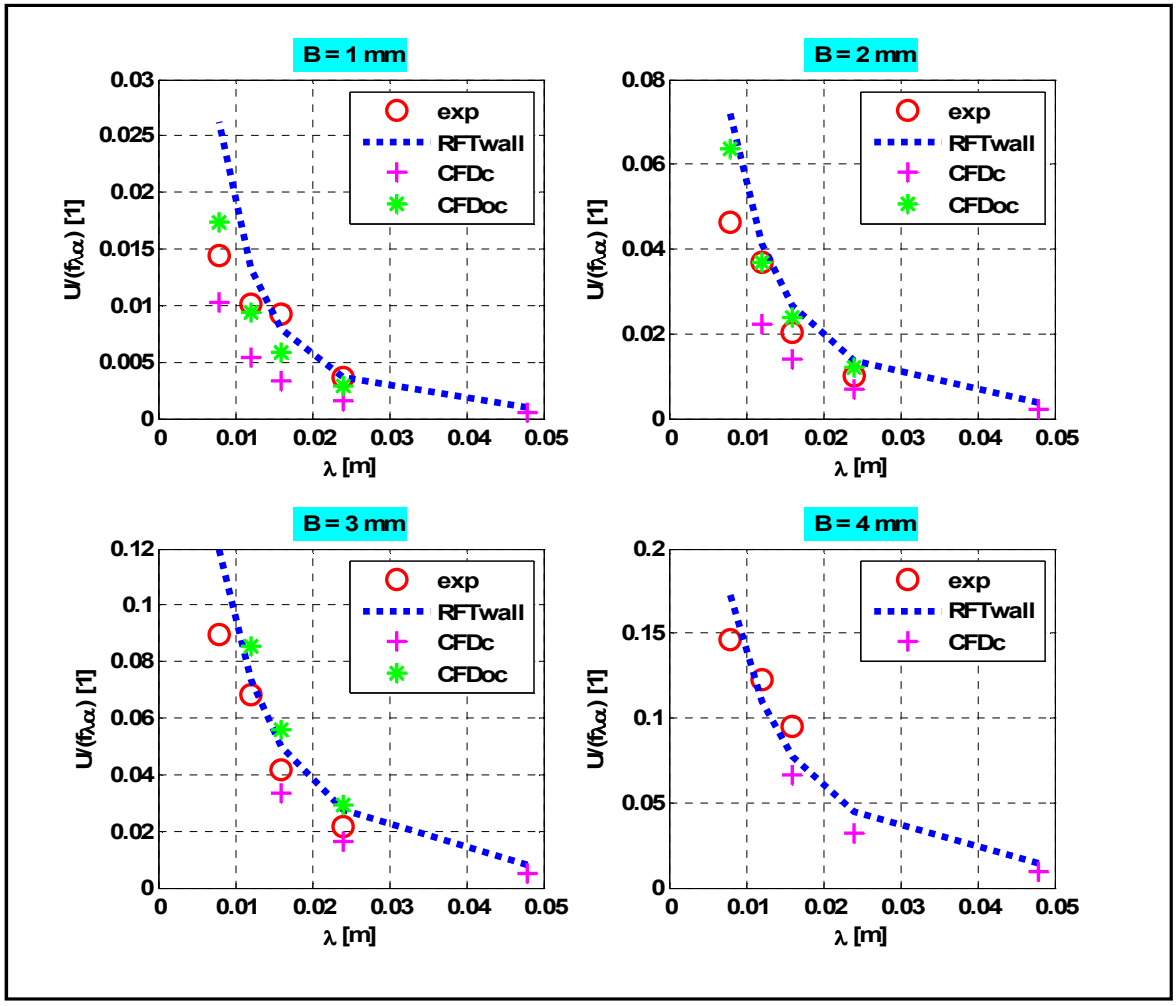

Figure 5.8: *U/V* vs. Wavelength for *Channel 1*

In Figure 5.8, measurements, the results of RFTwall model, CFDc (*center* simulations) and CFDoc (*off-center* simulations) are plotted with respect wavelength, λ. As seen from figure, with increasing wavelength λ (decreasing number of waves) leads to decrease in thrust force; thus, the ratio of propulsive speeds to linear wave propagation speeds decrease and this trend can be observed for all amplitudes. In addition to that, comparing the results of CFDoc and CFDc, it is obvious that CFDoc gives better approximation than CFDc ones with respect to experimental results. First it must be mentioned that, these CFDoc and CFDc simulations are done with same frequencies for same helical tail parameters. To reach the same induced frequencies for same helical tail parameters, CFDoc thrust forces must increase to win increasing shear forces which are caused by closer position to bottom wall.

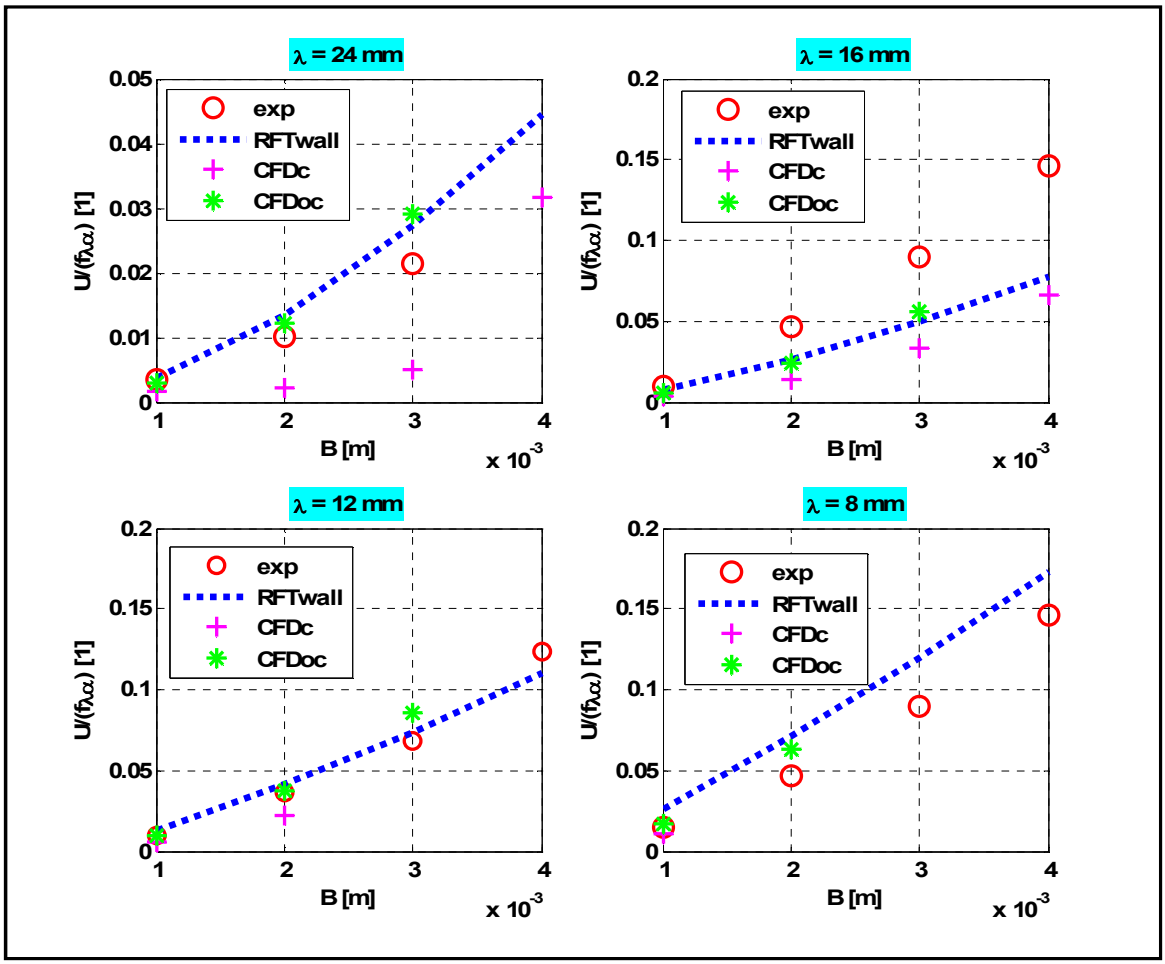

Figure 5.9: *U/V* vs Amplitude for *Channel 1*

In Figure 5.9, measurements, the results of RFTwall model, CFDc (*center* simulations) and CFDoc (*off-center* simulations) are plotted with respect amplitude, *B*. Increasing amplitude *B* leads to increase in thrust force; thus, the ratio of forward speeds to linear wave

propagation speeds increase and this trend can be observed for all amplitudes. In addition to that, like the wavelength graph, comparing the results of CFDoc and CFDc, it is obvious that CFDoc gives better approximation than CFDc ones with respect to experimental results. Also, these CFDoc and CFDc simulations are done with same frequencies for same helical tail parameters. In a same way with wavelength analysis, to reach the same induced frequencies for same helical tail parameters, thrust forces in the CFDoc is higher than CFDc ones due to win increasing shear forces which are caused by closer position to bottom wall. In other words, this increasing trend is causing due to cope with this increasing shear forces.

5.1.2. *Channel 2* Results

5.1.2.1. RFT and Experimental Results in *Channel 2*

Channel 2 experiments are done within 2.4 cm diameter cylindrical tube. Like the experiments in *Channel 1,* linear velocity of the robot, rotation rates of the body and tail are measured. For RFT and RFTwall calculations, same process is valid with *Channel 1* that, measured frequencies are fed into analytical models to calculate the propulsive speeds and rotation rates of the body. Again, two different resistive force coefficients are used that for free swimmer Lighthill's and for channel correction Lauga's coefficients are valid. Also, the tuned parameters are needed to reflect the additional frictional effects of bounded surfaces into analytical model. These tuned drag coefficients are:

For RFT model with Lighthill's resistive force coefficients:

$$\begin{bmatrix} D^F_{U,Li} \\ D^T_{\Omega,Li} \end{bmatrix} = \begin{bmatrix} 119.36\ (kg/s) \\ 3.4 \times 10^{-4} (kgm^2/s) \end{bmatrix} \tag{5.6}$$

For RFT model with Lauga's resistive force coefficients:

$$\begin{bmatrix} D^F_{U,La} \\ D^T_{\Omega,La} \end{bmatrix} = \begin{bmatrix} 128.5\ (kg/s) \\ 2.267 \times 10^{-4} (kgm^2/s) \end{bmatrix} \tag{5.7}$$

For RFTwall calculations, the distance from bottom wall, d_{ch}, is selected as d_{ch}= 0.001 cm. In graphs, experimental results are indicated as 'exp', RFT results with Lighthill's coefficients are indicated as 'RFT' and with Lauga's coefficients are indicated as 'RFTwall'.

Table 5.3: Standard Deviation Calculations for Propulsive Speeds in *Channel-2*

ROBOTS	U_{std} (± %)	$U_{RFT,error}$ (%)	$U_{RFTwall,error}$ (%)
B_3^*	12.376	61.441	24.244
B_4^*	7.874	81.67	36.33
B_6^*	28.86	60.756	30.9
C_3^*	13.154	58.478	33.566
C_4^*	6.345	18.37	27.26
C_6^*	24.8	4.85	11.386
D_3^*	43.344	2.571	0.439
D_4^*	57.734	30.716	46.235
D_6^*	69.276	5.2615	79.631

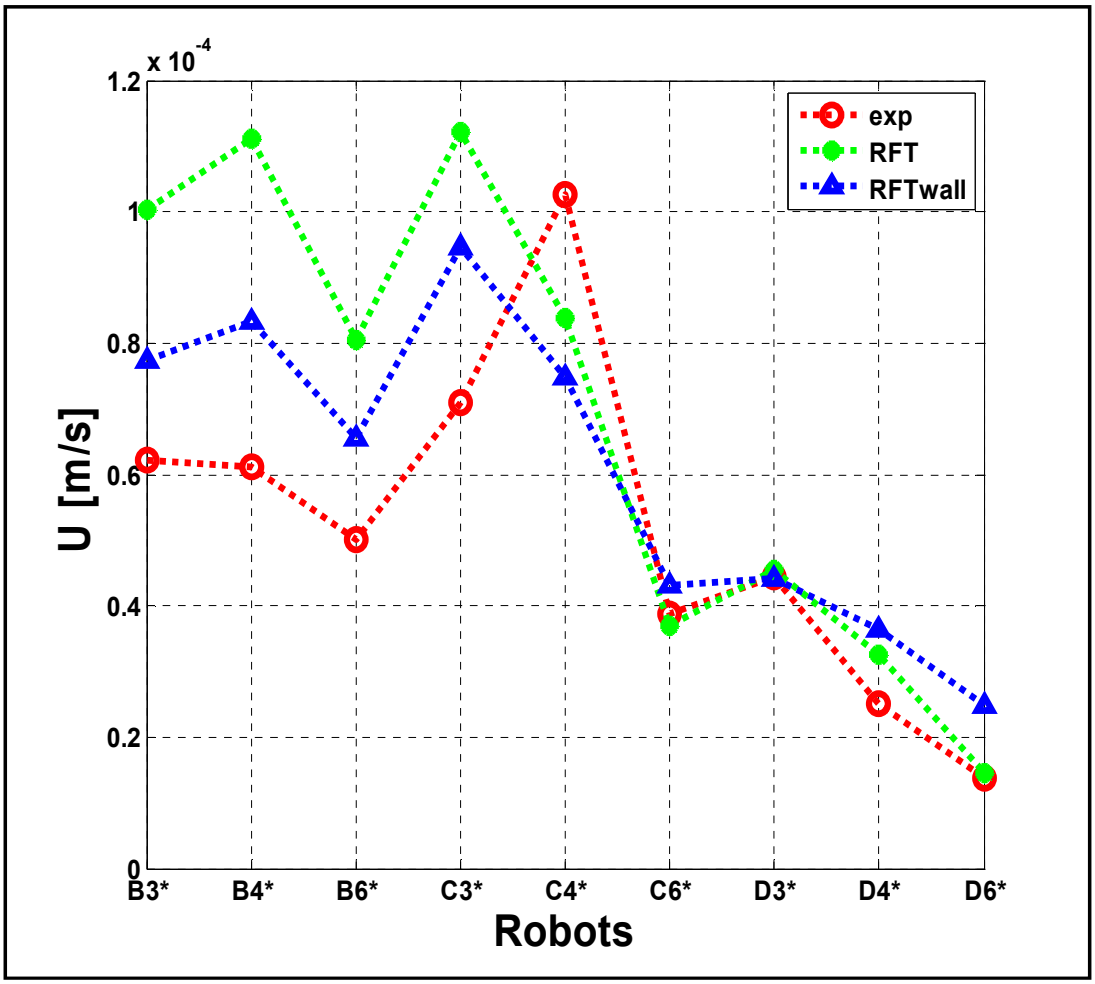

Figure 5.10: Propulsive Speeds vs. Robots in *Channel 2*

From Figure 5.10, it can be seen experimental measurements and both RFT and RFTwall calculations have the same trend. For RFT calculations with Lighthill's free swimmer resistive force coefficients, according to Table 5.3, robots C_6* (4.85 %), D_3* (2.571 %) and D_6* (5.2615 %) exactly remain outside one-sigma around the measurements; in fact robots B_4* (36.33 %), B_6* (60.756 %) and C_3* (58.478 %) have large discrepancy with the experimental results. For RFTwall calculations which are done with Lauga's resistive force coefficients, according to Table 5.3, robots B_3* (24.244 %), C_6* (4.85 %) and D_3* (2.571 %) almost remain outside one-sigma around the measurements; on the other hand, robots B_4* (36.33 %), D_4* (46.235 %) and D_6* (79.631 %) have large discrepancy with the experimental results.

It is apparent from RFTwall analysis that, this simple model cannot offer good approximation for the robots with 4 mm amplitudes (for D* robots). But interestingly, it shows better agreement than RFT model for other robots, except the D* ones.

Furthermore, from Table 5.1 and Table 5.3 it can be observed that, the forward speeds decrease dramatically in *Channel 2* with respect to *Channel 1*. This can be explained by Lauga's approach that these swimmers are swimming with constant power because design considerations are not changing between these two channels experiments. Thus, the presence of a boundary leads to decrease in propulsive speed because translational drag coefficient of the body increases when it comes closer to boundary and due to constant power, this drag force slows down thrust motion of robots. Also, increased drag coefficient can be observed from the tuned translational drag coefficients of the body that it is 9 (kg/s) for *Channel 1* while it is at least 119.36 (kg/s) for *Channel 2.*

Table 5.4: Standard Deviation Calculations for Body Rotations in *Channel-2*

ROBOTS	Ω_{std} (± %)	$\Omega_{RFT,error}$ (%)	$\Omega_{RFTwall,error}$ (%)
B_3^*	29.461	4.613	4.99
B_4^*	11.075	41.595	16.161
B_6^*	13.327	26.038	5.969
C_3^*	1.588	1.999	0.899
C_4^*	32	3.6	3.249
C_6^*	5.613	29.787	43.531
D_3^*	9.442	9.871	2.0342
D_4^*	16.221	2.827	4.421
D_6^*	14.369	26.8	18.454

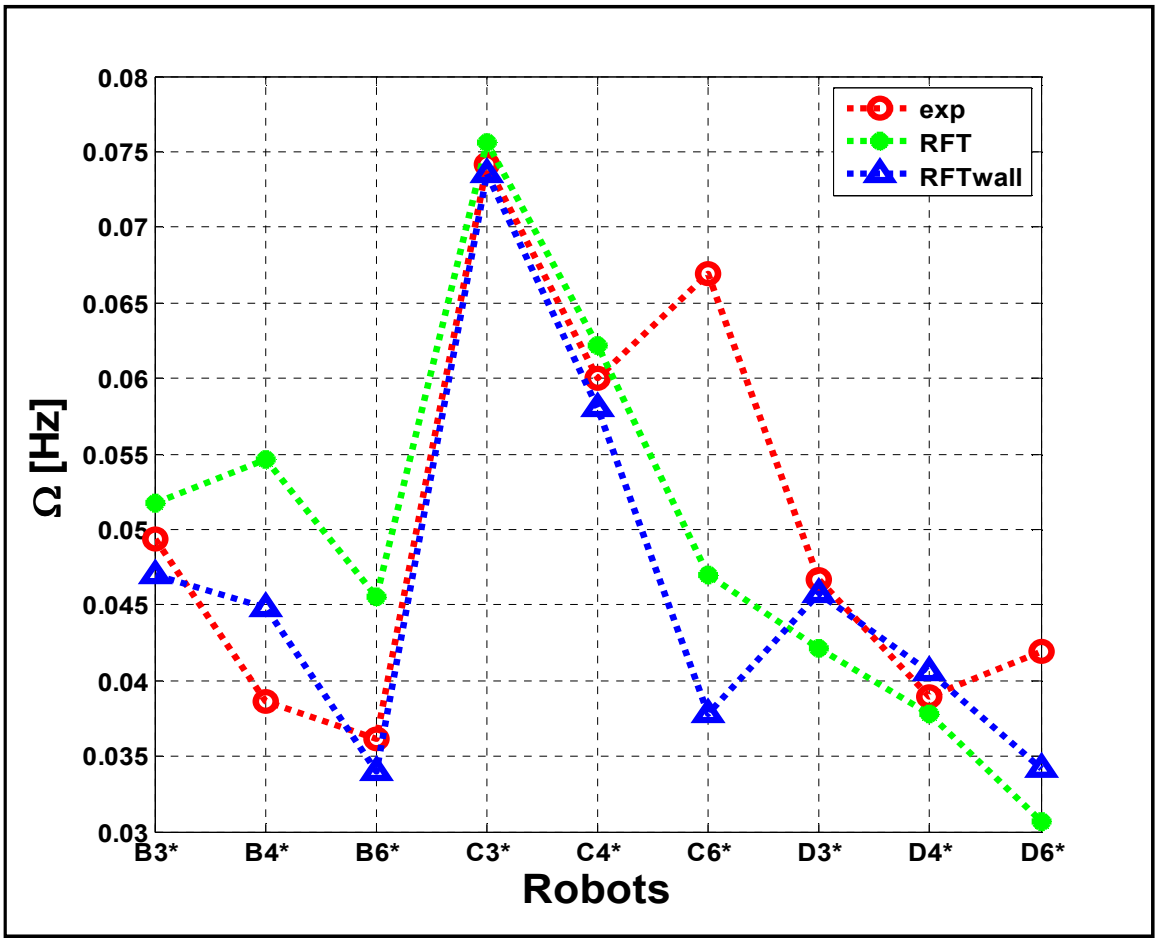

Figure 5.11: Body Rotations vs. Robots for *Channel-2*

From 5.11 it can be seen that the body rotations' trend is almost same for experimental observations, RFT and RFTwall calculations. For RFT calculations with Lighthill's free swimmer resistive force coefficients, according to Table 5.4, robots B_3* (4.613 %), C_3* (1.999 %) and D_4* (2.827 %) exactly remain outside one-sigma around the measurements; in fact robots B_4* (41.595 %), B_6* (26.038 %) and C_6* (29.787 %) have large discrepancy with the RFT and RFTwall results. For RFTwall calculations which are done with Lauga's resistive force coefficients, according to Table 5.4, robots B_3* (4.99 %), C_3* (0.899 %) and D_3* (2.0342 %) exactly remain outside one-sigma around the measurements; on the other hand, robots B_4* (16.161 %), C_6* (43.531 %) and D_6* (18.454 %) have large discrepancy with the experimental results.

The interesting result emerge from the data is that, there is no significant difference between the body rotations for same robots in *Channel 1* and *Channel 2*. It can be also observed from the tuned rotational body drag coefficients such that, it is at most $3.4\text{x}10^{-4}$ (kgm^2/s) for *Channel 2* while it is at most $2.83\text{x}10^{-4}$ (kgm^2/s) for *Channel 1*.

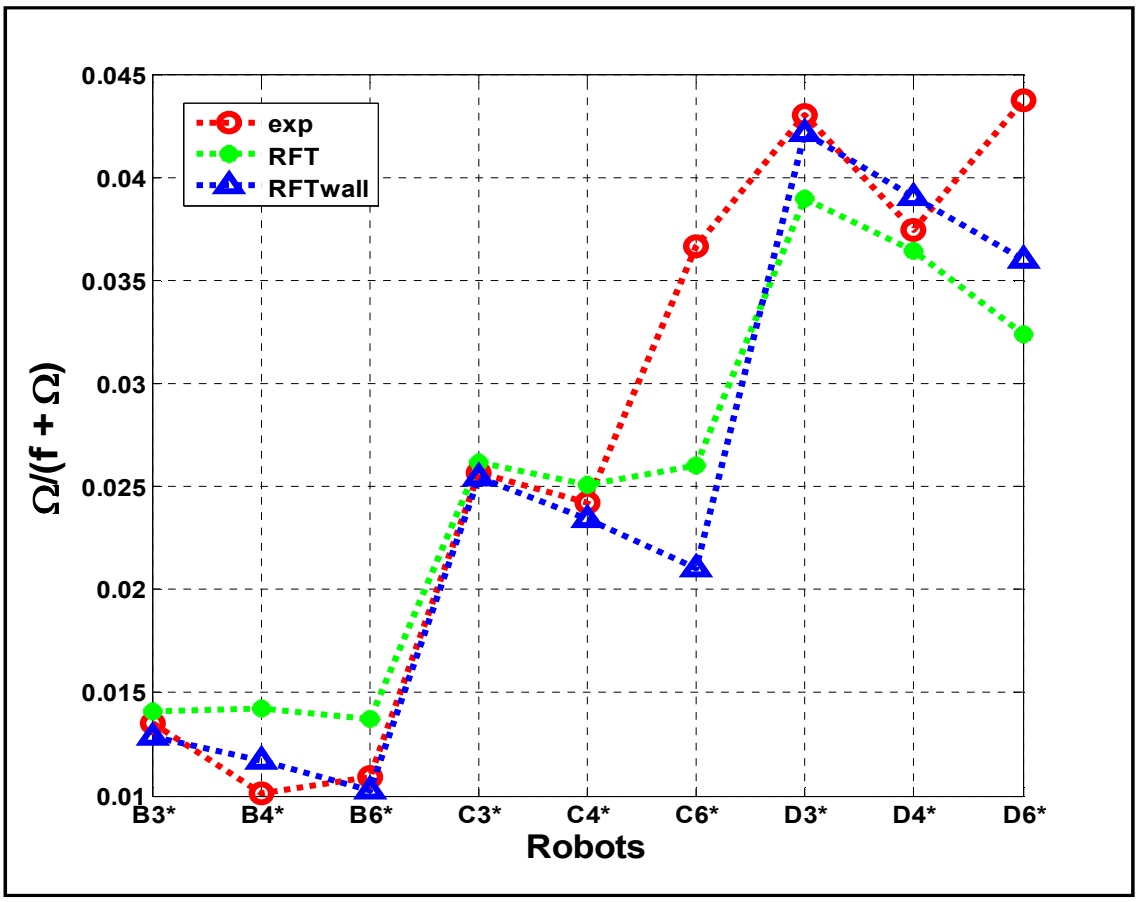

Figure 5.12: Ratio of Body Rotations to Motor Rotations vs. Robots in *Channel- 2*

The Figure 5.12 shows the ratio of head rotation rate to motor rotation rate. It can be observed from this figure that, both coefficients suggested by Lighthill and Lauga, underestimate this ratio except for the robots with number of waves are four as B_4*, C_4* and D_4*. Similarly to the results for the *Channel 1*, both RFT and RFTwall show decreasing trend for each amplitude group except the amplitude. However, experimental measurements show convex trend for each amplitude group. Because of this trend differences between the experiments, RFT, and RFTwall models, the robots with six helical waves which are C_6* and D_6* show large discrepancy.

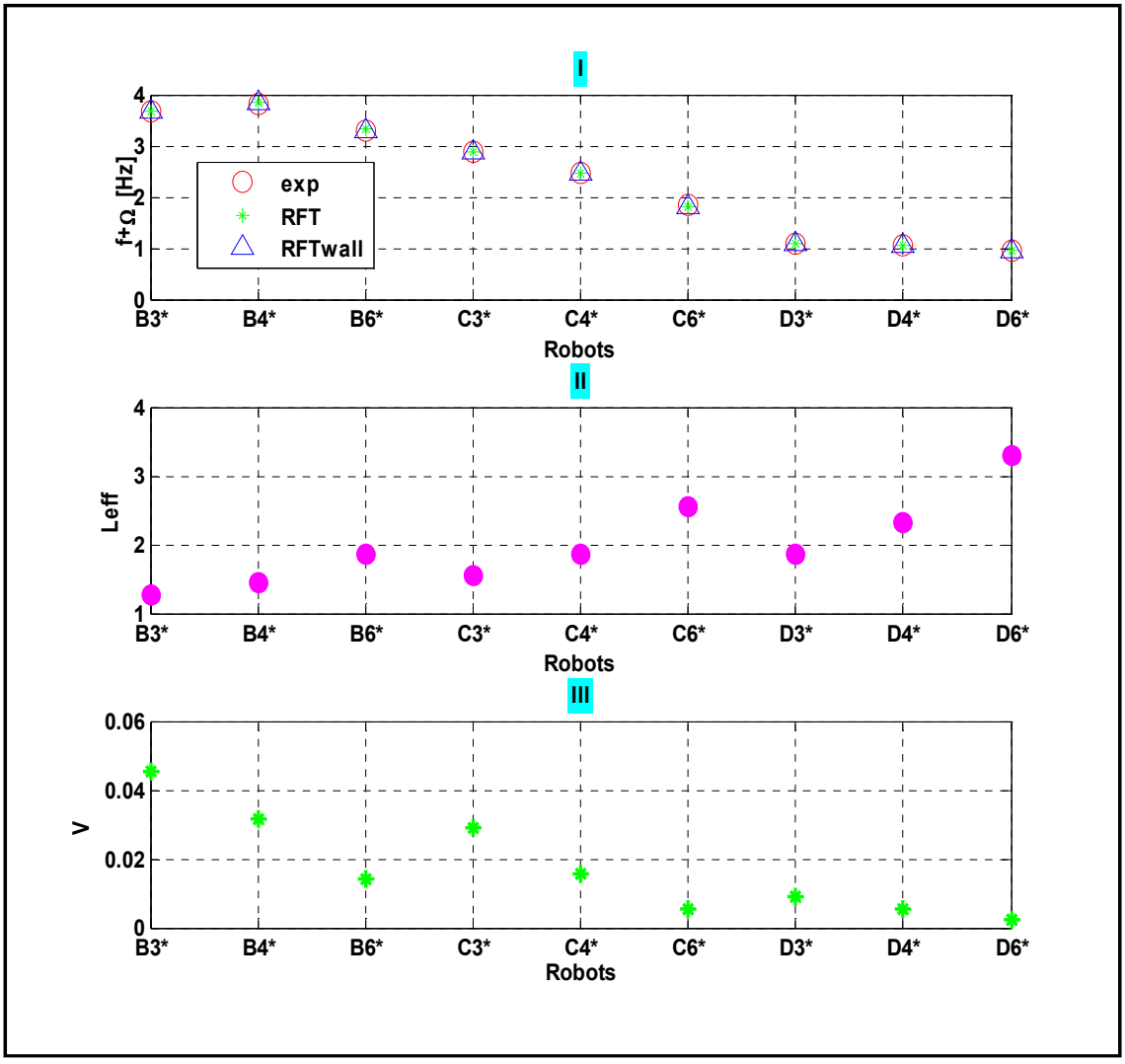

Figure 5.13: I. Total motor rotations vs. Robots; II. Effective lengths vs. Robots; III. Linear Wave Propagation Speeds vs. Robots

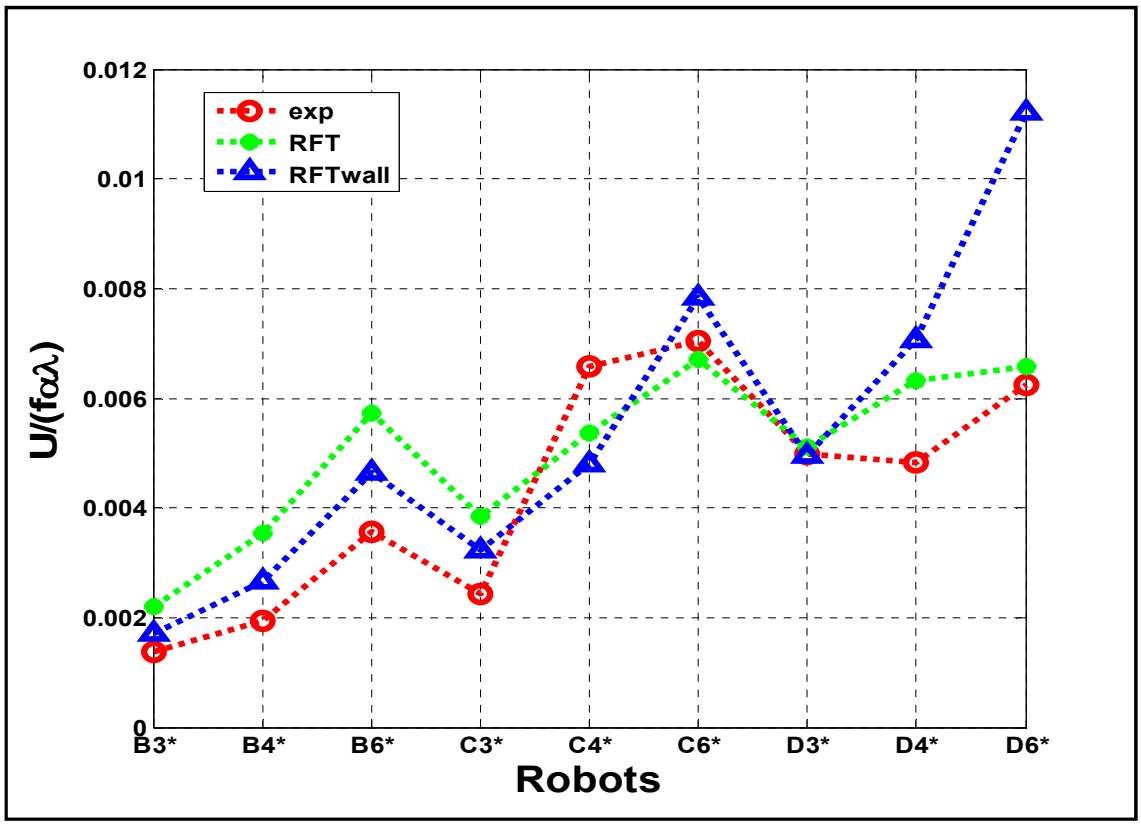

Figure 5.14: U/V vs. Robots in *Channel 2*

Normalized average linear velocity for each robot agrees reasonably well. The error analysis is same with propulsive speed that, for RFT calculations with Lighthill's free swimmer resistive force coefficients, according to Table 5.3, robots C_6* (4.85 %), D_3* (2.571 %) and D_6* (5.2615 %) exactly remain outside one-sigma around the measurements; in fact robots B_4* (36.33 %), B_6* (60.756 %) and C_3* (58.478 %) have large discrepancy with the experimental results. For RFTwall calculations which are done with Lauga's resistive force coefficients, according to Table 5.3, robots B_3* (24.244 %), C_6* (4.85 %) and D_3* (2.571 %) almost remain outside one-sigma around the measurements; on the other side, robots B_4* (36.33 %), D_4* (46.235 %) and D_6* (79.631 %) have large discrepancy with the experimental results.

Like the normalized velocity analysis for *Channel 1*, from Figure 5.13, it is observed that total frequency of the system has a decreasing trend with respect to robots. Also, it is seen from the Figure 5.12, the angular frequency ratio to total frequency of the helical propeller system has increasing while the amplitude of the robots increasing, too; hence, it leads to decrease the effective rotation rate of the helix. Although the effective length has increasing trend as it seen from Figure 5.13, the decreasing rate of frequency is higher than the increasing rate of effective length thus, linear wave propagation speed has decreasing trend

with respect to robots. Therefore, as seen from Figure 5.14, scaling propulsive speeds with linear wave propagation speeds results in increasing trend.

Furthermore, it is apparent from the Figure 5.14 that, this trend shows some different behavior between experimental measurements, RFTwall and RFT models. Except the robot C_4*, there is no significant behavior difference between experimental measurements and analytical models. But an interesting behavior can be observed for D_6* robot is that, the experimental datum behaves like RFT model and saturates to 0.6244 % of its linear wave propagation speed while the RFT model saturates to 0.6573 % of its wave propagation. On the other hand, for RFTwall model this normalized velocity increases beyond this limit that, robot reaches up to 1.122 % of its wave propagation speed. Although Lauga's coefficients agrees reasonably well with the experimental data, for the robots with amplitude 4 mm, Lighthill's coefficients offer better approximation.

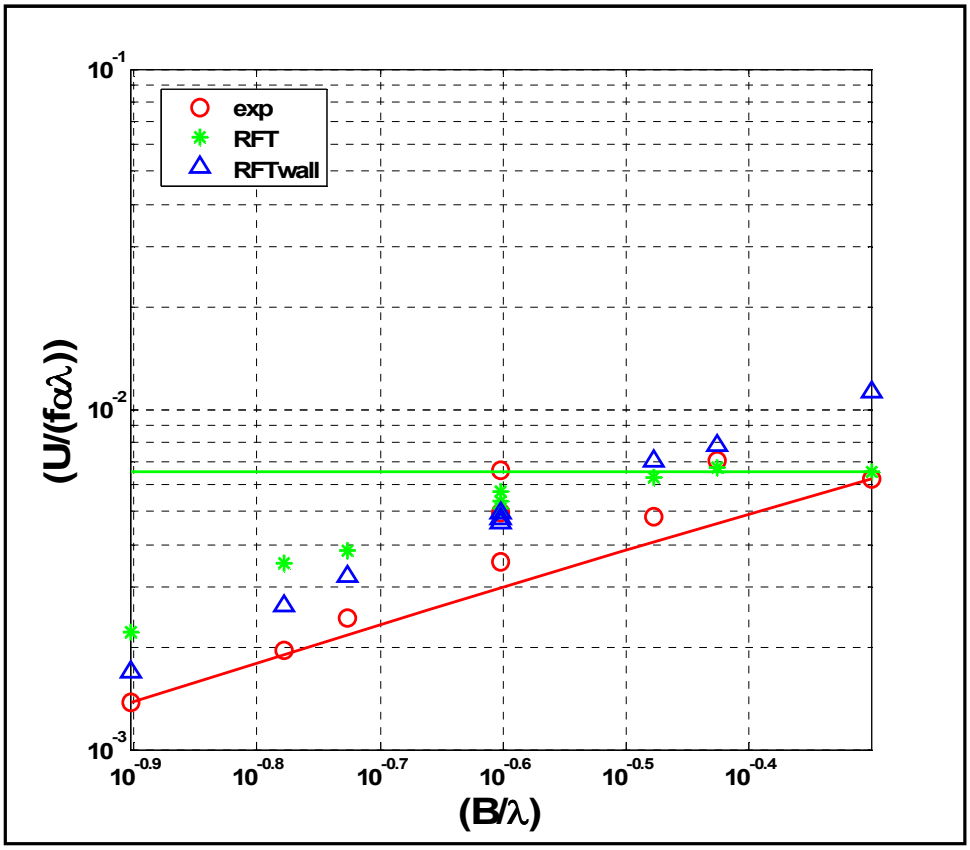

Figure 5.15: log(*B*/*λ*) vs. log(*U*/*V*) for *Channel- 2*

In Figure 5.15, measurement and the results of RFT and RFTwall are plotted with respect to B/λ, which the constant pitch angle as:

$$tan\beta = \frac{2\pi B}{\lambda} \tag{5.7}$$

Similar to the results obtained from *Channel 1*, from Figure 5.7, as the pitch angle increases, tail exerts more force on the fluid hence, forward thrust ability also increases for helical propeller system. Due to increase in thrust force, the system forward speed gets closer to linear wave propagation speed. But when the Figure 5.15 is compared with the Figure 5.7, it shows that, in *Channel 1*, experimental measurements are not limited unlike in *Channel 2*. In *Channel 2*, the normalized velocity is limited for both RFT model and experimental measurements that, in RFT it is limited by 0.6573 % and in experiments this limited value is 0.6244 %. On the other hand, in RFTwall model, this normalized velocity increases beyond this limit; robot reaches up to 1.122 %.

For the last robot, there is a difference trend between the experimental and RFTwall model, it can be observed from Table 5.3 and Table 5.4 that, RFTwall model offers better approximation than RFT one.

5.1.2.2.Experimental, RFT and COMSOL Results in *Channel 2*

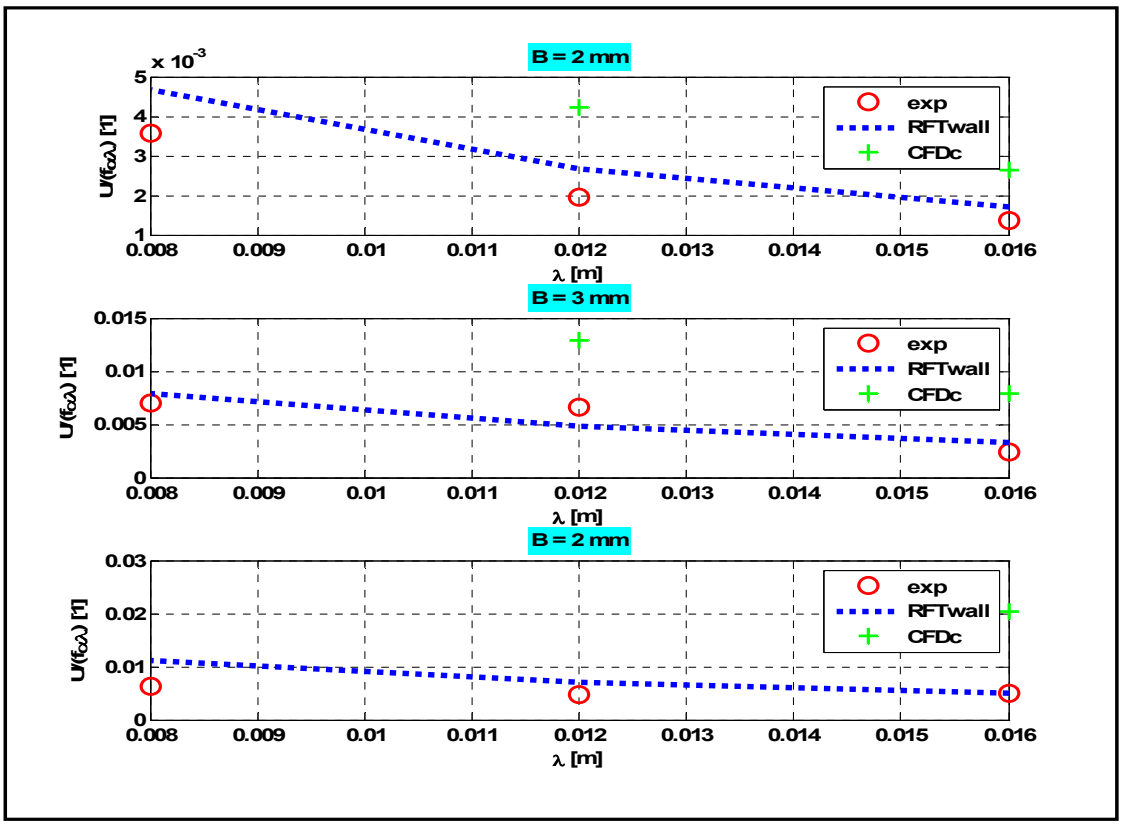

Figure 5.16: *U/V* vs. Wavelength for *Channel 2*

In Figure 5.16, measurements, the results of RFTwall model and CFDc (*center* simulations) are plotted with respect wavelength, λ. As seen from figure, with increasing wavelength λ (decreasing number of waves) leads to decrease in thrust force; thus, the ratio of forward speeds to wave speeds decrease and this trend can be observed for all amplitudes which are the same behavior within *Channel 1* observations. RFTwall model overestimates the experimental observations for 2 mm and 4 mm amplitudes while underestimates the one with 3 mm. For all amplitudes, CFDc models overestimate the experimental observations.

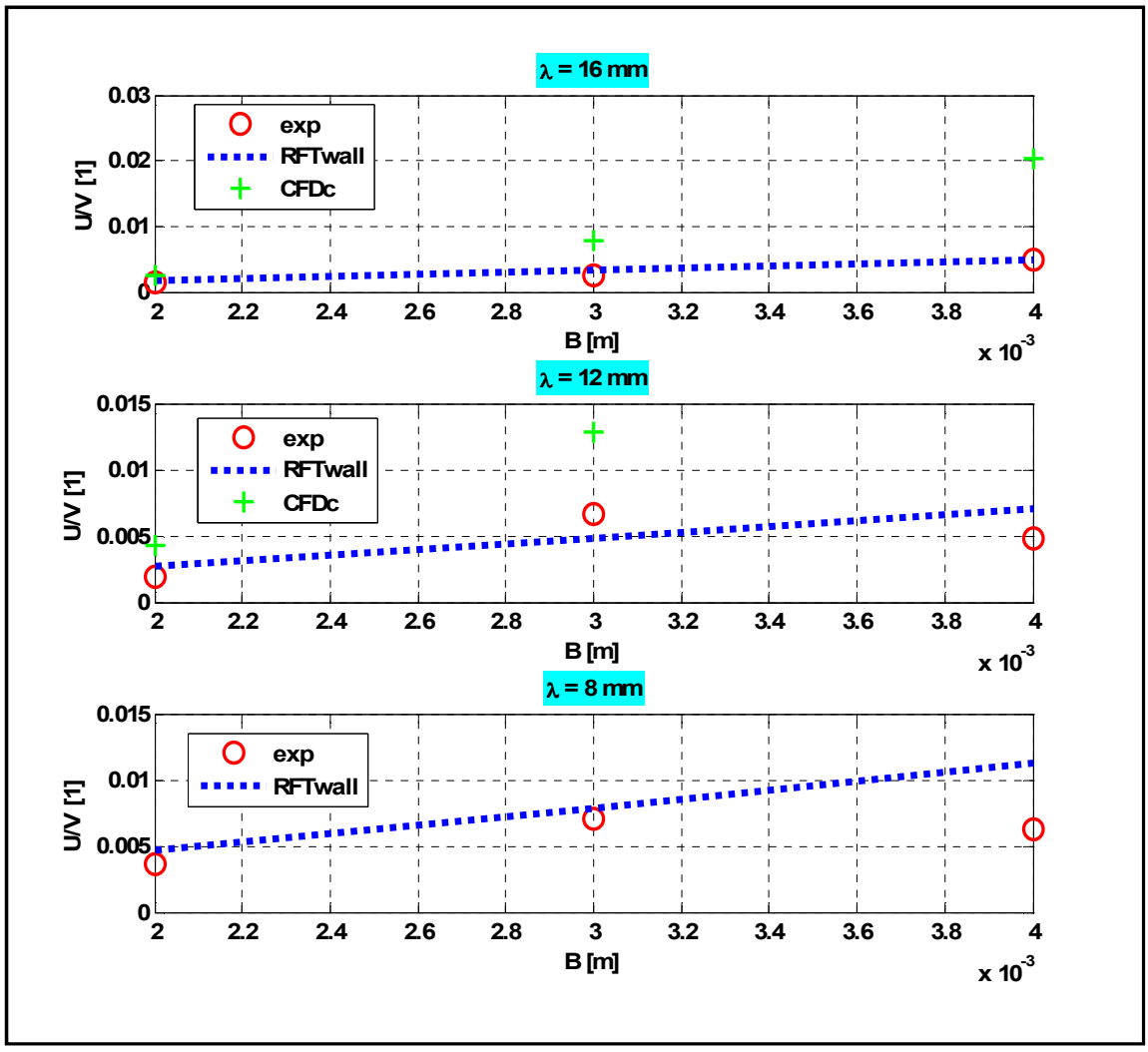

Figure 5.17: *U/V* vs. Amplitudes for *Channel21*

In Figure 5.17, measurements, the results of RFTwall model and CFDc (*center* simulations) are plotted with respect amplitude, *B*. As seen from figure, with increasing amplitude *B* leads to increase in thrust force; thus, the ratio of propulsive speeds to linear wave propagation speeds increase and this trend can be observed for all amplitudes. RFTwall model have good

agreement with experimental results. Similar to U/V vs. amplitude, CFDc models overestimates the experimental observations.

5.2. REASONS FOR SHORTCOMINGS OF AGREEMENT BETWEEN RESULTS

- **Wobbling Effect**

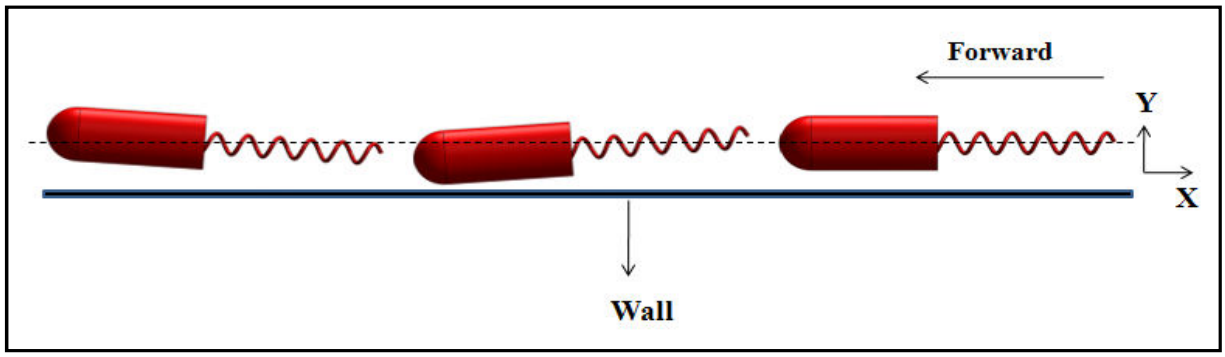

Figure 5.18: Wobbling movement of prototypes

Stability is an important criterion for prototype to have design which is close to real bacteria movement. The aim is make the position of the center of gravity and buoyancy get closer to each other since, application positions of these forces can result in either a restoring (stable condition, rotate back to original position) or overturning (unstable condition, move to a new equilibrium position) movement. Although some materials like putty is used to make weight and buoyancy forces collinear, this putting new materials into capsule does not always work effectively, thus this restoring and overturning movements can be observed as seen from the Figure 5.18. As a result of varying distance to the wall boundary, the interaction between the robots and boundary also varies along the prototypes. This effect cannot be fed into analytical and CFD models. Therefore, one of reasons for the shortcoming of agreement with results is this wobbling movement in experiments.

- **Conical Filament Trajectory**

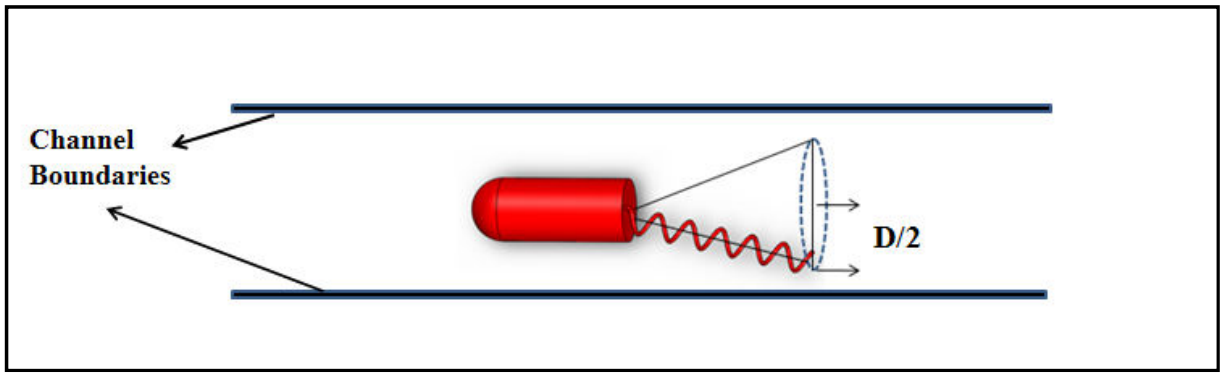

Figure 5.19: Conical trajectory of prototypes

Due to off axis connection of helical tail and revolute joint, the point on the flagellum may have position off-axially, too. This shape deficiency may make the tail follow a conical trajectory whose tip rotates around a larger circle as seen from the Figure 5.19 [48]. As a result of this trajectory, this helical tail's tip may come into contact with narrow cylindrical channels' boundaries thus, it can create traction. Also, because of this trajectory, tips' have higher velocity relative to tail proximal points and this additional velocity cannot be caught by CFD and analytical model. Due to these reasons, this conical trajectory can also be a reason for shortcoming of agreement.

- **Other Reasons**

One of the reasons for shortcomings of agreement is that the increasing effective length and weight for increasing amplitudes and wave numbers such as robots D_6 and D_6* has the largest effective length with largest amplitude, thus it can behave differently from the other ones due to this reason. For this robot, the propulsion force from the tail is not always balanced by the drag, as the vertical component of the force balances the effect of gravity on the robot, and only the horizontal component propels the robot.

Furthermore, shape deficiency of tails is the other reason for shortcoming of agreements. For instance, the robots with amplitude 2 mm have off axis connection of tail and revolute joints. In addition to that, like B_4 and C_3 robots waves are not equally fabricated. Thus, these robots can make the different behavior than the other ones.

Lastly, Resistive Force Theory is not taken into account of body and helical tail interaction. But, may be this is not very effective for bacteria which have micro or nanometer sizes but for this macro experiments, this interaction may have important effect on the results,

thus, Slender Body Theory can work better than Resistive Force Theory for these experimental measurements [49].

CHAPTER 6

CONCLUSION

This thesis presents both the macro design of helical swimmer and comparison of results between analytical and CFD models with experimental ones.

In the first part of the thesis, the helical swimmer is designed and built to measure the forward and angular velocities of body. Six design criteria are extremely important for analyzing the helical flagellar system appropriately which are neutral buoyancy, stability, propulsive speed, power requirement, size and simplicity. To make swimmer remained at rest in fluid, the ratio of weight to volume should be equal to fluid's specific weight. In addition to that, stable position of body can be achieved by coinciding the center of mass and buoyancy of it. Also, to obtain a desired propulsive speed, both the determination of swimmer dimensions and power source become important. Furthermore, for the repeatability of the experiments, manufacturing and assembly must be simple.

The onboard-powered swimming robot has two components (links): body and tail. The body of the robot is made from glass tube having 15.8 mm in diameter, 40 mm in length and a hemi-spherical cap. The body contains a small DC motor, a small polymer Li-Ion battery and a switch. The DC motor is a typical pager motor, which has a diameter of 6 mm and length of 10.4 mm. The size of the Li-ion polymer battery is 17.3x13.5x3.7 mm^3, and operates at 3.7 V with an energy storage capacity of 65 mAh, which is typically enough for a 4-minute continuous operation of the robot. A six legged switch of dimensions 7x3x3 mm^3 is used to connect the battery and the motor to control the power consumption.

The helical tail of the robot is made of steel wires with the diameter of 1 mm and apparent length of 48 mm. The connection between motor and tail is made with a plastic sleeve coupling material, which is constructed by drilling from opposite sides with respect to diameters of the motor shaft and the helical tail. The plastic sleeve coupling is secured to the tail by applying a heat process to ensure a stable rotation of the tail.

Components in the glass capsule that makes of the body of the robot are assembled with a consideration of design criteria and a soft putty material is used for hand calibration as

needed. The glass tube is sealed with a plastic cover to protect the components inside from direct contact with silicon oil. The plastic cap is drilled to fit the DC motor, and to provide a stable rotation of helical tail.

The swimming robot is placed inside a 30cm-long cylindrical channel with diameters of 36 mm and 24 mm named as *Channel 1* and *Channel 2*, respectively. The channels are kept open-ended and placed inside a pool of silicone oil with dynamic viscosity of 5.6×10^{-3} Pa-s.

For each case, experiments are repeated for at least three times, and average linear, U, and angular, Ω, velocities, frequency, f, of the tail are calculated from the images in 2-minute videos for each robot.

In the second part of the thesis, an analytical model is developed which is based on Resistive Force Theory (RFT). This theory suggests that, in Stokes regime, there is a linear relation between hydrodynamic forces and local velocity with a resistive force coefficient. This mathematical model is obtained by assuming swimmer is submerged in an environment with no upstream velocity and wall effects are not taken into account. The model is obtained for a 6 degree-of-freedom robot, but a 2 degree-of-freedom model for linear velocity, U, of the robot and the angular rotation rate, Ω, of the body are considered. In experiments, linear velocity of the body and the tail are measured. The rotation of the tail is fed into the model as input, and model's output, linear velocity of the robot and the angular velocity of the body are compared with measurements. Tuning coefficients for the linear and the rotational drag of the body are used to include additional friction between the body and the channel walls. Note that the tuning of the rotational drag coefficient of the body modified only the angular velocity of the body in calculations; linear velocity of the robot remained unaffected by the tuning of the body's rotational drag and the same is true for linear drag coefficient and rotational velocity of the body.

In the last part of the thesis, the swimming robot with a rigid helical tail and bullet shaped body is analyzed by COMSOL with three simulation sets to verify the experimental results. First set is representing the *center* motion of robots in *Channel 1* and the second one is representing same kind of motion in *Channel 2*. The last set is representing the *off-center* motion of robots in *Channel 2*. The swimmer is assumed to be neutrally buoyant and has the same density with the water in calculations. The motion is modeled by considering 2 degree-of-freedom robot with COMSOL. Time dependent position and orientation of the swimmer are calculated with ordinary differential equations (ODE) in the model. Total force and torque on the swimmer are calculated by integrating fluid forces on the swimmer's surfaces. These simulations are solved with Parallel-Direct-Sparse-Solver (PARDISO) by Intel Xeon

processor workstation with 96 GB RAM and they are running on CentOS Linux operation system.

Measured body's rotation rates and forward velocities from *Channel 1* and *Channel 2* experiments are compared with calculations from the RFT model. In addition to that the average linear velocities of robots are normalized by the wave propagation speed on the tail's curvilinear coordinates and compared with the normalized speed from experiments. Also, measured ratios of head rotation rate to motor rotation rate from experiments are compared with the analytical model results. Furthermore, measured normalized average velocities from experiments are compared with calculations from both the RFT model and COMSOL model with respect to helical tails' wavelengths and amplitudes.

Shortcomings of the agreement between the results of the model and experiments could be due to experimental procedure, especially in balancing of the robot for all tails. Even if the balance of the body is achieved reasonably well in the silicone oil, tails, which are made of the metal wire, tend to introduce a bias in the motion of the robot. Thus the propulsion force from the tail is not always balanced by the drag along the axis of the channel, as the vertical component of the force balances the effect of gravity on the robot, and only the horizontal component propels the robot.

Future works contain dealing with these design shortcomings to get better experimental results and analyzing the flow characterization with PIV (particle image velocimetry).

APPENDIX A

MATRIX CALCULATIONS

$$R_{BNT}^{SQR} = [\boldsymbol{b} \quad \boldsymbol{n} \quad \boldsymbol{t}] = \begin{bmatrix} b_1 & n_1 & t_1 \\ b_2 & n_2 & t_2 \\ b_3 & n_3 & t_3 \end{bmatrix}$$

$$\boldsymbol{C}_{nt} = \begin{bmatrix} -\boldsymbol{C}_n & 0 & 0 \\ 0 & -C_n & 0 \\ 0 & 0 & -C_t \end{bmatrix}$$

$$C_{RCR} = \begin{bmatrix} -C_n b_1^2 - C_n n_1^2 - C_n t_1^2 & -C_n b_1 b_2 - C_n n_1 n_2 - C_n t_1 t_2 & -C_n b_1 b_3 - C_n n_1 n_3 - C_t t_1 t_3 \\ -C_n b_1 b_2 - C_n n_1 n_2 - C_n t_1 t_2 & -C_n b_2^2 - C_n n_2^2 - C_n t_2^2 & -C_n b_2 b_3 - C_n n_2 n_3 - C_t t_2 t_3 \\ -C_n b_1 b_3 - C_n n_1 n_3 - C_t t_1 t_3 & -C_n b_2 b_3 - C_n n_2 n_3 - C_t t_2 t_3 & -C_n b_3^2 - C_n n_3^2 - C_n t_3^2 \end{bmatrix}$$

APPENDIX B

ROBOTS USED IN EXPERIMENTS

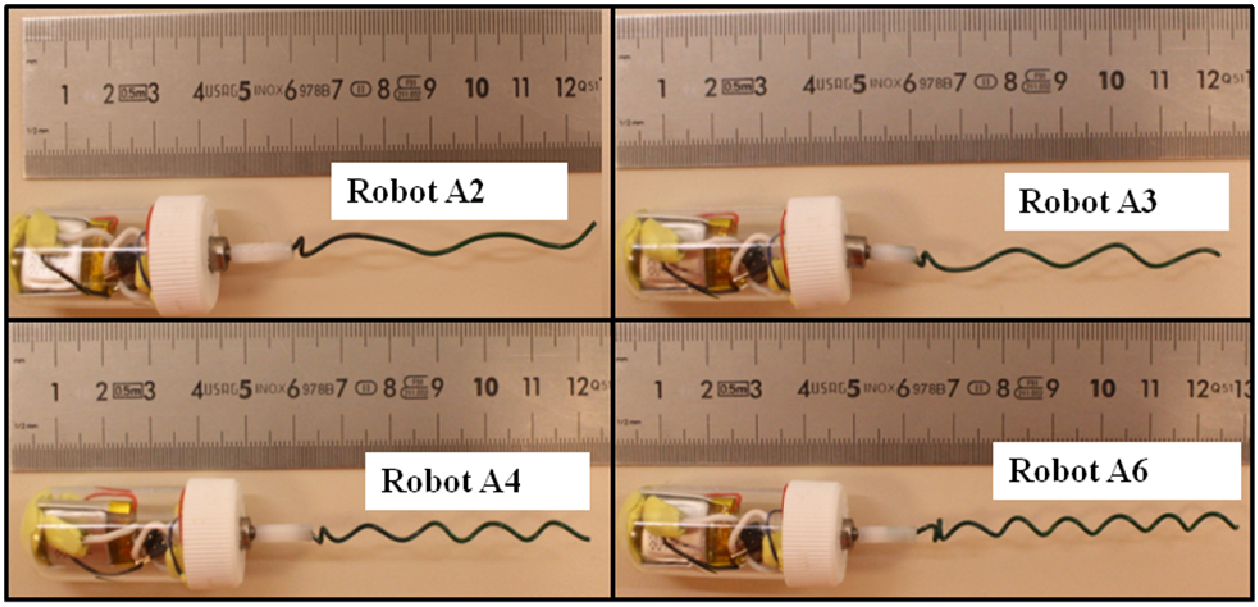

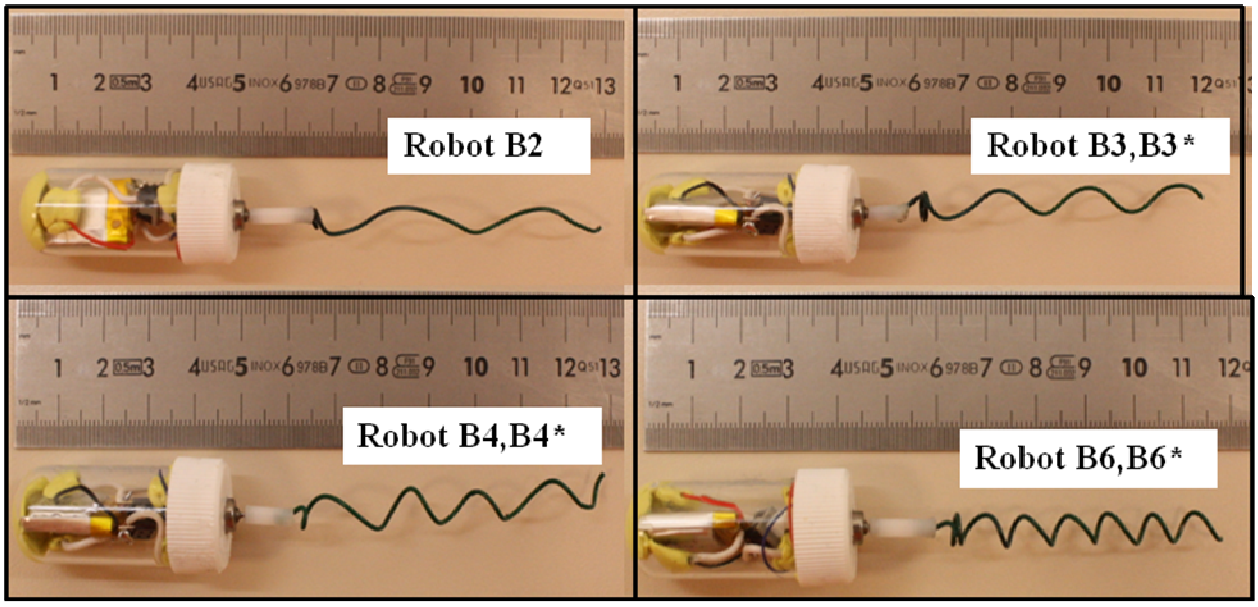
Robot B2
Robot B3,B3*
Robot B4,B4*
Robot B6,B6*

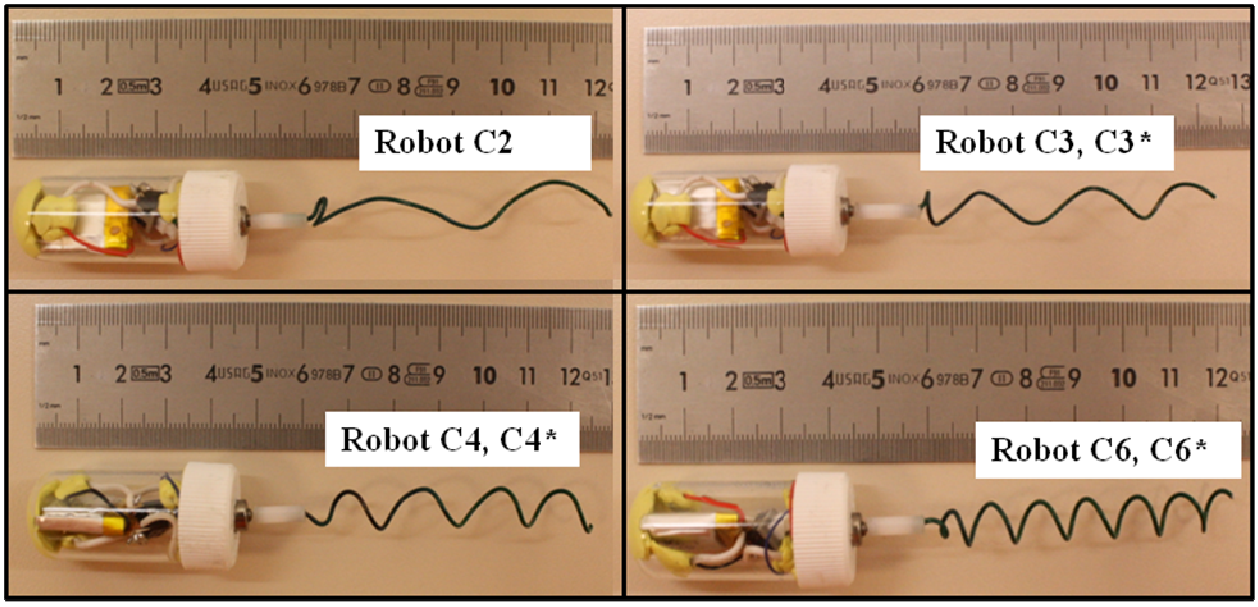
Robot C2
Robot C3, C3*
Robot C4, C4*
Robot C6, C6*

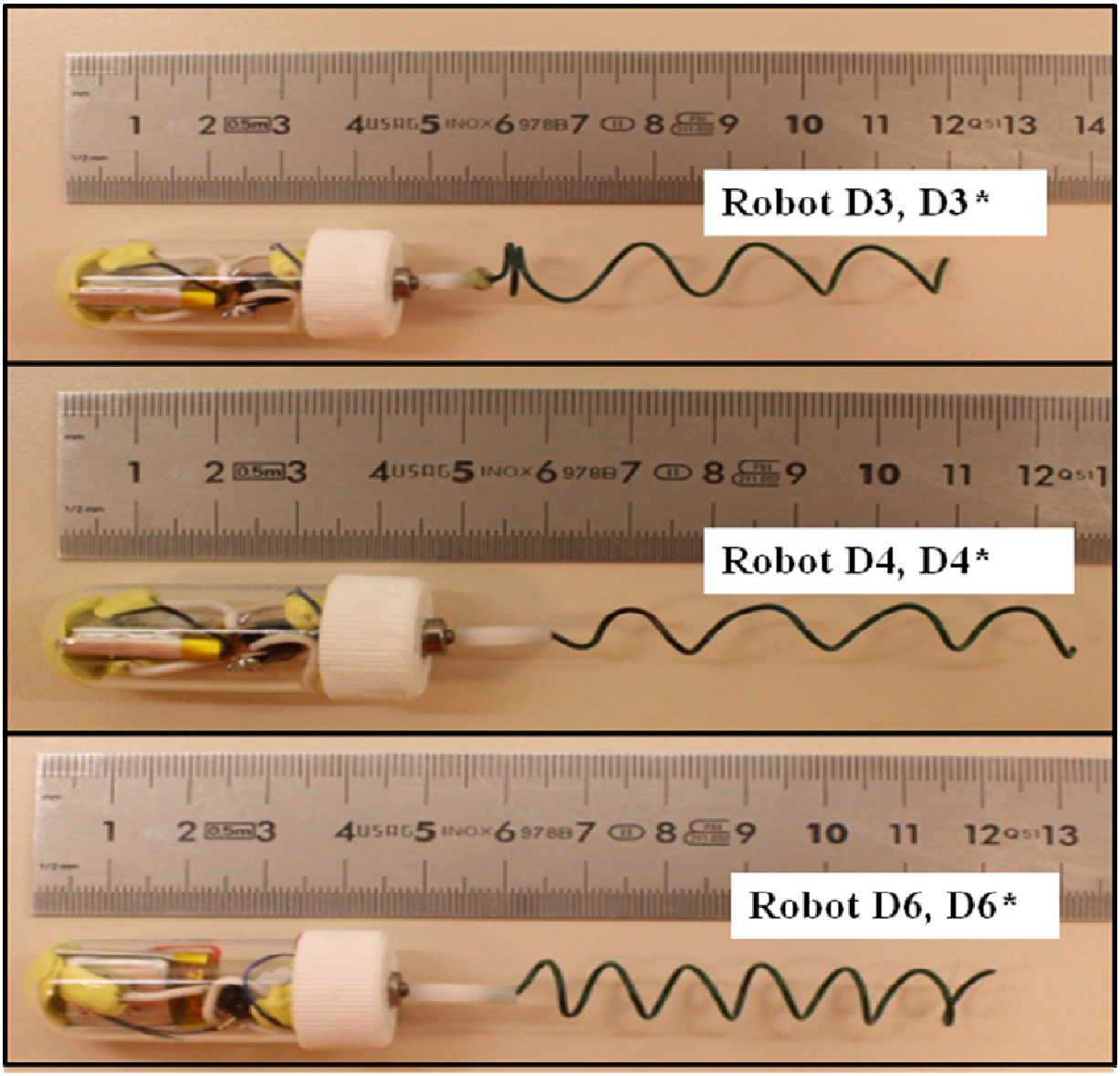
Robot D3, D3*
Robot D4, D4*
Robot D6, D6*

APPENDIX C

MESH STATISTICS

Table: *Channel 1 center* simulations mesh statistics

ROBOTS	**# of Degrees of Freedom**	**# of Tetrahedral Elements**
A_1	134090	24379
A_2	134090	24379
A_3	170459	31941
A_4	242630	46441
A_6	341379	64914
B_1	136544	24917
B_2	159946	29869
B_3	169147	31599
B_4	203130	38266
C_1	134090	24379
C_2	159946	29869
C_3	178418	33066
D_1	154519	28101
D_2	168331	30966
D_3	178418	33066

Table: *Channel 1 off-center* simulations mesh statistics

ROBOTS	**# of Degrees of Freedom**	**# of Tetrahedral Elements**
A_2	165239	30205
A_3	198684	37254
A_4	240788	45752
A_6	584862	114777
B_2	165239	30205
B_3	198684	37254
B_4	239946	45623
B_6	584862	114777
C_2	165239	30205
C_3	198684	37254
C_4	239946	45623

Table: *Channel 2 center* simulations mesh statistics

ROBOTS	**# of Degrees of Freedom**	**# of Tetrahedral Elements**
B_3^*	202763	36184
B_4^*	239823	43949
C_3^*	200992	43949
C_4^*	239823	43949
D_3^*	200992	35732

APPENDIX D

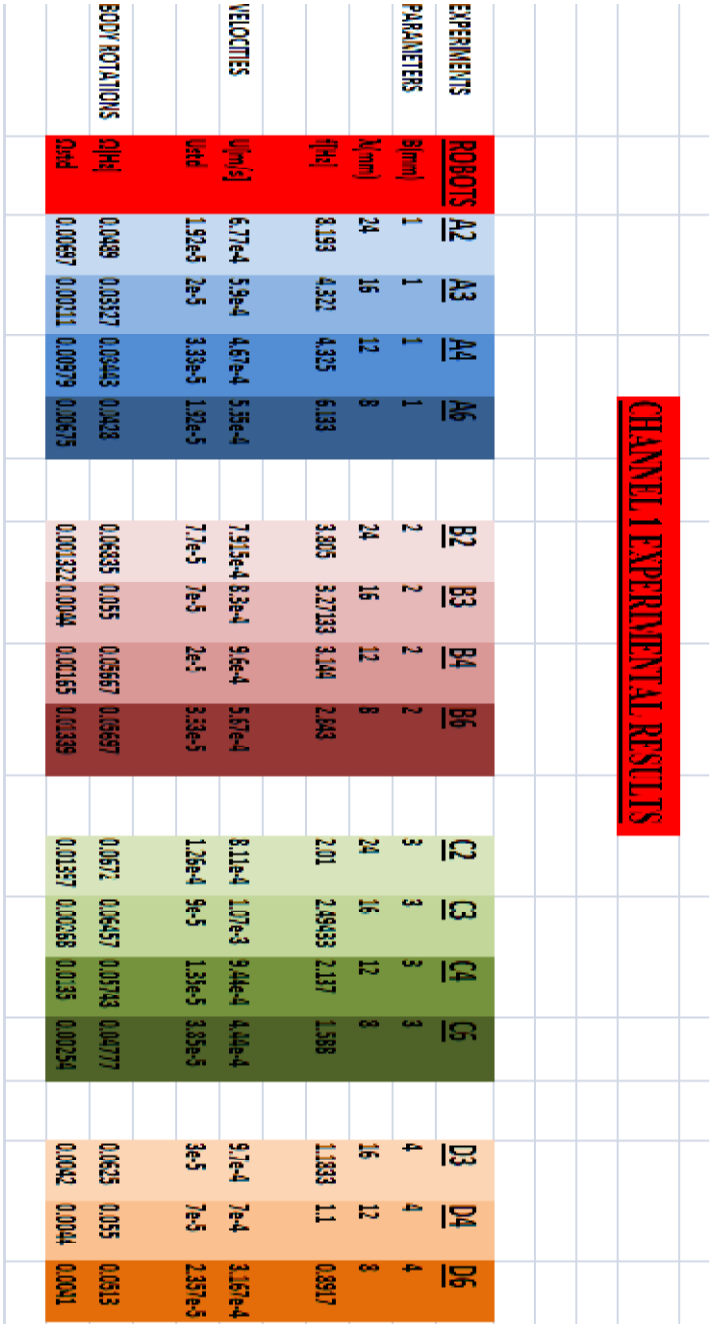

CHANNEL 1 EXPERIMENTAL RESULTS

EXPERIMENTS	A2	A3	A4	A6	B2	B3	B4	B6	C2	C3	C4	C6	D3	D4	D6
PARAMETERS	1	1	1	1	2	2	2	2	3	3	3	3	4	4	4
b[mm]	24	16	12	8	24	16	12	8	24	16	12	8	16	12	8
λ[mm]	8.193	4.921	4.925	6.133	3.805	3.27133	3.144	2.643	2.01	2.49433	2.137	1.588	1.1933	1.1	0.8917
f[Hz]	6.77e-4	5.9e-4	4.67e-4	5.35e-4	7.915e-4	6.3e-4	9.6e-4	5.67e-4	8.11e-4	1.07e-3	9.44e-4	4.44e-4	9.7e-4	7e-4	3.167e-4
VELOCITIES U[m/s]	1.92e-5	2e-5	3.33e-5	1.92e-5	7.7e-5	7e-5	2e-5	3.33e-5	1.26e-4	9e-5	1.35e-5	3.05e-5	3e-5	7e-5	2.357e-5
U.t.t.d	0.0697	0.00111	0.00979	0.10675	0.001322	0.0044	0.00165	0.01339	0.01357	0.00268	0.0135	0.00254	0.0042	0.0044	0.0041
BODY ROTATIONS Q[Hz]	0.0489	0.03527	0.03443	0.0428	0.06835	0.055	0.05667	0.05697	0.0672	0.06457	0.05743	0.04777	0.0635	0.055	0.0513
Q.t.t.d	0.0697	0.00111	0.00979	0.10675	0.001322	0.0044	0.00165	0.01339	0.01357	0.00268	0.0135	0.00254	0.0042	0.0044	0.0041

CHANNEL 1 CENTER COMSOL RESULTS

COMSOL

ROBOTS	A1	A2	A3	A4	A6	B1	B2	B3	B4	B6	C1	C2	C3	C4	D1	D2	D3
B	0.1	0.1	0.1	0.1	0.1	0.2	0.2	0.2	0.2	0.2	0.3	0.3	0.3	0.3	0.4	0.4	0.4
λ	4.8	2.4	1.6	1.2	0.8	4.8	2.4	1.6	1.2	0.8	4.8	2.4	1.6	1.2	4.8	2.4	1.6
f	6.9	8.193	4.322	4.325	6.133	3.9	3.805	3.27133	3.144	2.843	3.1	2.01	2.49433	2.137	2	1.6	1.1833
Umax	0.0026	0.0038	0.0052	0.006	0.0068	0.0103	0.0147	0.0179	0.0189		0.0227	0.031	0.0354		0.0404	0.053	0.0575
Umin	0.0024	0.0035	0.0048	0.0055	0.0062	0.0096	0.0139	0.017	0.018		0.022	0.03	0.0341		0.0397	0.0522	0.0566
Uavg	0.0025	0.0037	0.005	0.0057	0.0065	0.01	0.0143	0.0175	0.0184		0.0223	0.0305	0.0348		0.04	0.0526	0.057
Ωmax	0.1069	0.1129	0.0865	0.0899	0.099	0.1914	0.17	0.1899	0.2076		0.3295	0.3193	0.3674		0.482	0.5386	0.638
Ωmin	0.1016	0.1047	0.0844	0.0876	0.0953	0.1831	0.1653	0.1858	0.2031		0.3167	0.3118	0.3615		0.4748	0.5321	0.633
Ωavg	0.1042	0.1088	0.0854	0.0887	0.0972	0.1873	0.1677	0.1878	0.2053		0.3231	0.3156	0.3645		0.4784	0.5354	0.6355
Qmax	0.0024	0.0038	0.0049	0.0056	0.0064	0.0094	0.0135	0.0164	0.0177		0.0189	0.0262	0.0295		0.0283	0.0378	0.042
Qmin	0.0011	0.0017	0.0031	0.0036	0.0037	0.0063	0.0093	0.0122	0.0137		0.0139	0.0205	0.0244		0.0245	0.0339	0.0392
Qavg	0.0018	0.0028	0.004	0.0046	0.005	0.0078	0.0114	0.0143	0.0157		0.0164	0.0233	0.0269		0.0264	0.0358	0.0406

CHANNEL 1 OFF-CENTER COMSOL RESULTS

	ROBOTS	A2*	A3*	A4*	A6*	B2*	B3*	B4*	B6*	C2*	C3*	C4*
OFF CENTER COMSOL	Umax	0.0093	0.01	0.0108	0.0115	0.0309	0.0325	0.0326	0.0286	0.0622	0.0618	0.0579
	Umin	0.0043	0.0072	0.009	0.0104	0.0208	0.027	0.0288	0.026	0.0477	0.0537	0.0519
	Uavg	0.0068	0.0086	0.0099	0.0109	0.0258	0.0298	0.0307	0.0273	0.0549	0.0577	0.0549
	Ωmax	0.0058	0.0052	0.0051	0.0053	0.0149	0.0144	0.0149	0.0167	0.029	0.0295	0.0318
	Ωmin	0.0014	0.0026	0.0035	0.0046	0.0056	0.0089	0.0113	0.0148	0.0143	0.0205	0.0255
	Ωavg	0.0036	0.0039	0.0043	0.005	0.0103	0.0116	0.0131	0.0158	0.0216	0.025	0.0286
	Qmax	0.0051	0.0052	0.0051	0.005	0.0144	0.0146	0.0139	0.0119	0.0241	0.0236	0.0214
	Qmin	1.8234e-4	0.002	0.0031	0.0027	0.0043	0.0086	0.0103	0.0093	0.0102	0.0158	0.0167
	Qavg	0.0027	0.0036	0.0041	0.0038	0.0094	0.0116	0.0121	0.0106	0.0172	0.0197	0.0191

CHANNEL 1 RFT AND RFTWALL RESULTS

RFT TUNED MODEL	ROBOTS	A2	A3	A4	A6	B2	B3	B4	B6	C2	C3	C4	C6	D3	D4	D6
	B(mm)	1	1	1	1	2	2	2	2	3	3	3	3	4	4	4
	λ(mm)	24	16	12	8	24	16	12	8	24	16	12	8	16	12	8
	f[Hz]	8.193	4.322	4.325	6.133	3.7023	3.27133	3.144	2.843	2.01	2.49433	2.137	1.588	1.1833	1.1	0.51667
	U(m/s)	6.3862e-4	5.0877e-4	6.48773e-4	0.001147	9.692e-4	0.001092	0.0011075	8.3808e-4	9.20138e-4	0.001192	8.8874e-4	3.99458e-4	6.22478e-4	4.3136e-4	1.7067e-4
	Ω[Hz]	0.0362	0.0218	0.0239	0.0379	0.0604	0.0563	0.0545	0.0474	0.066	0.0803	0.0659	0.0443	0.0575	0.0499	0.0358
	Cn	27.1269	31.6739	35.6550	42.0896	26.5938	30.0566	32.1648	32.9191	25.7267	27.6823	27.8132	25.1831	25.0468	23.8054	19.9439
	Ct	16.6047	20.0062	23.0941	28.3720	16.0187	18.4121	20.0304	21.5773	15.2627	16.7417	17.3836	17.2848	15.2724	15.3292	14.4632
RFT WALL CORRECTED MODEL	U[m/s]	6.9358e-4	5.0637e-4	6.0964e-4	0.001014	0.001058	0.0010968	0.001077	8.7614e-4	0.0010384	0.001296	0.00101425	5.951331e-4	7.85828e-4	6.2424e-4	3.74862e-4
	Ω[Hz]	0.0369	0.0188	0.018	0.0232	0.0626	0.0502	0.0441	0.0348	0.0715	0.0778	0.0605	0.0402	0.0629	0.0537	0.0401

CHANNEL 2 EXPERIMENTAL RESULTS

CHANNEL 2	ROBOTS	B3*	B4*	B6*	C3*	C4*	C6*	D3*	D4*	D6*
PARAMETERS	B(mm)	2	2	2	3	3	3	4	4	4
	λ(mm)	16	12	8	16	12	8	16	12	8
	f (Hz)	3.611	3.7833	3.272	2.8167	2.42	1.761	1.0389	1	0.9167
VELOCITIES	Umeasured (m/s)	6.22e-5	6.11e-5	5e-5	7.083e-5	1.027e-4	3.88e-5	4.44e-5	2.5e-5	1.389e-5
	Ustd	7.698e-6	4.81125e-6	1.443e-5	9.317e-6	6.5168e-6	9.622506e-6	1.9245e-5	1.44337e-5	9.6225e-6
BODY ROTATIONS	Ωmeasured [Hz]	0.04942	0.03861	0.0361	0.074167	0.06	0.06694	0.0467	0.0389	0.04194
	Ωstd	0.01456	4.2763e-3	4.81125e-3	1.1785e-3	0.0192	3.7577e-3	4.40958e-3	6.31e-3	6.02667e-3

CHANNEL 2 CENTER COMSOL RESULTS

COMSOL (nondimensional)	ROBO B3*		B4*	C3*	C4*	D3*
PARAMETERS	B(mm)	2	2	3	3	4
	λ(mm)	16	12	16	12	16
	f[Hz]	3.611	3.7833	2.8167	2.42	1.0389
VELOCITIES	Umax	0.0036	0.0038	0.0085	0.0086	0.0176
	Umin	0.003	0.0032	0.0078	0.0081	0.0174
	Uavg	0.0033	0.0035	0.0082	0.0083	0.0175
BODY ROTATIONS	Ωmax	0.1996	0.2170	0.3918	0.4352	0.6906
	Ωmin	0.1986	0.2158	0.39	0.4337	0.6887
	Ωavg	0.1991	0.2164	0.3909	0.4345	0.6896
FLOW RATES	Qmax	0.0147	0.0159	0.0274	0.0285	0.0379
	Qmin	0.0132	0.0143	0.0256	0.027	0.0373
	Qavg	0.014	0.0151	0.0265	0.0278	0.0376

CHANNEL 2 RFT AND RFTWALL RESULTS

RFT TUNED MODEL	ROBOTS	B3*	B4*	B6*	C3*	C4*	C6*	D3*	D4*	D6*
PARAMETERS	B(mm)	2	2	2	3	3	3	4	4	4
	λ(mm)	16	12	8	16	12	8	16	12	8
	f (Hz)	3.611	3.7833	3.272	2.8167	2.42	1.761	1.0389	1	0.9167
	U[m/s]	1.004e-4	1.11e-4	8.037e-5	1.122e-4	8.383e-5	3.691e-5	4.554e-5	3.268e-5	1.462e-5
	Ω[Hz]	0.0517	0.0546	0.0455	0.0756	0.0621	0.047	0.0421	0.0378	0.0307
RFT WALL CORRECTED MODEL	U[m/s]	7.772e-5	8.33e-5	6.545e-5	9.46e-5	7.47e-5	4.321e-5	4.42e-5	3.655e-5	2.495e-5
	Ω[Hz]	0.0469	0.0448	0.0339	0.0735	0.058	0.0378	0.0457	0.0406	0.0342

REFERENCES

1. Dario P., Carrozza MC., Benvenuto A., Menciassi A. 2000. Micro-systems in biomedical applications. *J. Micromech. Microeng.* 10(2):235-44
2. B. Nelson, I. Kaliakatsos, J. Abbott, "Microrobots for Minimally Invasive Medicine,"*The Annual Review of Biomedical Engineering*, pp. 55-85, 2010
3. Carrozza MC., Dario P., Jay LPS. 2003. Micromechatronics in surgery. *Trans. Inst. Meas. Control* 25(4):309-27
4. G.M. Patel, G. C. Patel, R. B. Patel, J. K. Patel, M. Patel, "Nanorobot: A versatile tool in nanomedicine", *Journal of Drug Targeting*, vol. 14, pp. 63-67, 2006.
5. Taylor, Sir, G.I., "Analysis of the Swimming of Microscopic Organisms", *Proc. R. Soc. Lond.*, 209(A), pp. 447-461, 1951.
6. Gray, J., Hancock, G.J., "The Propulsion of Sea Urchin Spermatozoa", *J. Exp. Biol*., Vol.32, pp. 802-814, 1955.
7. Keller, J.B., Rubinow, S. I., "Swimming of Flagellated Microorganisms", *Biophysical Journal*, Vol. 16, pp.151-170, 1976.
8. Lighthill, J. 1976. Flagellar Hydrodynamics . *SIAM Rev*. 18: 161-230.
9. R. E. Johnson, C. J. Brokaw, "A Comparison between Resistive-Force Theory and Slender Body Theory", *Biophys. J. Biophysical Society*, pp. 113-127, 1979.
10. A.T. Chwang, T.Y. Wu, "A Note on the Helical Movement of Micro-Organisms", *Proc. R. Soc. Lond. B*, pp. 327-346, 1971.
11. J. J. L. Higdon, "The hydrodynamics of flagellar propulsion: helical waves", *J. Fluid Mech.*, vol. 94, pp. 331-351, 1979.
12. A.J. Reynolds, "The swimming of minute organisms", *J. Fluid Mech*. , vol. 23, part 2, pp. 241-260, 1965.
13. J.R. Blake, "A note on the image system for a stokeslet in a no-slip boundary condition", *Proc. Camb. Phil. Soc.,* vol. 70, pp. 303-309, 1971.
14. J.R. Blake, A.T. Chwang, "Fundamental singularities of viscous flow. Part I. The image systems in the vicinity of a stationary no-slip boundary. *J. Eng. Math*. 8:23-29
15. D.F. Katz, J.R. Blake, L. Paveri-Fontana, "On the movement of slender bodies near plane boundaries at low Reynolds number", *J. Fluid Mech*., vol. 72, part 3, pp. 529-540, 1975.
16. M. Ramia, D.L. Tullock, N.Phan-Thien, "The Role of Hydrodynamic Interaction in the Locomotion of Microorganisms", *Biophysical Journal*, Vol. 65, pp.755-778, 1993.
17. E. Lauga, W. R. DiLuzio, G. M. Whitesides, H. A. Stone, "Swimming in Circles: Motion of Bacteria near Solid Boundaries", *Biophysical Journal*, vol. 90, pp. 400-412, 2006.
18. T. Goto, K. Nakata, K. Baba, M. Nishimura, Y. Magariyama, "A Fluid-Dynamic Interpretation of the Asymmetric Motion of Singly Flagellated Bacteria Swimming Close to a Boundary", *Biophysical Journal*, vol. 89, pp. 3771-3779, 2005.
19. T. Goto, S. Masuda, K. Terada, Y. Takano, "Comparison between Observation and Boundary Element Analysis of Bacterium Swimming Motion," *JSME International Journal*, Vol.44, pp.958-963, 2001.

20. T. Nakai, M. Kikuda, Y. Kuroda, T. Goto, “Speed, Trajectory and Increment in the Number of Cells of Singly Flagellated Bacteria Swimming Close to Boundaries”, *Journal of Biomechanical Science and Engineering*, Vol.4,No.1, 2009.
21. S. Chattopadhyay, X.L. Wu, “The Effect of Long-Range Hydrodynamic Interaction on the Swimming of a Single Bacterium”, *Biophysical Journal*, Vol.96, pp.2023-2028, 2009.
22. E. M. Purcell, “Life at low Reynolds number”, Am. J. Phys, 1977.
23. L. E. Becker, S. A. Koehler, H. A. Stone, “On self-propulsion of micro-machines at low Reynolds number: Purcell’s three link swimmer”, Journal of Fluid Mechanics, 490:15-35, 2003.
24. Brian Chan. Propulsion devices for locomotion at low reynolds number. Master’s thesis, Massachusetts Institute of Technology, 2004.
25. R. Dreyfus, J. Boundry, M. L. Roper, M. Fermigier, H. A. Stone, J. Bibette, “Microscopic Artificial Swimmer”, *Nature*, vol.437, 2005.
26. B. Behkam, M. Sitti, “Design Methodology for Biomimetic Propulsion of Miniature Swimming Robots”, *Journal of Dynamic Systems, Measurement, and Control*, vol.128, 2006.
27. S. Martel, J.B. Mathieu, O. Felfoul, A. Chanu, E. Aboussouan, S. Tamaz, P. Pouponneau, L. Yahia, G. Beaudoin, G. Soulez, M. Mankiewicz, "Automatic navigation of an untethered device in the artery of a living animal using a conventional clinical magnetic resonance imaging system", *Applied Physics Letter*, vol. 90, 2007.
28. L. Zhang, J.J. Abbott, L. Dong, B.E. Kratochvil, D. Bell, B.J. Nelson, “Artificial bacterial flagella: Fabrication and magnetic control”, *Applied Physics Letters*, vol.94, 2009.
29. K. Peyer, L. Zhang, B.E. Kratochvil, “Non-ideal Swimming of Artificial Bacterial Flagella Near a Surface”, *IEEE International Conference on Robotics and Automation*, 2010.
30. T.S. Yu, "Elastic Tail Propulsion at Low Reynolds Number", Master of Science in MIT ;Mechanical Engineering, 2007.
31. S. Zhang, Y. Or, R.M. Murray, “Experimental Demonstration of the Dynamics and Stability of a Low Reynolds Number Swimmer Near a Plane Wall”, *American Control Conference,* 2010.
32. B. Chen, S. Jiang, Y. Liu, P. Yang, S. Chen, “Research on the Kinematic Properties of a Sperm-Like Swimming Micro Robot”, *Journal of Bionic Engineering*, vol. 7, pp.123-129, 2010.
33. S. Martel, M. Mohammadi, O. Felfoul, Z. Lu, P. Pouponneau, "Flagellated Magnetotactic Bacteria as Controlled MRI-trackable Propulsion and Steering Systems for Medical Nanorobots Operating in the Human Microvasculature", The International Journal of Robotics Research, vol. 4, pp. 571-582, 2009.
34. G. Dogangil, O. Ergeneman, J.J. Abbott, S. Pane, H. Hall, S. Muntwyler, B. J. Nelson, "Toward Targeted Retinal Drug Delivery with Wireless Magnetic Microrobots", *IEEE/RSJ International Conference on Intelligent Robots and Systems*, pp. 22-26, 2008.
35. S. Devasia, E. Eleftheriou, S. O. R. Moheimani, "A Survey of Control Issues in Nanopositioning", *IEEE Transactions on Control Systems Technology*, Vol. 15, No. 5, 2007.

36. N. Siauve, R. Scorretti, N. Burais, L. Nicolas, A. Nicolas, "Electromagnetic fields and human body: a new challenge for electromagnetic field computation", *The International Journal for Computation and Mathematics in Electrical and Electronic Engineering*, Vol. 22, No. 3, pp. 457-469, 2003.
37. R. A. Bullen, T.C. Arnot, J.B. Lakeman, F. C. Walsh, "Biofuel cells and their development", *Biosensors and Bioelectronics*, 2006.
38. A. Heller, "Miniature biofuel cells", *Phys. Chem. Chem. Phys*. , vol. 6, pp.209-216, 2004.
39. Phan-Thien, N., T. Tran-Cong, M. Ramia, "A boundary element analysis of flagellar propulsion", *J. Fluid Mech*.,pp. 533-549, 1987.
40. B. U. Felderhof, "Swimming at low Reynolds number of a cylindrical body in circular tube", *Physics of Fluid*, vol. 22, 2010.
41. Thesis, Michael W. Wybenga, "Design of a Propulsion System for Swimming Under Low Reynolds Flow Conditions"
42. T.S. Yu, "Elastic Tail Propulsion at Low Reynolds Number", Master of Science in MIT; Mechanical Engineering, 2007.
43. H. C. Berg, "Random Walks in Biology", 1983.
44. A. F. Tabak, S. Yesilyurt, "Validated Reduced Order Models for Simulating Trajectories of Bio-Inspired Artificial Micro-Swimmers", *Conference on Microchannels and Minichannels*, 2010.
45. L. Braescu, T. F. George, "Arbitrary Lagrangian-Eulerian method for coupled Navier-Stokes and convection-diffusion equations with moving boundaries", *12tf WSEAS Int. Conf. on APPLIED MATHEMATICS,* 2007.
46. M. Koz, S. Yesilyurt, "Simulations of microflows induced by rotation of spirals in microchannels", *Microfluidics, BioMEMS, and Medical Microsystems VI*, Vol.6886, 2008.
47. M. Koz, S. Yesilyurt, "Simulation-Based Analysis of the Micropropulsion with Rotating Corkscrew Motion of Flagella", *ASME Fluids Engineering Division Summer Meeting*, 2009.
48. S. Trachtenberg, D. Fishelov, M. B. Artzi, "Bacterial Flagellar Microhydrodynamics: Laminar Flow over Complex Flagellar Filaments, Along Archimedean Screws and Cylinders, and Its Perturbations", *Biophysical Journal*, Vol. 85, pp. 1345-1357, 2003.
49. B. Behkam, M. Sitti, "Modeling and Testing of a Biomimetic Flagellar Propulsion Method for Microscale Biomedical Swimming Robots", *International Conference on Advanced Intelligent Mechatronics,* 2005.